INVESTIGATION OF THE TURBULENT AXISYMMETRIC JET MIXING LAYER

by

Muhammed S. S. Khwaja

A thesis submitted to the Faculty
of the Graduate School of State University
of New York at Buffalo in partial fulfillment
of the requirements for the degree of
Master of Science

February 1981

ACKNOWLEDGEMENTS

The author wishes to express his sincere appreciation for the knowledge, guidance, inspiration and stimulation received from his advisor, Professor William K. George, Jr., during the course of this investigation. The students and staff of the Turbulence Research Laboratory deserve a special mention for their effectiveness, as a cohesive group, in the interchange of knowledge and skills.

The author recognizes the high degree of significance of the unqualified support received from his family in all his educational endeavors.

The support received from the Department of Mechanical and Aerospace Engineering in the form of a Teaching Assistantship is gratefully acknowledged. The funding for the experimentation received from the National Science Foundation (Grant No. ENG76-17466) and the Air Force Office of Scientific Research (Contract No. F49620-78-C-0047) and the personal support received in the form of a Research Assistantship from the Research Foundation of the State University of New York, Air Force Office of Scientific Research (Contract No. F49620-78-C-0047) are gratefully acknowledged.

Special thanks are due to Mrs. Eileen Graber for expert secretarial help in the completion of this thesis.

TABLE OF CONTENTS

TABLE OF CONTENTS (cont.)

List of Figures

List of Figures (cont.)

List of Figures (cont.)

Nomenclature

B	Correlation coefficient
D	Jet exit diameter, m
e	Instantaneous voltage signal, volts
E	Linearizer output voltage, volts.
f	Frequency, H_z
F_{11}^1	One dimensional velocity spectrum (of u' velocity), m^3/sec^2
h	Dynamic ead of water in manometer, inches
$\underline{k}$	Wave number ector, m^{-1}
k_1	Wave number along x, m^{-1}
k_2	Wave number along y, m^{-1}
k_3	Wave number along z, m^{-1}
$\overline{K}$	Linearization constant, u/v or U/E, m/sec. volts
M	Momentum flux, $kg.m/sec^2$
ρ	Normalized correlation coefficient
R	Jet exit radius, m
Re	Reynolds number
r	Radial coordinate m(x,r,ϕ) coordinate system
S_e	Half line power spectral density of voltage signal, $volt^2/Hz$
S_u	Half line power spectral density of velocity signal, m^2/sec^2 Hz
T	Absolute temperature, degrees R
u' or u_1	Instantaneous velocity along x coordinate, m/sec.
$\overline{U}$	Mean velocity along x coordinates, m/sec.
U_e	Mean jet exit velocity, m/sec
U_c	Mean convection velocity, m/sec
$U_{\mathcal{L}}$	Mean jet centerline velocity, m/sec

Nomenclature(cont.)

u/v	Same as $\overline{K}$
u_{eff}	Effective cooling velocity for hot-wire sensor, m/sec
v' or u_2	Instantaneous velocity along y-coordinate, m/sec
V	Volts
w' or u_3	Instantaneous velocity along z-coordinate, m/sec
x	x coordinate in (x,y,z) system
y	y coordinate in (x,y,z) system
z	z coordinate in (x,y,z) system
α	Constant, approximately = 1.5
ε	Dissipation of turbulent energy, m^3/sec^2
ℓ	Velocity integral scale, m
ℓ_ω	Sensor length, mm
$\mathscr{L}$	Velocity integral scale, used interchangable with ℓ, m
λ	Wave length or length scale, m
θ	Momentum thickness, cm
ρ	Density of air, kg/m^3
τ	Time lag, sec
$\mathscr{T}$	Time integral scale, sec
ϕ	ϕ coordinate in (x,r,ϕ) system
overbar	denotes time averaging

ABSTRACT

This investigation is part of a continuing program of investigation of jet mixing layers. The primary interest is the large scale structure of turbulence in the initial mixing region of an axisymmetric, incompressible, non-reacting, single phase, isothermal air jet in a non-stratified, quiescent environment.

To establish the viability of the jet facility for extensive measurements later, basic mean flow and spectral dynamic measurements were carried out using analog and digital data processing techniques. These measurement have helped establish the credibility of the facility and the signal processing hardware.

As a first step towards the investigation of the large eddy structure in the mixing layer space-time cross-spectral and spacial cross-correlation characteristics were examined in the mixing layer. The cross-spectral measurements are continuing while some significant initial results of the cross-correlation measurements are reported here. There is evidence of the existence of over 5% of the turbulent energy (of longitudinal velocity vectors) in scales more than ten times as large as the local integral scales. Time-autocorrelation measurements also provide evidence for the existence of these large scales.

CHAPTER I

1. Introduction

1.1 Background

The first extensive investigations of the axisymmetric jet mixing laye are due to Davies, Fisher and Barrat (8) and Bradshaw, Ferris and Johnson (4). Bradshaw et al. proposed a conceptual model for the large scale structure after the manner of Townsend (1956) and Grant (1958). Their structure was described as ",..a series of mixing jets which instead of lying in the (x,y) plane as in the wake, more at an angle of about 45° to this plane". While useful in characterizing the large scale turbulent structure, this conceptual model does not appear to have been extended to a quantitative model.

More recently, Crow and Champagne (7) observed "puff-like" eddies in the mixing layer when they periodically forced the settling chamber of the jet. The puffs were not visible at high Reynolds numbers. Inviscid instablility theory appeared to correlate satisfactorily the maximum growth rates of the jet distrubances. Hussain (1974) performed similar experiments on a two-dimensional jet with substantially the same results although the growth rates and frequencies observed were different. These experimental approaches were motivated in part by the wave-guide turbulence model of Landahl, which modeled turbulence as dispersive waves in a shear layer.

Davies (1972) has suggested that the jet mixing layer is dominated by "roller eddies" which are vortex ring type structures. George and Lauchle (1973) inferred such structures from measurements of the intermittency profile. Nagib (20) and others have visually observed the interaction of such large structures; the phenomenon is similar to that of one vortex ring overtaking and blowing through another. Both dye and bubble rings can no

longer be distinguished at higher Reynolds numbers.

In 1967, Lumley proposed an objective technique for deducing the larg eddy structure of turbulent flows. The technique is based on an orthogona decomposition of the space-time correlation of the statistical quantity be observed. An outstanding advantage of Lumley's orthogonal decomposition i that it requires no subjective judgments on the part of the experimentalis as to the presence or absence of structure. In spite of this advantage, because of the large amount of data required it has, until recently, never been applied, in full, to an experimental problem.

Arndt and George (1974) in a review of Lumley's (1967) orthogonal decomposition showed that both wave-like and vortex-like interpretations of the eddy structure were consistent and resulted from the partial homogeneity of the flow field. The vortices were viewed as groups of dispersive waves. *The lifetime of the group is proportional to its spacial* bandwidth. As the Reynolds number is increased, the "eddy" spectrum broadens and the lifetime diminished. Visibility of the eddy was seen to depend on this lifetime; that is, the degree to which the spectral energy of the eddy was concentrated near a single wavenumber-frequency pair. Thus, the eddies become increasingly less visible as Reynolds number increases. This is consistent with observations. In particular, Hussain (1974) has remarked that the jet mixing layer appears to be puff-like or vortex-like at low Reynolds number and wave-like at high Reynolds number. Through the orthogonal decomposition the jet is seen to possess both characteristics at once. Similar conclusions were reached by Michalke and Fuchs (1975) from application of a simplified decomposition to the near field pressure.

Arndt and George (1974) also showed how the large eddy obtained from the decomposition could be used to directly compute the radiated noise spect

Currently at SUNY/Buffalo an extensive program is underway with NSF and AFOSR support to carry out such a decomposition of the turbulent velocity field in a high Reynolds number jet for which there is no visibly discernible structure. To date, the only evidence for coherent structures in jet mixing layers is visual and at low Reynolds numbers. This investigation is intended to confirm (or deny) their existence by modern statistical techniques which impose increased objectivity on the investigation.

1.2 Recent Investigations:

A host of investigators have in the recent years studied the near fiel and the large scale structure of axisymmetric jets. Hussain et al. (15) have studied the effects of initial conditions on the evolution and average characteristics of free shear layers, and indicated that discrepancies in d of different investigators may be attributed primarily to apparatus depende initial conditions.

Davies and Yule (1974) summarized the developments in understanding of the large scale structure in free shear layers. They stressed the importan of making simultaneous flow-visualization and quantitative investigations s that observed phenomenon could be related to measured velocity time histori Statistical measuring techniques have to-date only provided quantitative information on time-averaged properties, so that much of the detail of such structures is lost.

Pertinent to the present investigation, Bradshaw et al. (4) using their "mixing jets" model envisioned the existence of very large scales due to a shaking of the mean velocity gradient by the random cross-stream velocity component undulations of the shear layer.

Jones et al. (17) investigated space-time correlations in a two-stream mixing layer. They observed differences between axial broadband convection velocities and both mean turbulence and mean entrained fluid velocities. Scaled broadband convection velocities for the mixing layer and simple round jets were found to collapse to a common curve. Axial narrow band convection velocities showed strong frequency and transverse position dependence.

1.3 Scope of This Investigation:

The goals of the present investigation were two fold. Firstly to establishing a credible axisymmetric jet facility and data acquisition and processing hardware. This was to be accomplished by establishing scaling relationships for mean flow and spectral quantities. Secondly, to begin quantitative first and second order statistical measurements and to scale the results with spacial and temporal parameters.

The investigation is described in detail in the following chapters. Chapter 2 describes the jet facility used in this investigation while Chapter 3 details the instrumentation and procedures for calibrating them. The results of the investigation are presented in Chapters 4, 5 and 6, which present and discuss the mean flow properties of the jet, the spectral characteristics and the two point statistics, respectively. Chapter 7 summarizes the results and provides commentary on their usefulness.

CHAPTER 2

2. The Jet Facility

The facility for generating a nonreacting, single-phase, isothermal, incompressible, axisymmetric air jet is shown schematically in Figure 2.1. The facility can be used to generate exit velocities ranging from a few cm/sec to about 100 m/s. The range of exit velocities used in this experiment was between 13 m/s and 40 m/s. Based on the exit diameter of 20.57 cm this corresponds to Reynolds numbers of 2.2×10^5 to 5.4×10^5.

Quantitative measurements of the jet exit profile are discussed in Chapter 4. The exit plane turbulence intensity was 0.33%, the profile was flat to within 0.1% and the boundary layer was approximated to be 4 mm thick

Air intake is through a 102 x 87 x 87 cm filter box that can filter particles larger than about 5 μm in size. The air velocity through the filter elements is less than 20 cm/sec at full flow, thus resulting in low penetration of dust and good filtering efficiency.

The filtered air passes through a flow control mechanism which is primarily a 80 cm diameter orifice with variable pitch radial vanes. A manually controlled lever regulates the intake area from 5% to 100% fully open. Downstream of the control is the power source of the jet; the blower.

The blower is a 80 cm diameter radial flow "limit load fan" with 40 vanes. For the experiments under discussion the blower was run at a fixed speed of 875 r.p.m., powered by a 30 h.p., 3 phase induction motor running at 1750 r.p.m. A 1:2 ratio in speeds is accomplished by pulleys driven by multiple belts. The speed ratio achieved by the pulleys is operator selectable. The flow exits from the blower housing through a 43 x 51 cm opening and into a section which consists of 2.5 cm square channels and is 15 cm in length. The entire blower assembly is rigidly mounted on a 15 m^3 concret

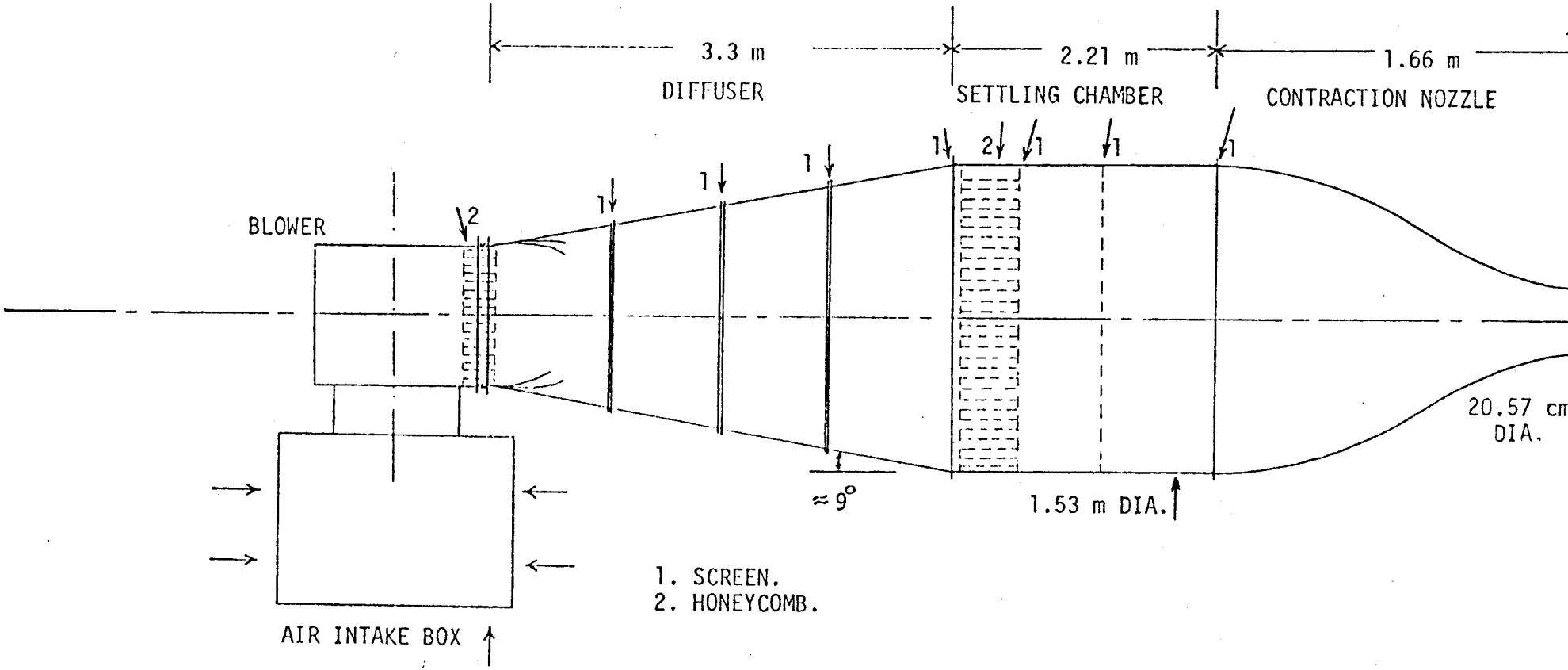

FIG. 2.1 JET FACILITY SCHEMATIC.

foundation to damp vibrations.

The diffuser is connected to the blower housing with flexible mounts designed to prevent transmission of vibrations from the blower to the rest of the flow facility downstream. The diffuser is 3.3 m long with a final diameter of 1.53 m, which corresponds to a diffuser total angle of about 18 degrees. The diffuser is in four sections of equal axial length, with the first upstream section providing a transition from a rectangular to a circular flow cross section. The design of the diffuser is based on NACA Report No. 949 (on screen diffusers), and it was meant to safely avoid flow separation for the entire range of operation of the jet facility. This objective is achieved by placing screens after every section of the diffuser The first two upstream sections have 20 mesh, 25% solidity screens and the downstream two have 30 mesh, 35% solidity screens, all of them woven with stainless steel wire.

Downstream of the diffuser is a 2.21 m long, 1.53 m in diameter settlin chamber. About 20 cm from the entrance to the settling chamber begins a 25 cm long honeycomb section. The honeycomb consists of over 100,000 cockta straws, each with an approximately circular flow passage and an average inside diameter of 4.5 mm, packed together and aligned with the axis of the settling chamber. Holding the straws against the drag from a maximum settli chamber flow velocity of 70 cm/sec is a 10 mesh screen. There is also a 10 mesh screen in the middle of the settling chamber and another at the entr ance to the contraction nozzle.

The contraction nozzle is 166.4 cm long, has an area contraction ratio 56.25:1 (diameter ratio of 7.5:1) with an exit diameter of 20.57 cm. The nozzle is made of spun aluminum alloy and is a surface of revolution of two matched polynominals. See Figure 2.2. The nozzle was not constructed

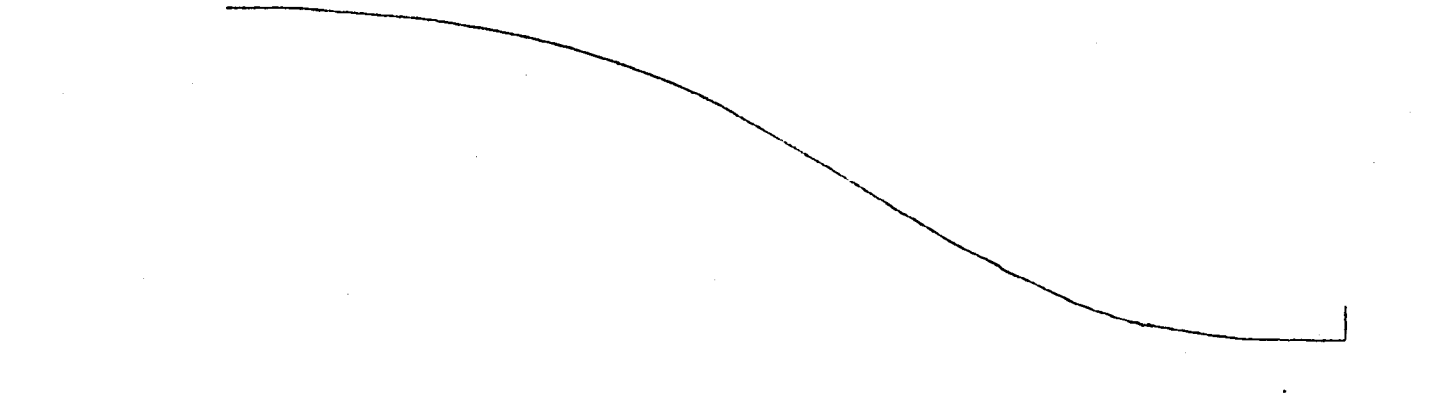

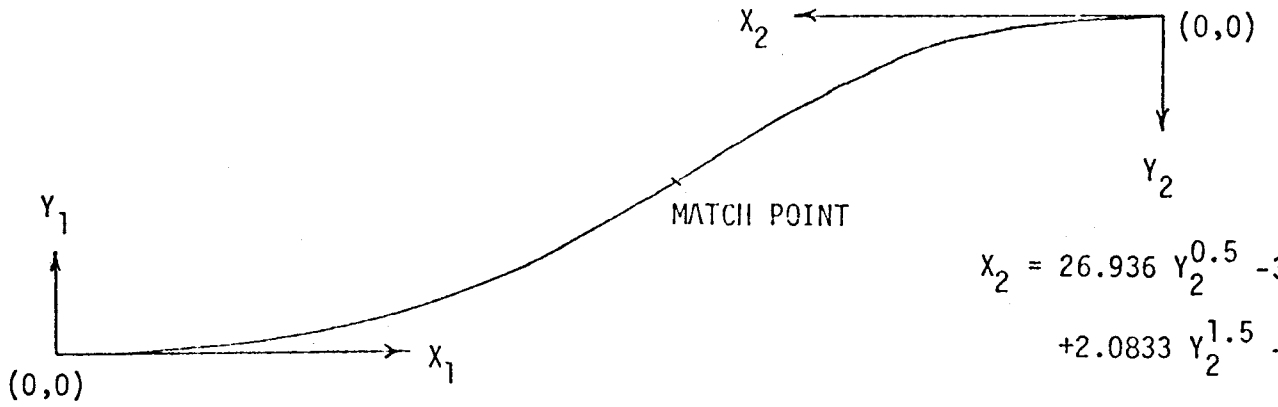

$$X_2 = 26.936\ Y_2^{0.5} - 3.8217\ Y_2^{0.25} - 8.516\ Y_2 + 2.0833\ Y_2^{1.5} - 0.212\ Y_2^{2}$$

$$X_1 = 4.486\ Y_1^{0.5} + 4.7085\ Y_1 - 3.5507\ Y_1^{1.5} + 1.6774\ Y_1^{2} - 0.53\ Y_1^{2.25}$$

FIG 2.2 JET NOZZLE CONTRACTION PROFILE.

specifically for this investigation but was obtained from a wind tunnel at Syracuse University, New York in the Department of Mechanical Engineering. The inner surface of the nozzle has undulations with characteristic dimensions of 2 mm and below. This irregularity would serve to trip the boundary layer and increase the initial fluctuation levels.

Two traversing mechanisms were used to position the two probes used in the experiments; a four axis traverser and a two axis traverser. The four axis traverser, discussed in Ref. (23), can traverse the probe (183 cm, 122 cm, 122 cm, 360°) in (x, y, z,θ) coordinates. The traverser was aligned with the jet flow axis to within a maximum misalignment of 0.1 degrees (the limitation being the size of the probe used to measure velocity contours across the flow). The movements along the axes are powered by stepping moto which are operator controllable through a Intel-8085 Microcomputer.

Great care was taken to keep all parts of the traversing mechanism out of the main flow field and to cause minimal obstruction in the entrainment velocity field. The vertical axis was fashioned with an L-shaped overhang (60 x 60 cm) for the probe mount, held rigid by tensioned guy wires to minimize flow induced vibrations. This feature caused only part of the probe holder to be directly in the flow (far downstream of the probe, of course) and held to a minimum the effects on the potential flow field.

The smaller traverser had an (x,y) travel of (145 cm, 50 cm) along with another degree of movement of 40 cm in the z direction. See Figure 2.3. This traverser was aligned in the flow using the four axis system as referenc

The small traverser was used to locate the fixed probe in space while the large traverser was used to locate the moving probe. The amount of movement could be programmed on the microcomputer or the microcomputer could jog the traverser along reference scales fixed on each of the axes, the error

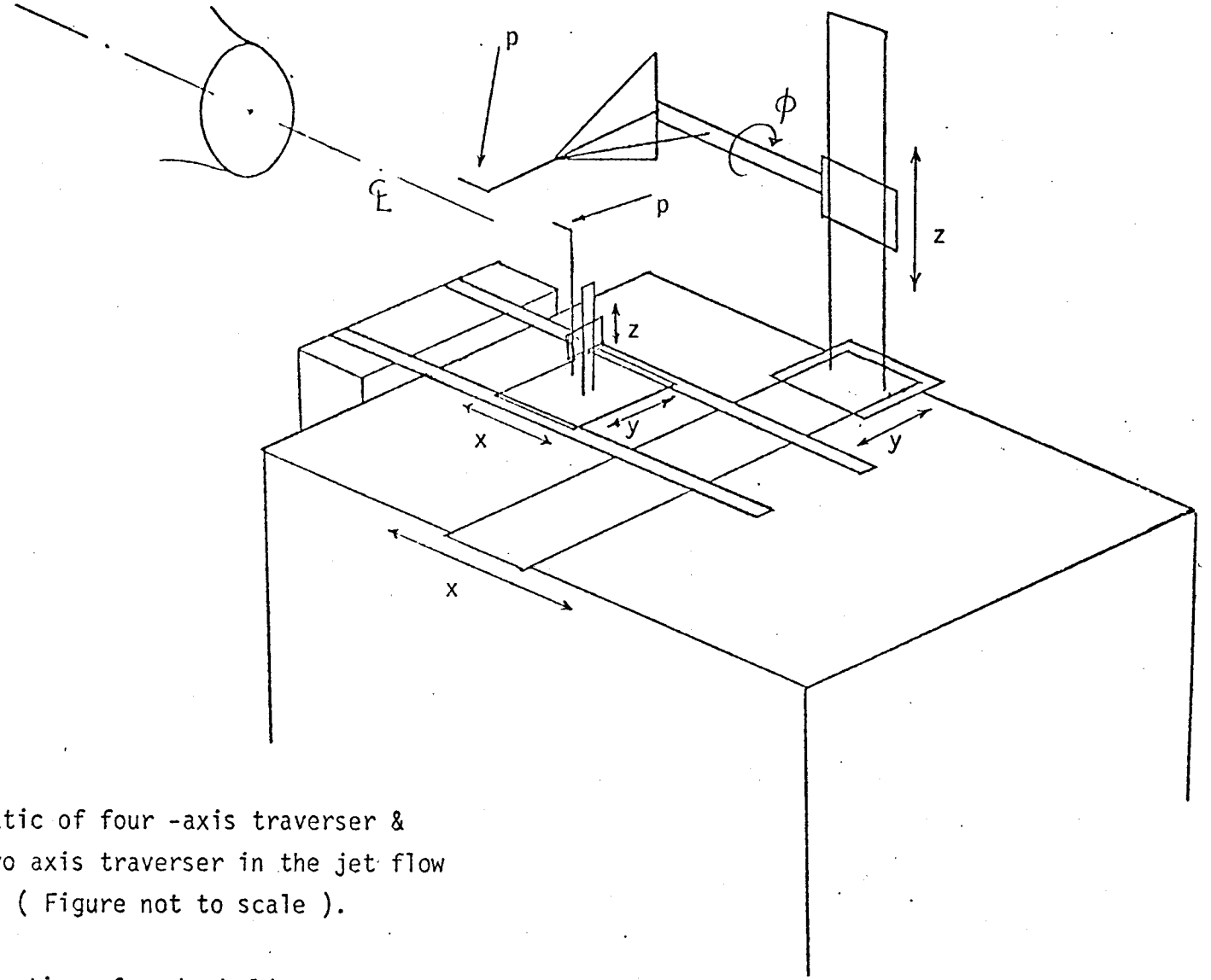

FIG 2.3 Schematic of four -axis traverser & the two axis traverser in the jet flow field. (Figure not to scale).

p. Location of probe holders.

of the visual reference being about 0.5 mm (1/4 the length of the sensor).

The entire facility is enclosed in a large 4 x 12 x 5 m room covered with mylar (this results in a closed flow circuit). The enclosure is locate in a large 20 x 20 x 6 m laboratory room, which is a part of the Turbulence Research Laboratory.

CHAPTER 3

3. General Instrumentation and Calibration

For sensing velocity in the flow field, DISA 55P01 hot wire probes were used (Figure 3.1). Each wire was 5 μm in diameter and 2 mm long, givin an L/D ratio of 400. The wires were made of tungsten with platinum plating and gold-plated prongs; they were also plated on the inactive length that wa welded to the prongs. Each probe formed one arm of DISA 55M10 Constant Temperature Anemometer bridges which was used in conjunction with DISA 55M01 Anemometers (Figure 3.1).

The anemometer bridges were set to provide a wire overheat ratio of 1.8 The frequency response limit (with the high frequency filter setting) was se at 120 KHz and the AC gain (with the amplifier gain setting)was 1000. 5 m long cables were incorporated in the probe arms of the bridges and the syste were tuned with a square wave test to less than 10% overshoot. This was first done at a step higher gain setting than mentioned above, and then reduced one step thereby obtaining extremely stable operation for the bandwidt of interest (DC-6KHz).

The bridge top voltages from the anemometers were connected to the inpu of DISA 55M25 linearizers (Figure 3.2). The linearizers accomplished the linearization of the anemometer signals by means of analog computers each having a transfer function composed of an exponential and a square root function. For the flow conditions under discussion the square root function was not necessary and hence was not used. The linearizers could be programme by means of thumbwheel selectors to obtain an exponential transfer function with an exponent which increased with anemometer output voltage (increase in flow velocity). The exponent factors and variable exponent levels were fine tuned by calibrating over the entire flow range repetitively. Ultimately the

Pt-plated tungsten wire, diameter 5 μm, overall length 3mm, sensitive wire length 1.25 mm. Copper and gold plated at the ends to a diameter of approx. 30 μm.

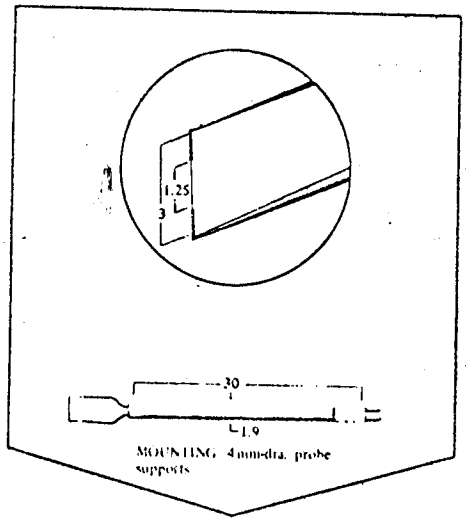

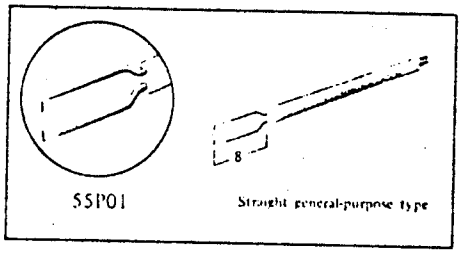

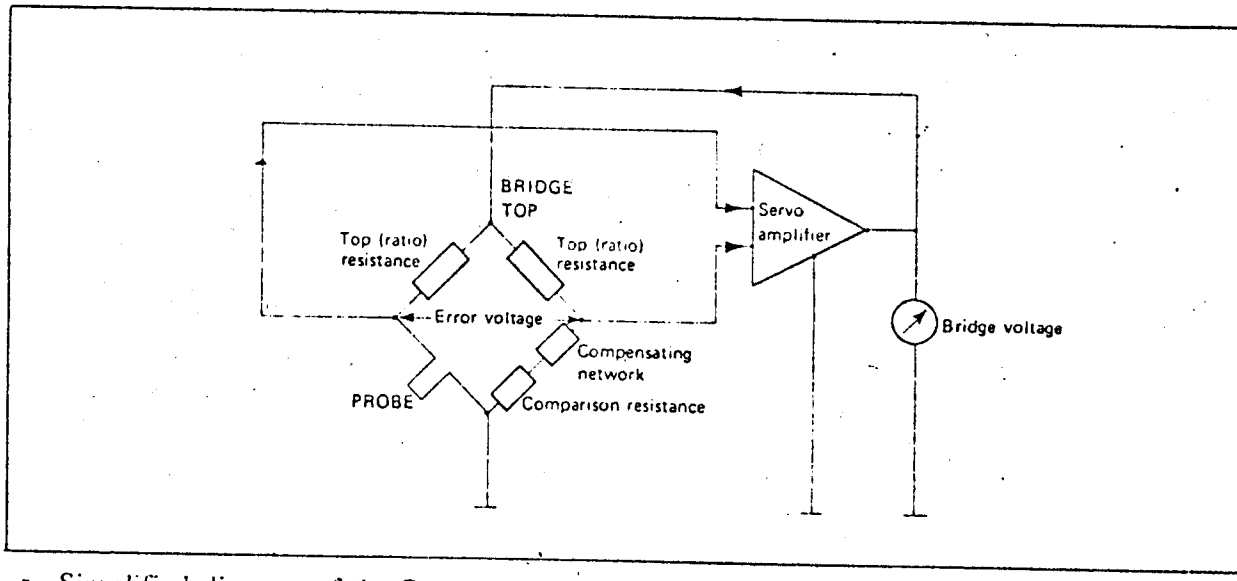

FIG 3.1 Simplified diagram of the Constant-temperature Anemometer.

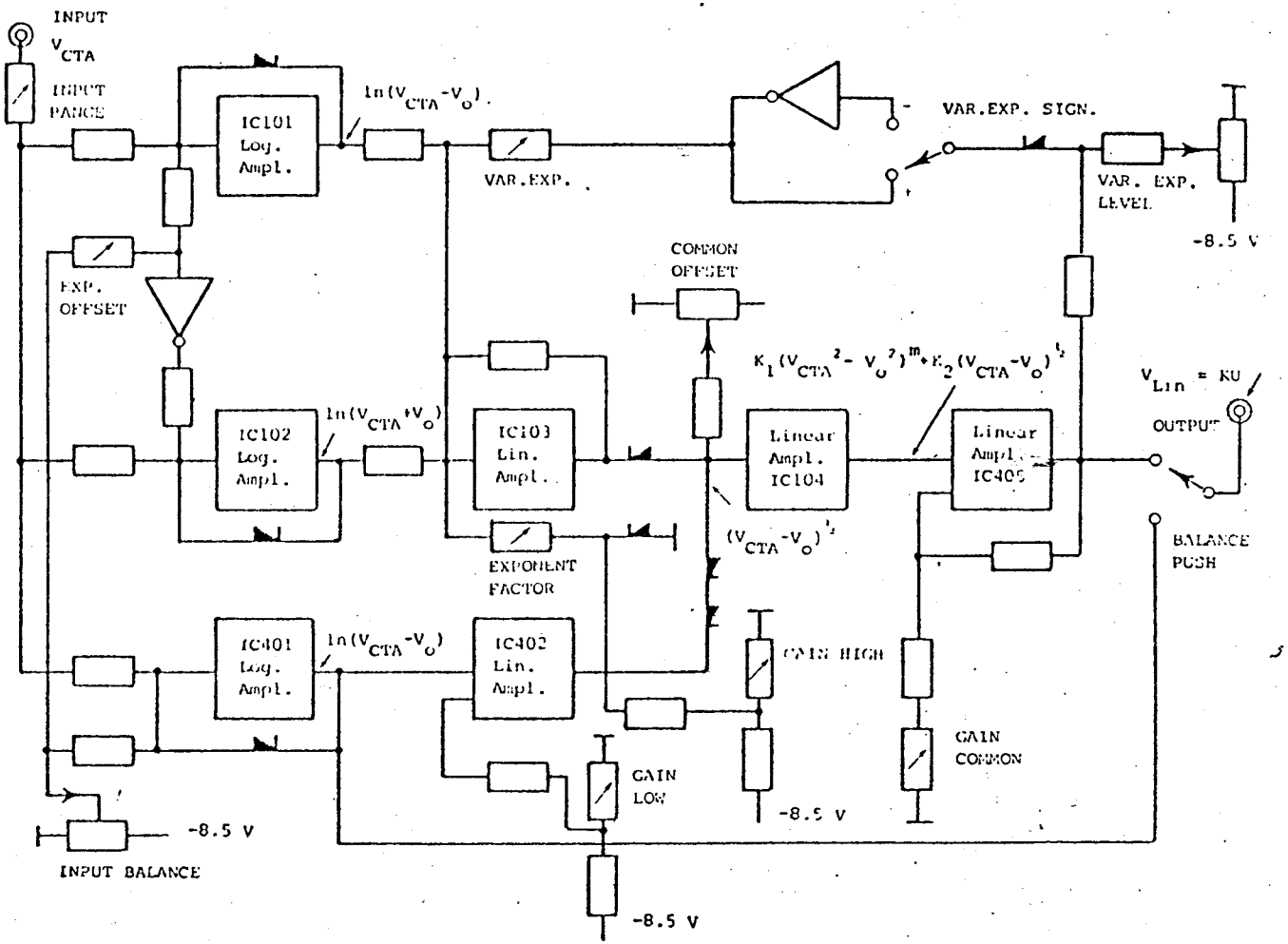

FIG 3.2 Simplified block diagram of DISA 55M25 Linearizer

output signals from the linearizers were linear to within 0.5% of a true straight line in the velocity range of 1 m/s to 40 m/s. The limitation being primarily the step size in the adjustments to the transfer functions on the analog computers of the linearizers.

During exploration of the capabilities of the DISA 55M25 Linearizer, it was discovered that the effect of the step size of the adjustments to the transfer functions was progressively minimized when using higher output gain Thus with the flow range of 1-40 m/s and a DC output from the linearizer of 0-50 volts, the maximum inaccuracy was brought down to 0.2%. But this high output level is not compatible with any of the instruments used to process the signals. Thus a 0-10 volt output was used for which the aforementioned linearization limitation was applicable.

When sampling the signals on the AR-11 A/D Converter in the PDP 11/34 Minicomputer the output of the turbulence signals from the linearizers had to be kept down to ± 2.5 volts. This required a DC output of 0-5 volts from the linearizer, and in this case, linearization was off by $\pm 2\%$. Thus a curve was fitted to the linearizer output and information from such curves was used to convert voltage information to velocity information.

For a perfectly linearized CTA the effective cooling velocity is:

$$u_{eff} = \sqrt{(U+u')^2 + v'^2} \tag{3.1}$$

For small turbulence intensity, the radical can be expanded in a binomial series. Expanding and averaging results in:

$$\overline{u_{eff}} = \bar{U}\left[1 + \frac{\overline{v'^2}}{2U^2} + O\left(\frac{u'}{U}\right)^3\right] \tag{3.2}$$

For the measurements under discussion in subsequent chapters the effect of the factor involving the cross stream component of velocity, v', in

equation (3.2) is expected to be less than 10%. This estimate is based on the measurements being taken at locations of relatively low turbulence intensity, u'/U_e, only.

The system (anemometers + linearizers) was calibrated in two jet facilities: A small 7.62 cm diameter jet with a velocity range of 1-23 m/s, and the large one (described in Chapter (2)) with a velocity range of 13 m/s to 40 m/s.

A pitot-static tube, precalibrated for measurements in air for low subsonic ranges, was used as a reference for jet exit velocity. A micro-manometer was used to measure the velocity head in the large jet while in the small jet a Validyne differential pressure transducer was employed to give a digital readout of the pitot-static pressure difference. For the micro-manometer the velocity was related to the liquid head as:

$$\overline{U}_e = 0.88515 \sqrt{h}\ \sqrt{T}$$

$\overline{U}_e$ in m/s, h in inches of water, T in degrees Rankine for ambient air.

The entire system was mounted on castors and was moved from one facility to the other repeatedly because linearization required iterations between the entire velocity range. The ratio U_e/E where E is the linearizer output voltage and U_e is the jet exit velocity, varied with the ambient temperature of the room as follows:

+ 1.7% per °C rise, -1.6% per °C drop

over a temperature range from 25 to 31 °C. This was established by recalibrating after every degree change in blower intake temperature.

From the preceeding considerations, a calibrated linear signal representative of velocity fluctuations in a Eulerian frame of reference in the jet flow field was available from each sensor. Before being analyzed the signal

were sent through DISA 55D26 Signal Conditioners (Figure 3.3). The signal could be amplified, DC suppressed, low pass filtered and high pass filtered. Filters used in the signal conditioners were 18 dB/oct Butterworth filters. Both the signal conditions were extensively tested at different high and low pass settings for phase matching. White noise was input to both filters at identical settings and the transfer functions and phase difference spectra were closely examined. The two filters were found to be phase matched to within 0.5% of each other for up to 6.3 KHz low pass. Higher low pass settings were not checked because 6 KHz is about the probe attenuation roll off frequency in the center of the mixing layer at maximum jet velocity. A sensor placed in a flow field is only sensitive to disturbances with spatial scales larger than twice the largest dimension of the sensor. Thus

$$f_o = \frac{U_c}{2\ell_w}$$

where

f_o = probe wire attenuation roll of frequency. ≈6 dB/oct

U_c = local convection velocity

ℓ_w = sensor length

The signal conditioners were adjusted differently for different measurements, the appropriate settings will be mentioned individually in the descriptions of the particular measurements.

For computing cross correlations between two signals a DISA 52B25 Signal Processor was used. The features used on that device were A.C. coupling and an analog multiplying circuit. With A.C. coupling the -3dB point was tested to be at 1.6 Hz with a -6dB/oct RC filter.

A square wave test on the signal processor revealed that the instrument begins distorting a square wave at 5 KHz and the distortion becomes pronounced beyond 10 KHz. With a gain of 1 the instrument had an input window of $\pm$ 10

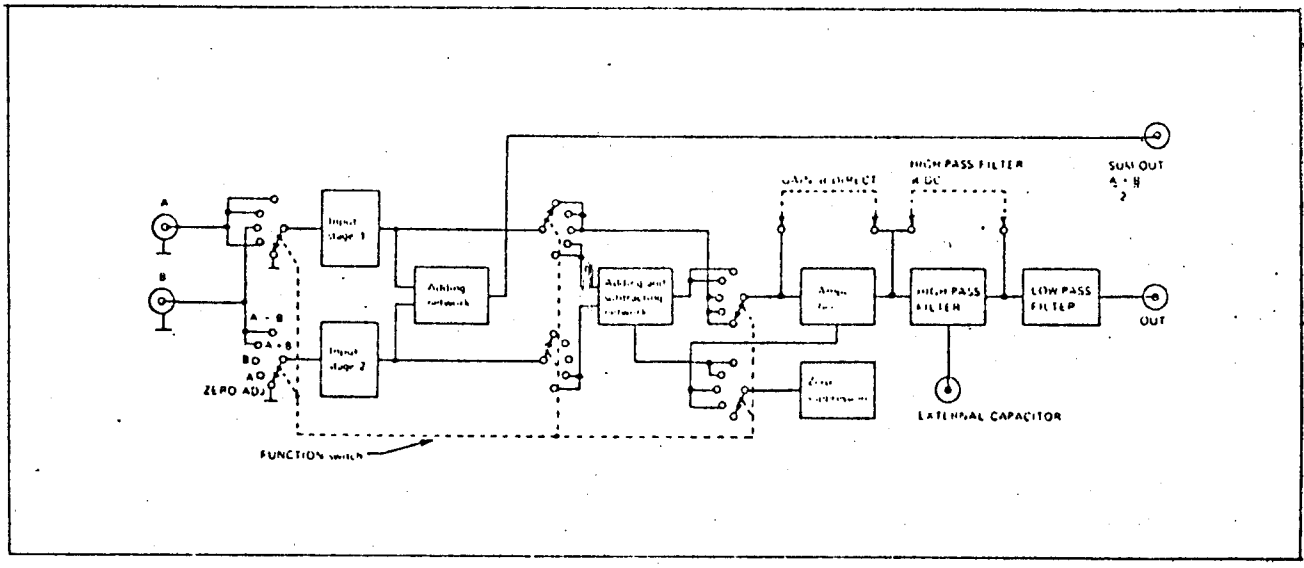

Block Diagram of the 55D26 Signal Conditioner.

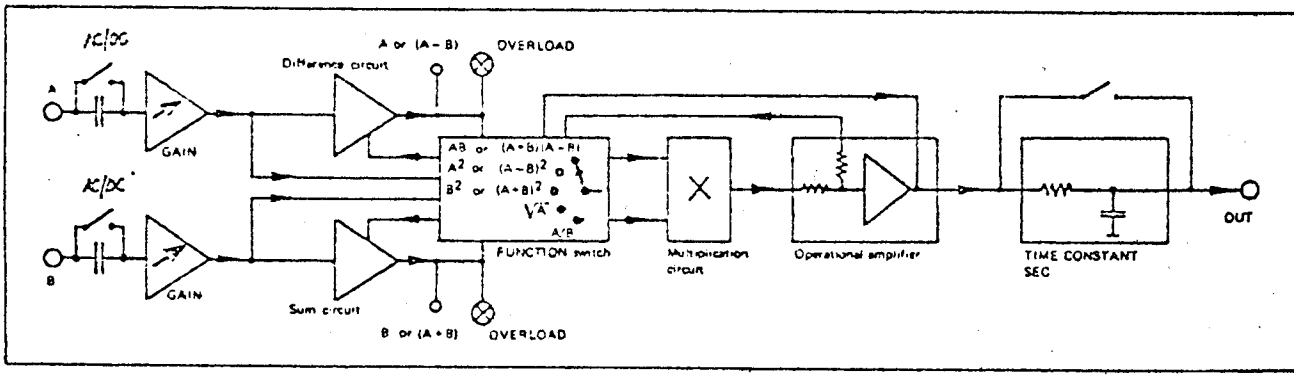

Block diagram of the 52B25 Turbulence Processor

FIG 3.3

The instrument was used with a gain of 1 to prevent the characteristics of the amplifiers from having an effect on the shape of the signals. Calibrating the multiplying circuit of the processor with mean square meters revealed an inaccuracy of +2% on a sine wave test at 5 KHz and +5% on a square wave test at 5 KHz. During measurements the output of the processor had a fixed bias of +0.02 volts, which was subsequently corrected in the da

For measuring mean and r.m.s. values of the conditioned and processed signals TSI 1076 voltmeters and DISA 55D31 voltmeters were used. The voltmeters were carefully calibrated with square waves using a Tektronics facto calibrated oscilloscope as a reference.

For computation of correlations (space-time) and spectral analysis a PDP 11/34 minicomputer and a Nicolet 660A two channel FFT Analyzer were use The features and application of these two processors are discussed in Chap.

4. Mean Flow Characteristics

Mean and r.m.s. values of the x component of velocity were measured in the 20.57 cm diameter jet from the linearized hot wire signals using DC and r.m.s. voltmeters. The instrumentation schematic is shown in Figure 4.1. For DC measurements a 30 sec. integration time constant was used for averaging while for r.m.s. measurements a 100 sec. integration time constant was found to give a steady-state error envelope of $\pm$ 1%; that being an acceptable level of accuracy. The mean and r.m.s. voltages were then decomposed into mean and r.m.s. velocities by multiplying them by the calibration constants.

For the profiles reported in this chapter the jet exit Reynolds number based on the diameter was:

$$Re_D = 5.4 \times 10^5$$

Traversing across the mixing layer was done along the r-axis of the jet and the sensor length was kept tangential to the velocity contours. For definition of coordinate system see Figure 4.2.

4.1 Measurements at the Exit Plane

The exit profile was measured to be flat to within 0.1%. The turbulence intensity at the exit plane on the jet center line was

$$\frac{u'}{U_e} = 0.0033 \quad \text{or} \quad 0.33\%$$

Boundary layer measurements were not made *per se* at the exit plane, but from spectral analysis the boundary layer was seen to be turbulent and the boundary layer thickness was approximated to be 4 mm. The power spectrum measured at the exit plane is presented in Chapter 5.

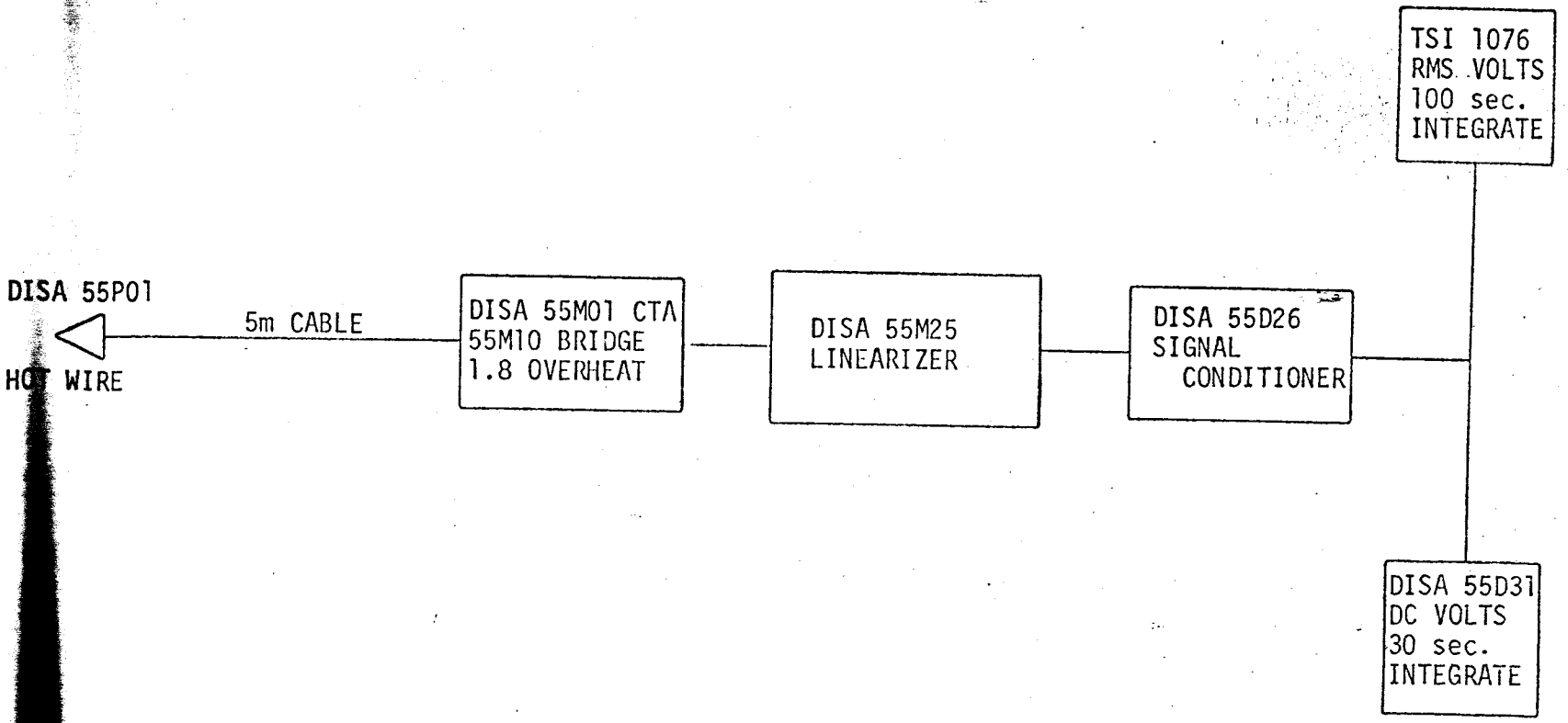

IG 4.1 INSTRUMENTATION SCHEMATIC FOR MEAN FLOW PROFILE MEASUREMENTS.

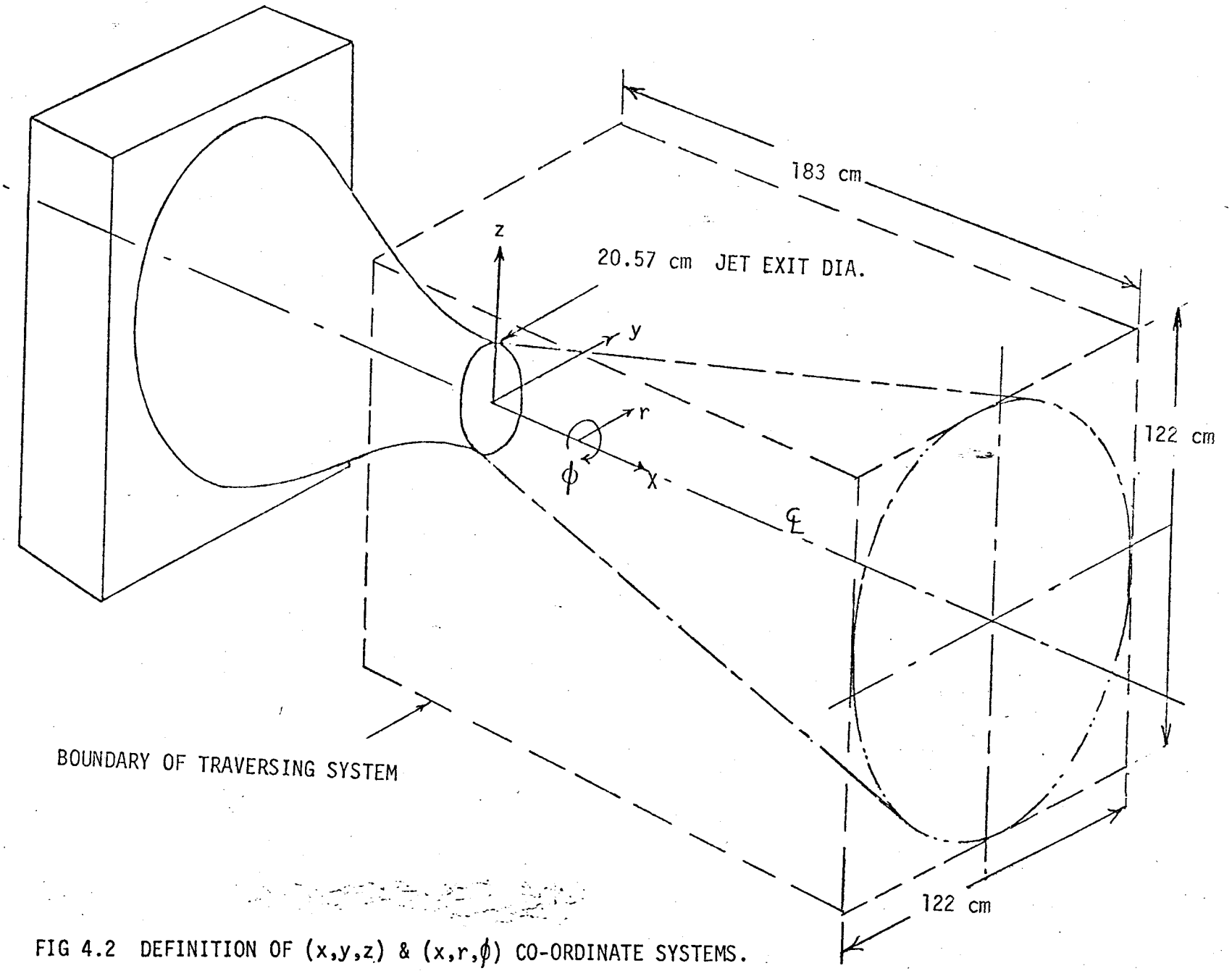

FIG 4.2 DEFINITION OF (x,y,z) & (x,r,ϕ) CO-ORDINATE SYSTEMS.

4.2 Measurements Across the Mixing Layer:

Measurements across the mixing layer were recorded at x/D of 1, 2, 3, 4 and 5. The mean velocity profiles are presented in Figure 4.3.

From the measured mean velocity profiles the momentum thickness was computed by graphically integrating each profile. The momentum thickness is defined as

$$\theta = \int_0^\infty \frac{\overline{U}}{\overline{U}_e} \left(1 - \frac{\overline{U}}{\overline{U}_e}\right) dr$$

or by finite difference approximation:

$$\theta = \sum_{i=1}^{i=n} \left(\frac{\overline{U}}{\overline{U}_e}\right)_i \left[1 - \left(\frac{\overline{U}}{\overline{U}_e}\right)_i\right] \Delta r \qquad (4.1)$$

Note that the mixing layer is sufficiently thin that the radial spreading can be neglected and a two-dimensional flow approximation is appropriate. The integration was terminated at $\overline{U}/\overline{U}_e = 0.1$, because beyond this point the contribution to the integral is diminishingly small (Figure 4.3). The momentum thicknesses are shown in the table below.and are plotted in Figure

The Reynolds numbers based on θ and $\overline{U}_c = 0.6\ \overline{U}_e$ at the five locations across the mixing layer are shown in Table 4.1.

Table 4.1

x/D	θ	Re_θ
1	1.074 cm	1.7×10^4
2	1.816 cm	2.87×10^4
3	2.59 cm	4.1×10^4
4	3.367 cm	5.3×10^4
5	4.135 cm	6.55×10^4

As shown in Figure 4.4 , the momentum thickness would be zero at x/D = -0.34 or 7.0 cm upstream of the exit plane. This indicates that the shear layer

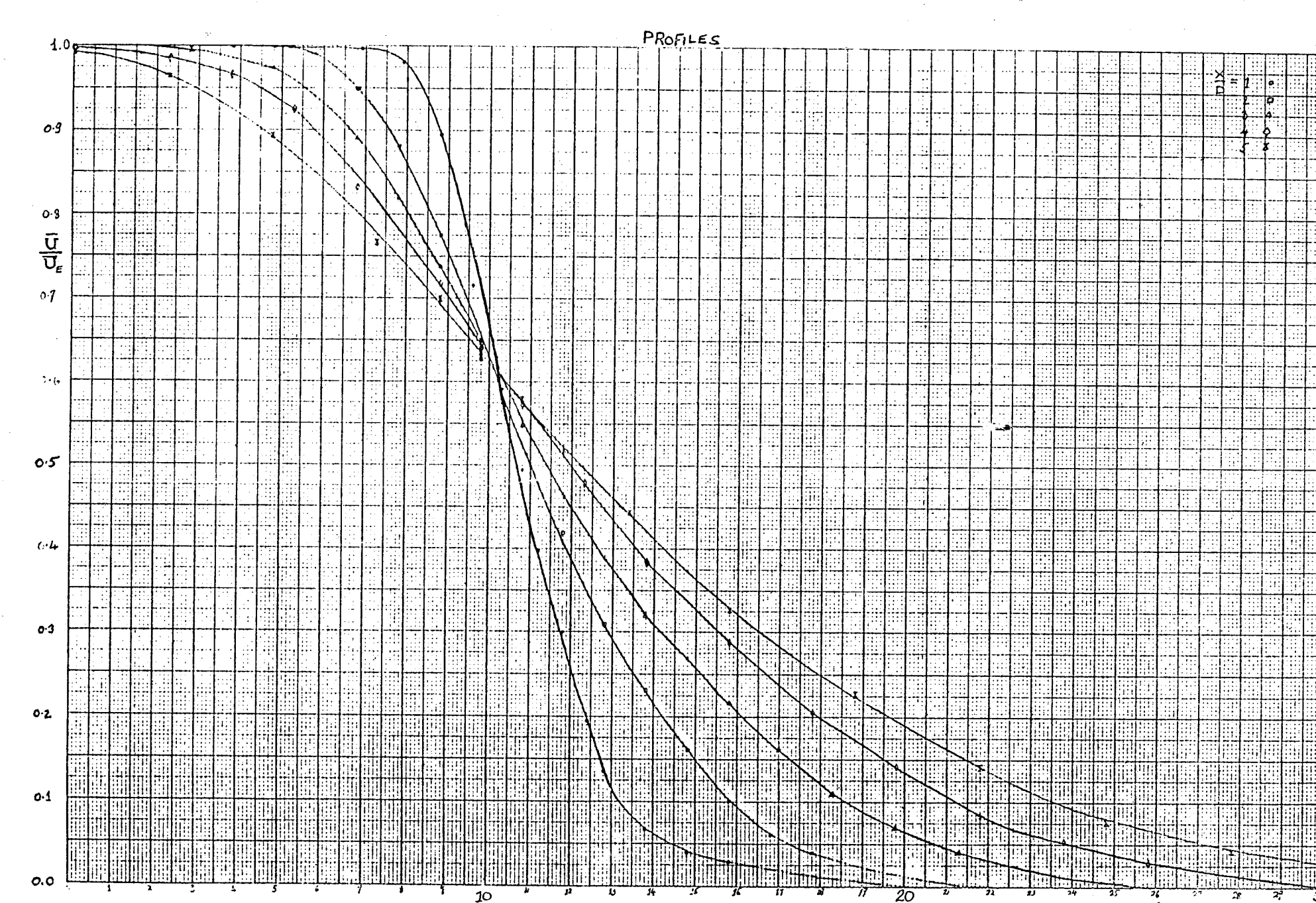
PROFILES
1.0
0.9
0.8
0.7
0.6
0.5
0.4
0.3
0.2
0.1
0.0
$\frac{\bar{U}}{U_E}$
10
20

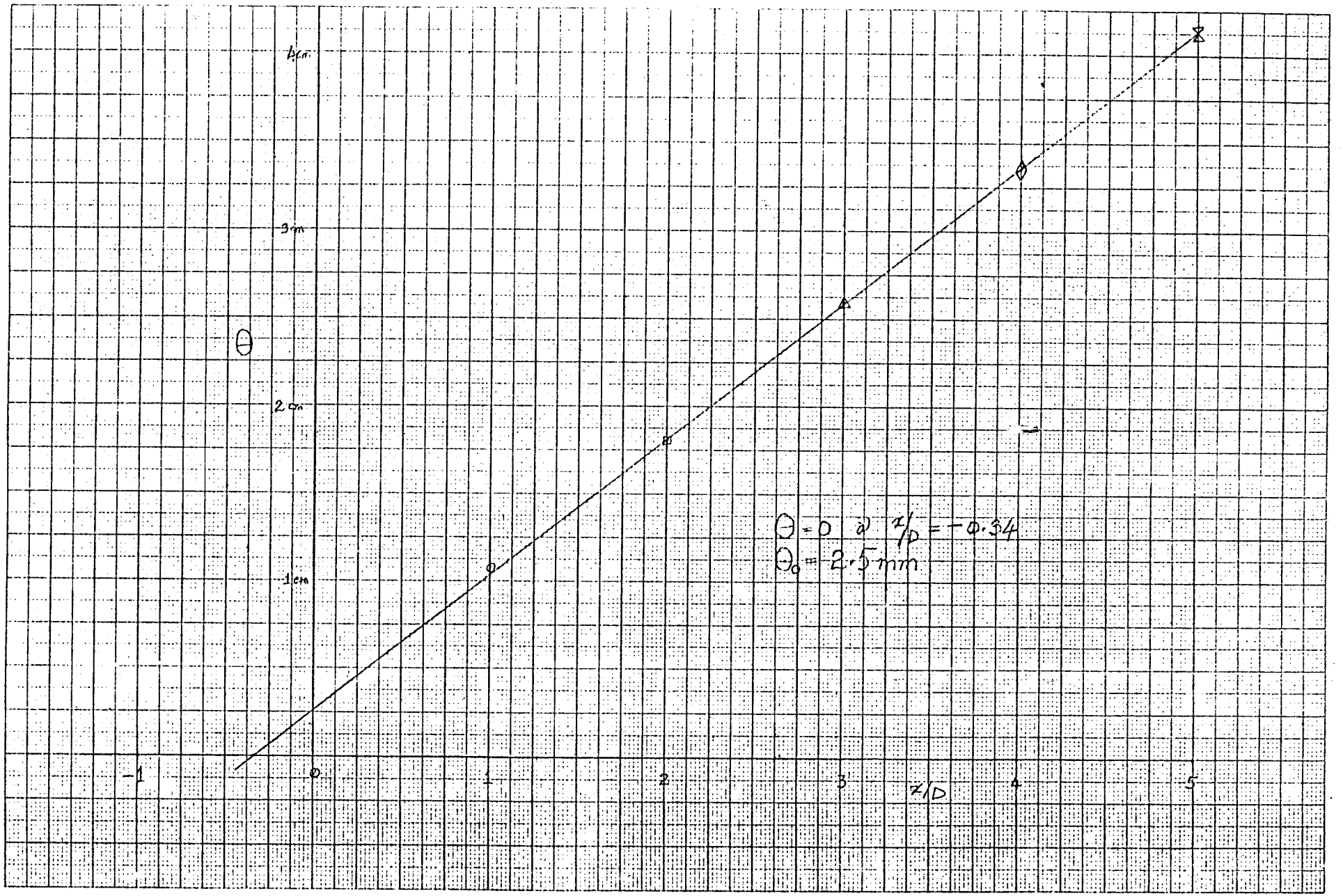
4cm
3cm
2cm
1cm
θ
-1
0
1
2
3
4
5
x/D
θ = 0 à x/D = -0.34
θ0 = 2.5 mm

has its virtual origin at x/D = -0.34. This observation is consistent with recent measurements of Hussain & Zedan (15) for initially tripped boundary layers in an axisymmetric jet.

The Reynolds numbers based on the local r.m.s. velocity in the center of the mixing layer and the integral scale (based on $\mathcal{L} = 0.08x$) at the five x/D locations are shown in Table 4.2.

Table 4.2

x/D	Re_T
1	7.46×10^3
2.	1.459×10^4
3.	2.12×10^4
4	2.8×10^4
5	3.37×10^4

The Reynolds number at x/D of 1 is very low for fully developed turbulence to exist and, as will be discussed later, the turbulence intensity profiles for x/D=1 do not collapse very well with the rest of the data.

Momentum flux conservation was checked by integrating the mean velocity profiles. At the exit plane the momentum flux was approximated by

$$\frac{1}{\rho} M_o = \frac{\pi}{4} D^2 \overline{U}_e^2 \qquad (4.2)$$

This being a very slight over estimate, because the estimate assumes no boundary layer along the circumference. At any other downstream location the momentum flux would be

$$\frac{1}{\rho} M_x = 2\pi \int_0^\infty r \overline{U}^2 \, dr$$

$$\frac{1}{\rho} M_x = 2\pi \overline{U}_e^2 \int_0^\infty r \left(\frac{\overline{U}}{\overline{U}_e}\right)^2 dr$$

or approximately:

$$\simeq 2\pi \overline{U}_e^2 \sum_{i=1}^{i=n} r_i \left(\frac{\overline{U}}{\overline{U}_e}\right)^2_2 . dr \qquad (4.3)$$

The plots of the profiles that were integrated are shown in Figure 4.3 . At x/D of 5 the momentum flux obtained from equation (4.3) was 98% of the initial momentum flux estimate computed from equation(4.2).

4.3 Analysis of Results:

Recent measurements by Nagib (20) and Hussain et al. (14,15) indicate a strong dependence of the initial growth of the mixing layer on exit conditioning in an axisymmetric jet. Since the exit condition mentioned in Section 4.1 is a highly turbulent initial boundary layer at the jet lip, some discrepancy in the similarity profiles is expected with measurements of other investigators in the initial developing region of the mixing layer.

To facilitate comparison with measurements done by other investigators the profiles were also plotted with x-ordinate normalization.

Figure 4.5 and 4.6 show plots of $\overline{U}/\overline{U}_e$ and $u'/\overline{U}_e$ with their radial coordinates normalized by the downstream distance, x, from the exit plane and by the momentum thickness of the shear layer at that x/D location, respectively.

The data collapses better with the momentum thickness than with the axial distance from the exit, primarily because with an initially turbulent boundary layer the virtual origin of the free shear layer is upstream of the exit plane. The momentum thickness is a better scale for self similari

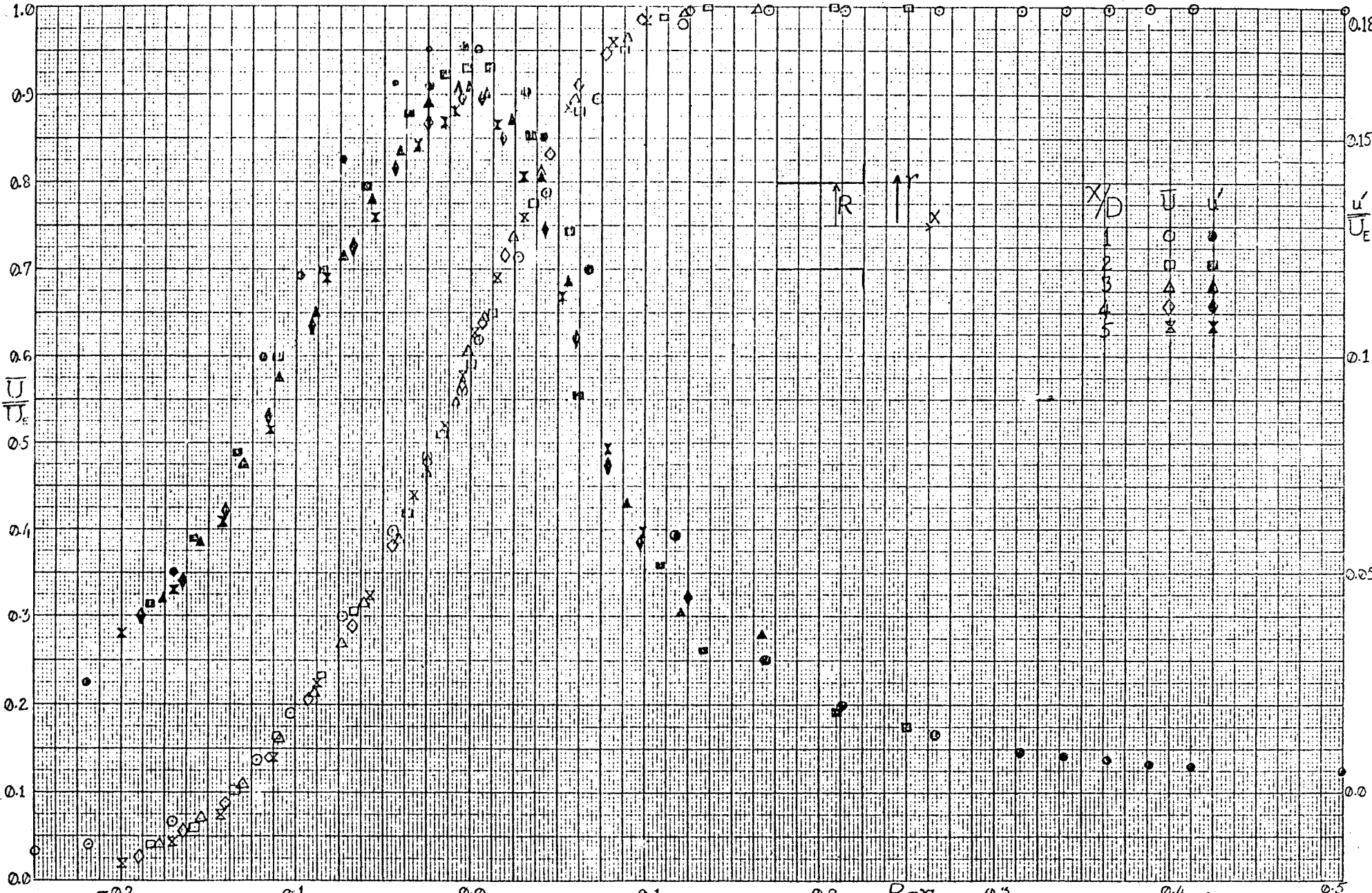
1.0
0.9
0.8
0.7
0.6
0.5
0.4
0.3
0.2
0.1
0.0
$\frac{\overline{U}}{U_E}$
0.18
0.15
0.1
0.05
0.0
$\frac{u'}{U_E}$
R
r
X/D
1
2
3
4
5
$\overline{U}$
u'
-0.2
-0.1
0.0
0.1
0.2
0.3
0.4
0.5
r=X

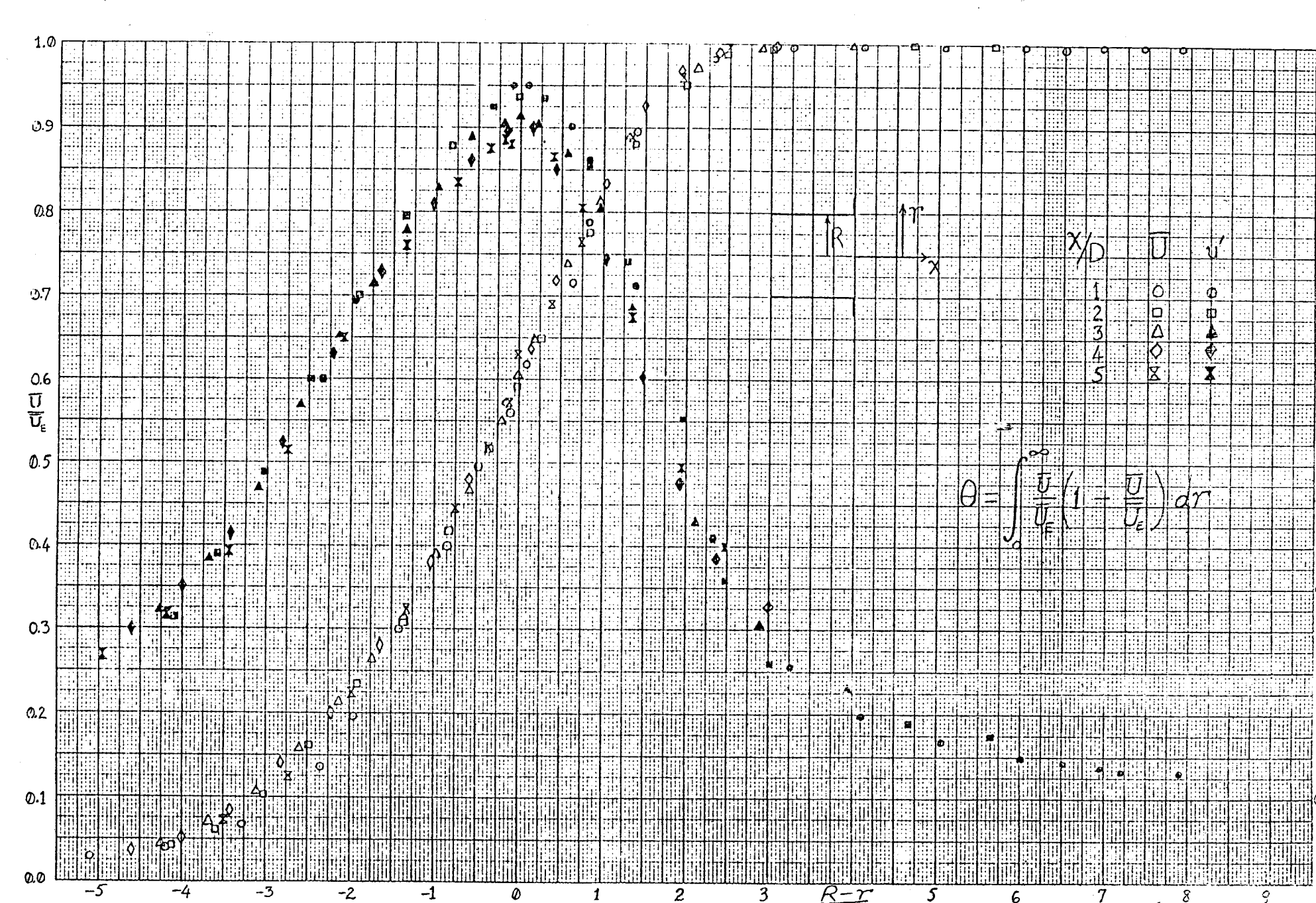
1.0
0.9
0.8
0.7
0.6
0.5
0.4
0.3
0.2
0.1
0.0
$\frac{\bar{U}}{\bar{U}_E}$
-5
-4
-3
-2
-1
0
1
2
3
R-r
5
6
7
8
9
R
r
x
x/D
$\bar{U}$
u'
1
2
3
4
5
$\theta = \int_0^\infty \frac{\bar{U}}{\bar{U}_E}\left(1 - \frac{\bar{U}}{\bar{U}_E}\right) dr$

in the absence of exact knowledge of the virtual origin. Based on the momentum thickness being zero, the virtual origin would be at x/D = -0.34 for this particular jet, as discussed previously.

The profiles from x/D of 1 do not collapse very well with the rest of the data, especially the $u'/\overline{U}_e$ profile. This can be attributed to the shear layer not having become self similar yet and that the self preserving region begins close to x/D of 1.5.

The maximum turbulence intensity based on the exit velocity was 0.17 (or based on the local velocity it was 0.28 in the center of the mixing laye At about x/D of 4.5 the center line velocity begins to drop below $\overline{U}_e$ thus indicating the end of the potential core and the merging of the axisymmetric mixing layer into a fully developed jet.

The mean velocity and turbulence intensity profiles are in close agreement with hot wire measurements of e.g. Bradshaw et al. (4), Tran (26), Hussain et al. (15), Champagne et al. (6).

An interesting contrast is seen in Figure 4.7 with the recent data of Nee (21), which was acquired by using a Laser Doppler Anemometer System. Since the LDA is sensitive to only the x-component of velocity in Nee's experiment, the data are free of contamination from any other velocity components. It is apparent that below U/U_e = 0.4 the hot wire measured profile are progressively higher than the LDA measurements (the turbulence intensiti in this region, based upon the local mean velocity, are 35% and above). Thi discrepancy can be attributed to the factor involving v' in equation 3.2 becoming significant beyond U/U_e = 0.4 or $(r-R)/x > 0.05$ and to the existence a small radial component of the mean velocity to which the LDA is insensitiv

It should be noted at this point that all the measurements discussed in Chapter 6 were conducted in the range of agreement of LDA and hot wire measured velocity profiles. In this range the effect of contamination by cross stream velocity components is estimated to be below 5%.

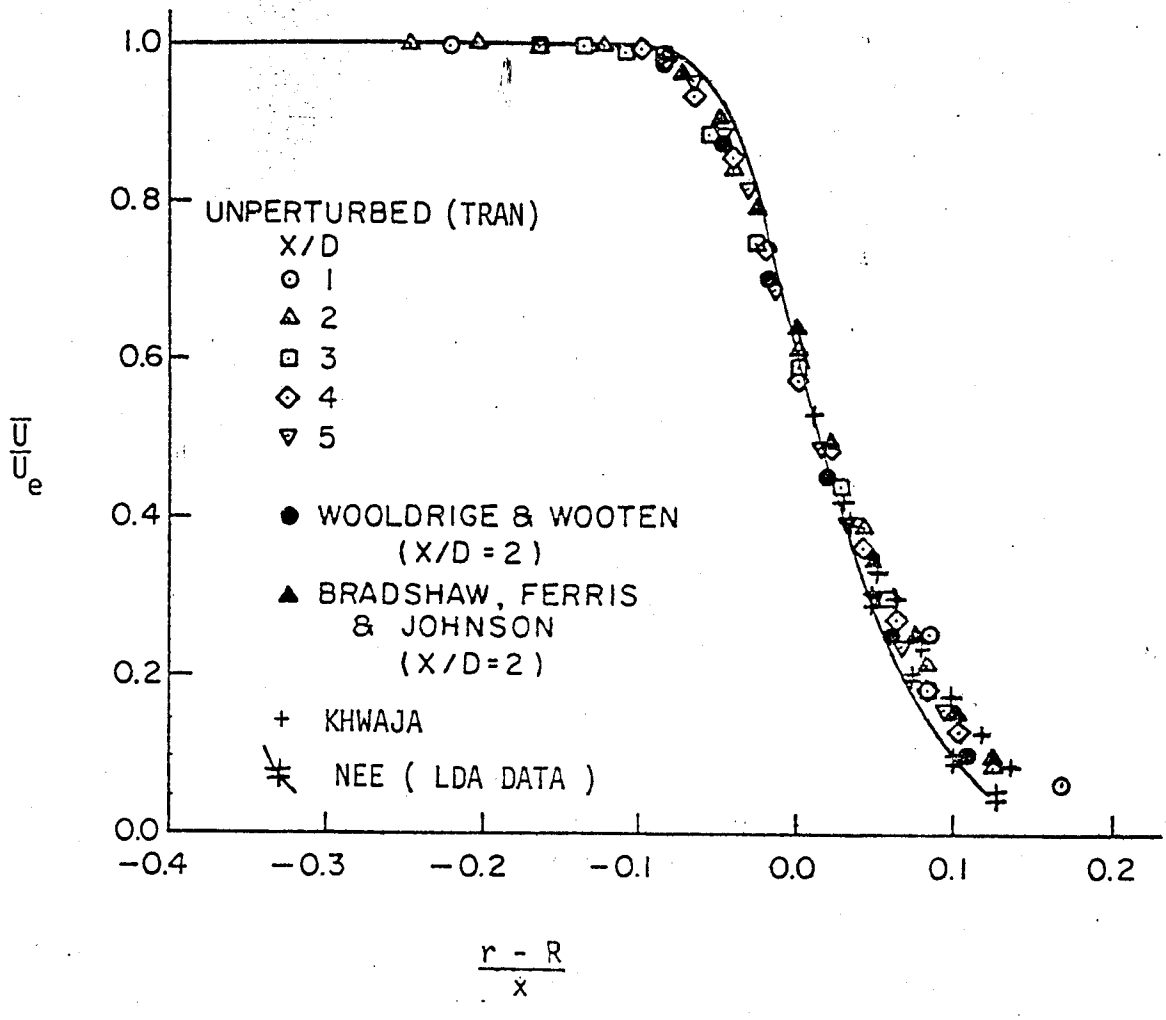

FIG 4.7 Comparison of Hot-Wire & LDA data.

4.4 Establishment of an Intrinsic Coordinate System

An intrinsic coordinate system, along the lines of constant velocity and turbulence intensity, may be defined based on experimental and theoretical evidence.

Figure 4.9 is a plot of constant mean velocity and turbulence intensit isocontours. Figure 4.8 shows similar data from Tran and Sokolov, et al. George (11) discussed the development of similarity in the mixing region from considerations of $R_e \to \infty$ and the basic equations of motion and conclude that beyond $x/D \geq 1$ the effects of initial conditions and viscous effects become insignificant and the shear layer becomes self similar. Figure 4.4 shows that the momentum thickness is linear with x/D in the range $1 < x/D <$

It seems reasonable to treat the mean velocity isocontours as straight lines in the region of $1 < x/D < 5$. The cross-correlation measurements discussed in Chapter 6 were taken in a coordinate system where x is defined as being along a $U = 0.59\ U_e$ isocontour and x' along a $0.4\ U_e$ isocontour in one case and $0.8\ U_e$ isocontour in the other case.

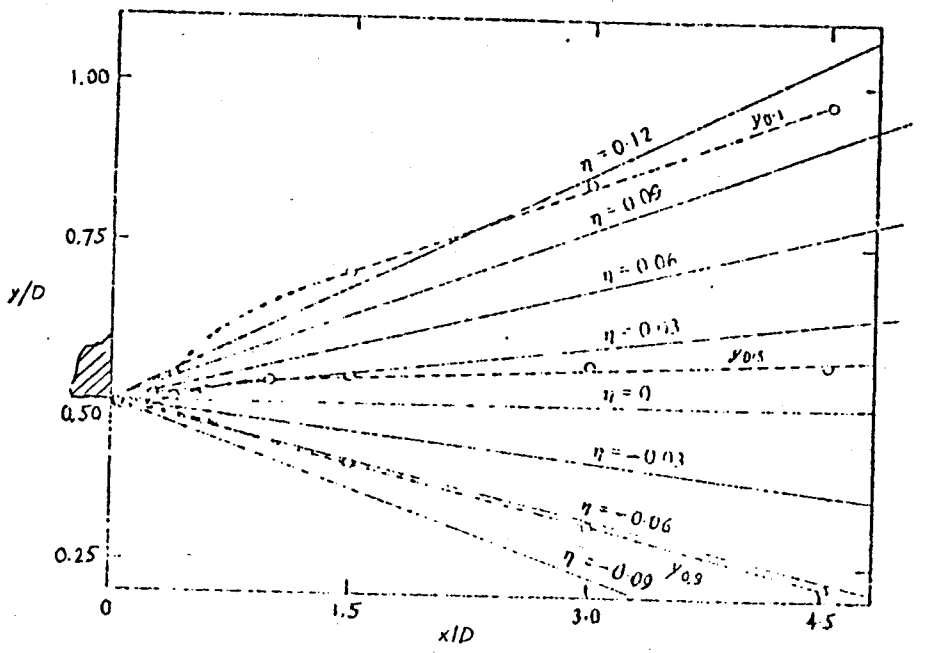

FIG 4.8a Co-ordinate system from Sokolov et al(24)
y_x along $U = xU_e$.

FIG 4.8b Data from Tran (26).

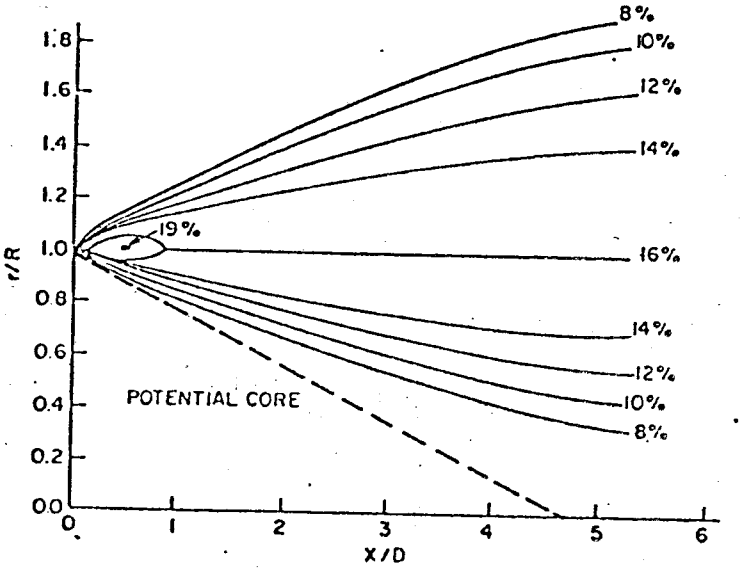

Isocontour of turbulence intensity of unperturbed jet.

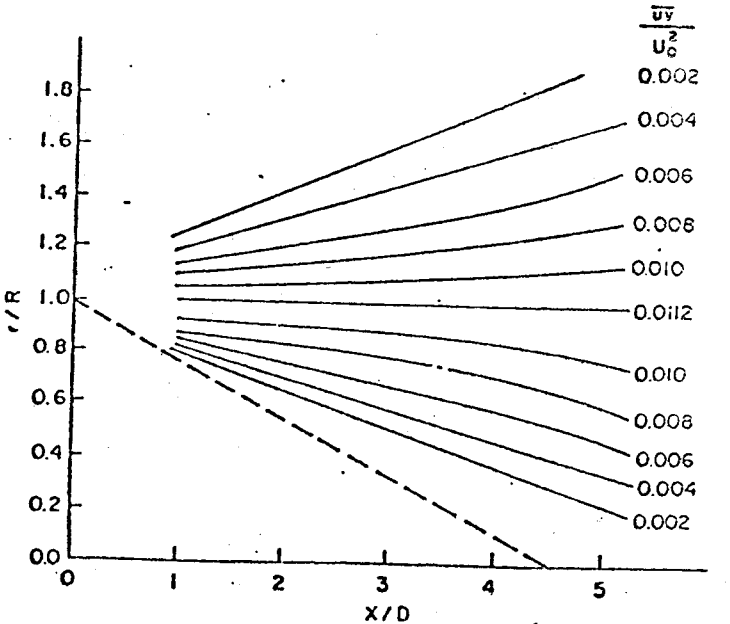

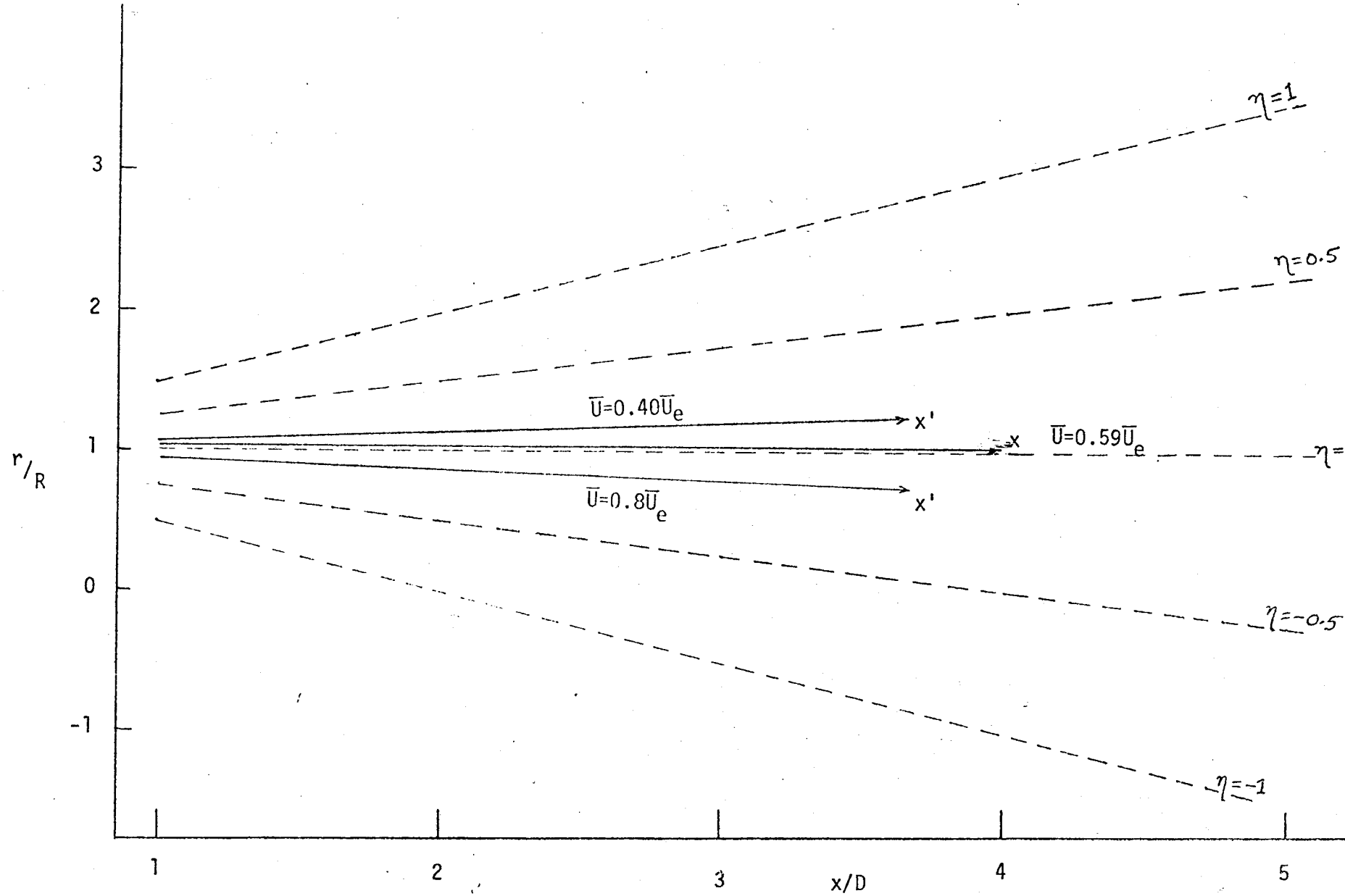

FIG 4.9 - - - constant η lines. ($\eta = \frac{r-R}{x}$). ——— constant $\overline{U}$ & u' lines.

CHAPTER 5

5. Spectral Analysis

5.1 Techniques Used for Spectral Analysis

Spectral analysis was performed on linearized hot wire signals in three different ways. The first method was only used as a calibration check on the second one.

(i) The Wave Analyzer

In the first method a linearized hot wire signal was input to a General Radio wave Analyzer. The instrument is basically a heterodyne receiver (with selectable bandwidths of 5, 10, 25 or 50 Hz) that can be tuned to a frequency of interest. The output of the instrument is an amplitude modulated 100 KHz carrier wave. The mean square of the output when normalized to a bandwidth of 1 Hz, gives the power spectral density of the half line spectrum at the tuned frequency. To obtain a complete spectrum the analyzer had to be tuned to individual frequencies over the entire range of interest. The true velocity spectrum was obtained by multiplying the individual components of the measured spectrum by the square of the linearization constant (from transfer function between $\overline{U}$ and E of the Linearizer-Anemometer system) and by the calibration constant of the wave analyzer.

The calibration constant of the wave analyzer was computed by measuring the spectral height of a low passed white noise signal with the analyzer, and taking the inverse of its ratio with the spectral height computed by measuring the mean square value of the low passed signal. The calibration constant also incorporated the conversion from half line to a whole line spectrum.

$$\text{Calibration constant } C = \frac{N}{N_{meas}(f)} \qquad (5.1)$$

where $N_{meas}(f)$ is the white noise spectral height measured by the analyzer at f (B.W.$< f \leq 0.1\ f_o$)

and $N = \frac{\overline{e^2}}{\pi f_o}$; $\overline{e^2}$ = mean square value of low passed white noise signal

f_o = cut off frequence of -6 dB/oct RC filter

N = True spectral height of white noise signal

(ii) The on-line Minicomputer

The second method of spectral analysis used an on-line PDP-11/34 minicomputer to compute single channel power spectra and two channel cross spectra.

Linearized hot wire signals were low-passed (18 dB/oct roll off) at 6.3 KHz, the frequency corresponding to probe attenuation frequency, to prevent aliasing during digital sampling and D.C. suppressed (not A. coupled by high pass filtering) with the signal conditioners to adjust the signal levels to be within the $\pm$ 2.5 volts window of the AR-11 A/D converter. The AR-11 A/D converter is a 10 bit multi-channel real time module. It has a $\pm$ 2.5 volts input window and the sampling rate is governed by a programmable real time clock. The A/D converter samples sequentially and thus introduces, linearly with frequency, a phase diff erence between two channels. This difference has to be removed in soft ware after the data are recorded.

The conditioned signals were sampled at over twice the low pass filtering frequency and multiple blocks of data were stored on disks. The block sizes used in this investigation ranged up to 1024 wo in length. The sampled data could be viewed on a graphics terminal to

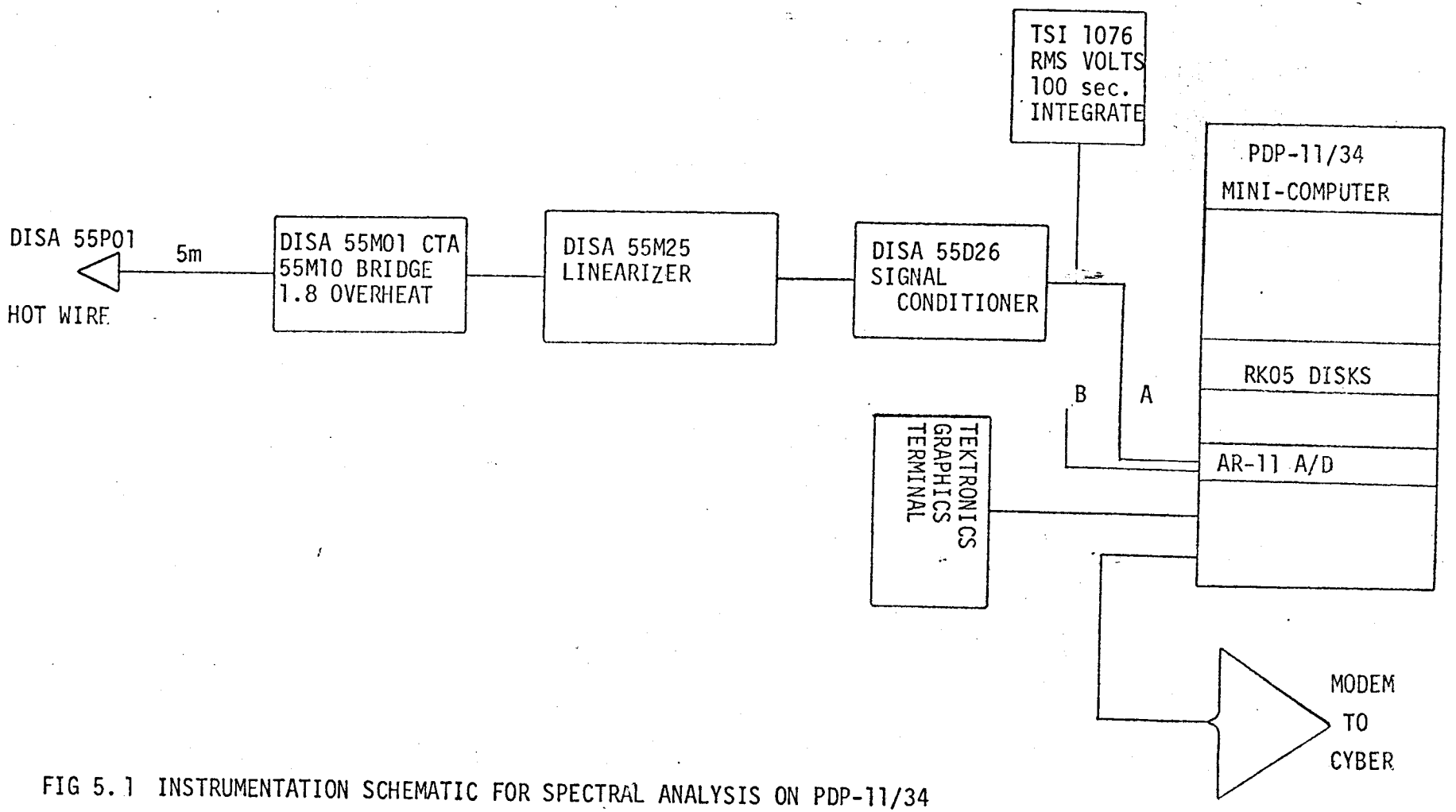

FIG 5.1 INSTRUMENTATION SCHEMATIC FOR SPECTRAL ANALYSIS ON PDP-11/34 MINI-COMPUTER. CHANNEL B IDENTICAL TO CHANNEL A FOR TWO CHANNEL

verify absence of input overflow and adequate window saturation. Fast Fourier transforms on the stored data were performed on every block of data using a software FFT program.

The Fourier components of the transformed data were then accessed by software algorithms to compute single channel power spectra and two channel cross spectra. The multiple blocks of data were used to perform block averaging, and additional software was used to perform spectral smoothing. The whole line voltage spectra obtained were converted to velocity spectra by multiplying each component of a spectrum by the square of the linearization constant. Results could be viewed on a graphics terminal and hard copies were obtained by transferring da via a modem to the University Cyber and running a plotting routine on that computer to plot the spectral data on an x-y plotter.

(iii) The Real-Time Spectrum Analyzer

The third method of spectral analysis used a Nicolet 660A Dual Channel FFT analyzer.

The FFT analyzer is a 12 bit processor which incorporates, among other features, a discretely selectable frequency range, internal anti-aliasing filters (which provide at least 70 dB attenuation of those input frequencies which can cause aliasing), internal sampling frequenc of 2.56 times the selected frequency range, selectable zero to peak input windows (0.1, 0.2, 0.5, 1, 2, 5, 10, 20 volts), parallel sampling between two channels, A.C. (-3 dB at 0.5 Hz) or DC coupling, 2048 point transforms and 800 point spectral computation in single channel mode or 1024 point transforms and 400 point cross spectral computation in dual channel mode, summation or difference averaging, continuous CRT annotat

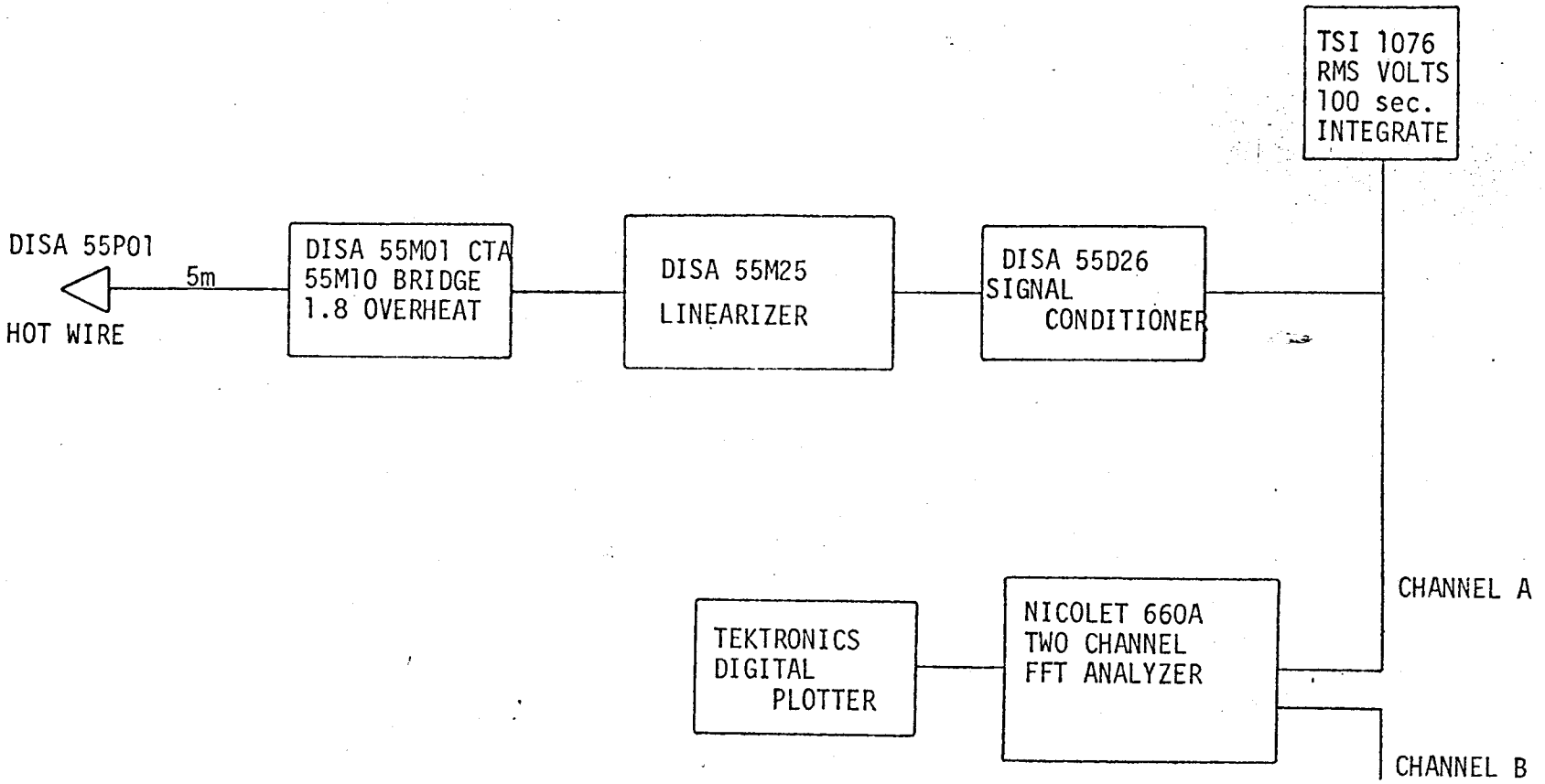

FIG 5.2 INSTRUMENTATION SCHEMATIC FOR SPECTRAL ANALYSIS. CHANNEL B IDENTICAL TO CHANNEL A FOR TWO CHANNEL CROSS-SPECTRAL ANALYSIS, & CROSS-CORRELATION MEASUREMENTS (SPACE-TIME).

display and interfaces with plotters and other external equipment. The overall specifications are summarized in the Appendix.

For computation of single channel power spectra a linearized hot wire signal, low passed at the probe cut-off frequency, e(t) was inpu to the FFT analyzer. The FFT analyzer was operated in a continuous mode so that it computed FFT's on 2048 point blocks of data and compu the power spectra, perfo[1]med "summation" averaging over 1000 such blo (# of averaging up to 29997 blocks) and displayed the results continu ously on a CRT. After the desired level of smoothing was achieved by block averaging the flow was turned off and the room allowed to stabi The FFT analyzer was run for another 1000 blocks, this time the aver was "difference", viz. subtracting the present spectrum from the pre- viously computed block averaged one. Running in this mode for the sa number of blocks as the summation averaging served to eliminate all background noise from the computed spectra.

When data are analyzed and averaged in the analyzer in a continu mode, a Hanning squared (or cosine to the fourth power) window is app to the data being processed. This window is utilized for all functio computed by the FFT analyzer. The output of the analyzer, read off t cursor, was $S_e(f)$, i.e. the half-line power spectrum of the voltage signal in frequency domain.

5.2 Interpretation of Wave Number Spectra From Measured Frequency Spectra

To convert frequency spectra into wave number spectra, Taylor's hypoth (frozen turbulence hypothesis) was used and a constant convection velocity all turbulence scales was assumed; i.e., if k_1 is the wave number then

$$k_1 = \frac{2\pi f}{U_c} \qquad (5.2)$$

The applicability of this hypothesis to the jet mixing layer has been discussed in detail by George et al. (12). In accordance with their choice, the convection velocity has been selected as the velocity in the center of the mixing layer. Thus,

$$U_c = 0.6\, U_e \tag{5.3}$$

The velocity spectrum in the frequency domain can be directly related t the measured spectrum $S_e(f)$ by

$$S_u(f) = \bar{K}^2\, S_e(f) \tag{5.4}$$

where $\bar{K}$ is the linearization constant U/E. Equation (5.4) follows immediate from

$$\overline{u_1^2} = \int_0^\infty S_u(f)\, df = \bar{K}^2 \int_0^\infty S_e(f)\, df \tag{5.5}$$

and the point-by-point correspondence of the integrands.

The applicability of Taylor's hypothesis to obtain the wave number spectrum from the frequency spectrum is accomplished as follows:

$$S_u(f) \longrightarrow F_{11}^1(K_1)$$

where

$$f \longrightarrow k_1 = \frac{2\pi f}{U_c}$$

$F_{11}^1(k_1)$ is the one dimensional spectrum of the x component of velocity and is given by

$$F_{11}^1(k_1) = \iint_{-\infty}^{\infty} F_{11}(\underline{k})\, dk_2\, dk_3 \tag{5.6}$$

where

$$F_{11}(\underline{k}) = \frac{1}{(2\pi)^3} \iiint_{-\infty}^{\infty} \overline{u_1(\underline{x})\, u_1(\underline{x} + \underline{r})}\, e^{-i\underline{k}\cdot\underline{r}} d\underline{r} \tag{5.7}$$

An alternative and equivalent definition is

$$F_{11}^{1}(k_1) = \frac{1}{2\pi} \int_{-\infty}^{\infty} \overline{u_1(x,y,z)\, u_1(x+r,y,z)}\, e^{-ik.r} dr \qquad (5.8)$$

where $\overline{u_1(x,y,z)\, u_1(x+r,y,z)}$ is recognized as the axial correlation of the x-component of velocity. Note that $F_{11}^{1}(k_1)$ is defined over the whole line $(-\infty,\infty)$ and that $F_{11}^{1}(k_1) = F_{11}^{1}(-k_1)$.

Since the velocity spectrum must integrate to the mean square velocity. it follows that

$$u_1^2 = \int_{-\infty}^{\infty} F_{11}^{1}(k_1)\, dk = \int_{0}^{\infty} S_u(f)\, df \qquad (5.9)$$

Application of the above relations implies

$$\frac{2\pi}{U_c} \int_{-\infty}^{\infty} F_{11}^{1}\left(\frac{2\pi f}{U_c}\right) df = \int_{0}^{\infty} S_u(f)\, df$$

from which the symmetry of $F_{11}^{1}(k_1)$ and a point-by-point identification of integrands implies

$$F_{11}^{1}(k_1) = \frac{U_c}{2\pi} \left[\frac{1}{2} S_u(f)\right] \qquad (5.10)$$

the factor of $\frac{1}{2}$ accomplishes the conversion of the measured half-line spectrum to a whole-line spectrum.

5.3 The Results

Data were taken for the one dimensional power spectra at x/D of 1, 2, 3, 4 and 5 in the center of the mixing layer. The normalized spectra are shown in Figure 5.3. The low frequency break point is at $k_1 x = 10$, the roll off is -5/3 in the inertial sub-range and the spectra finally roll off again due to attenuation by the sensor placed in the flow and the low pass filteri of the input signal. The measured spectra were graphically integrated to

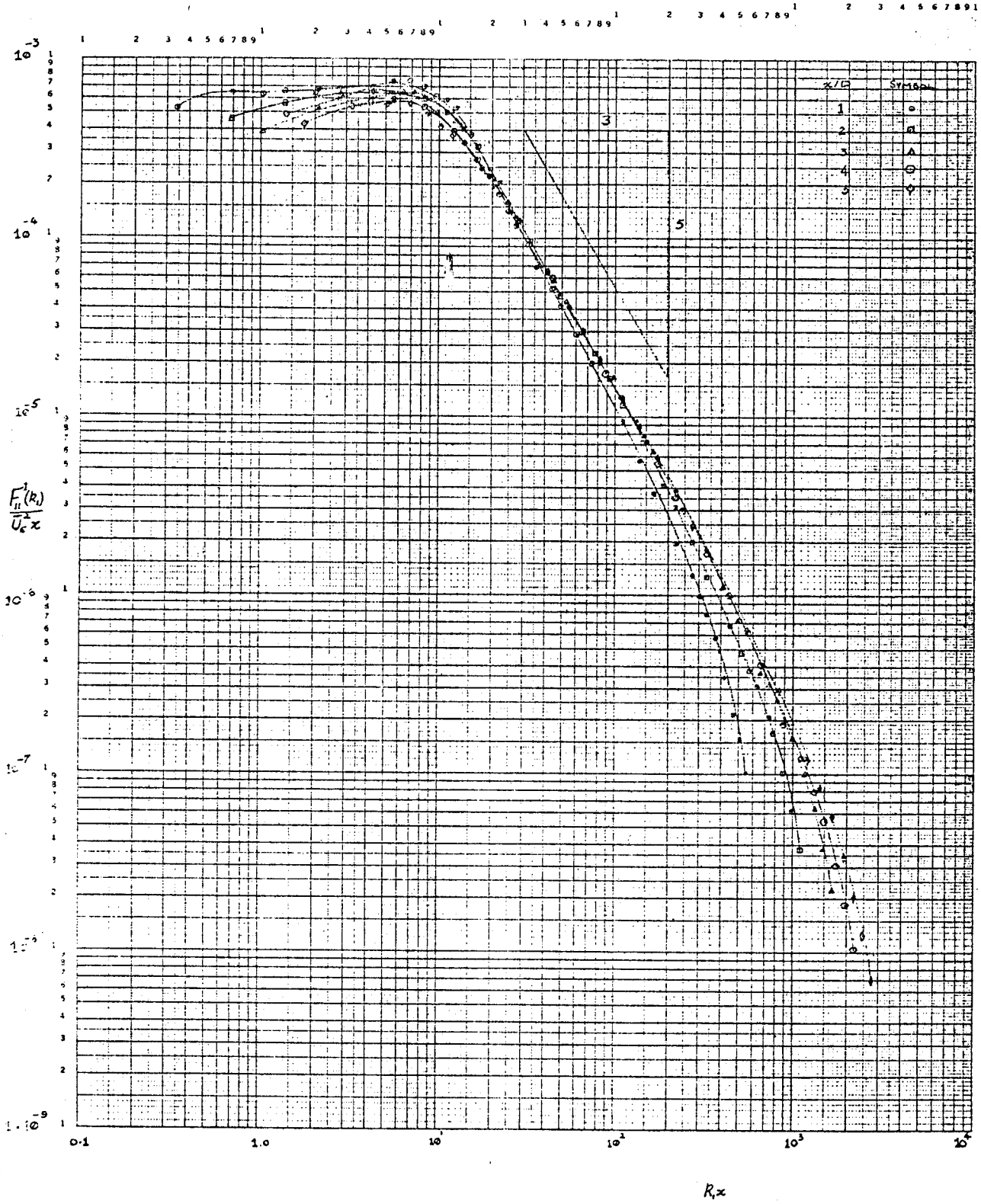

FIG 5.3

compare with the mean square value of the turbulence signal measured on dig voltmeters.

$$\overline{e^2} = 2 \int_0^\infty S_e(f)\, df$$

The integrated spectra matched the measured mean square values of the signa turbulence signals to between 95% and 97%, the integrated values being the ones consistently. This agreement confirms the spectral calibration proced which were used.

Spectra measured at x/D of 2 and 5 were differentiated in the frequency domain and the results are shown in Figure 5.4 and 5.5. The differentia spectra show a + $k^{1/3}$ range which corresponds to the inertial subrange.

The dissipation of turbulent energy ε can be estimated from the measure spectra in the inertial subrange. A value of approximately 1 KHz was used all x/D. The estimates were obtained as follows: From Batchelor (1953), t spectrum in the inertial subrange is given by

$$F_{11}^1(k_1) = \frac{9}{55} \alpha\, \varepsilon^{2/3}\, k_1^{-5/3} \qquad (5.11)$$

which implies

$$\varepsilon = \left[\frac{55}{9\alpha} k_1^{5/3}\, F_{11}^1(k_1)\right]^{3/2}$$

Normalizing by x and U_e yields

$$\frac{\varepsilon x}{\overline{U}_e^3} = \left[\frac{55}{9\alpha} k_1^{5/3} F_{11}^1(k_1)\right]^{3/2} \frac{x}{\overline{U}_e^3} \qquad (5.12)$$

α is generally believed to be about 1.5 (Tennekes & Lumley).

The results computed from Figure 5.3 are summarized in the table below:

Table 5.1

x/D	1	2	3	4	5
$\frac{\varepsilon x}{U_e^3}$	0.046	0.047	0.0465	0.0475	0.048

The collapsed data for $x/D = 2$, 3, and 4 are shown in Figure 5.6 and are compared with the one-dimensional spectral estimate from the local isotropy hypothesis (see George et al. 1980).

$$F_{11}^1(k_1) = \frac{9}{55}\alpha\,\varepsilon^{2/3}\lambda^{5/3}\frac{1}{[1+(k_1\lambda)^2]^{5/6}} \tag{5.13}$$

where

$$\alpha = 1.5,\ \varepsilon = 0.046\frac{\overline{U}_e^2}{x},\ \lambda = 0.96\ell = (0.96)(0.086)x$$

hence

$$\frac{F_{11}^1(k_1)}{\overline{U}_e^2 x} = \frac{4.93\times10^{-4}}{[1+6.82\times10^{-3}(k_1x)^2]^{5/6}} \tag{5.14}$$

It is evident from the superimposed plot of Figure 5.6 that the semi-empirical estimate for $F_{11}^1(k_1)$ coincides with the measured spectra only in the -5/3 range. This is, of course, as expected since the estimate above assumes an equi-partition of turbulent energy among all three components of fluctuating velocity. The slight off-axis peak in the measurements ($\sim k_1x \approx 10$) is consistent both with the fact that $\overline{j_1^2} > \overline{u_2^2}$ or $\overline{u_3^2}$ (c.f. George et al. 1980) and the fact that the Reynolds stress produces only the $\overline{u_1^2}$ component directly from the mean shear.

Spanwise power spectra were measured at x/D of 3, from the centerline of the jet out along the r-axis to the point at which $\overline{U} = 0.1\ \overline{U}_e$. These are shown in Figure 5.7. At the lowest frequency measured (10 Hz) there

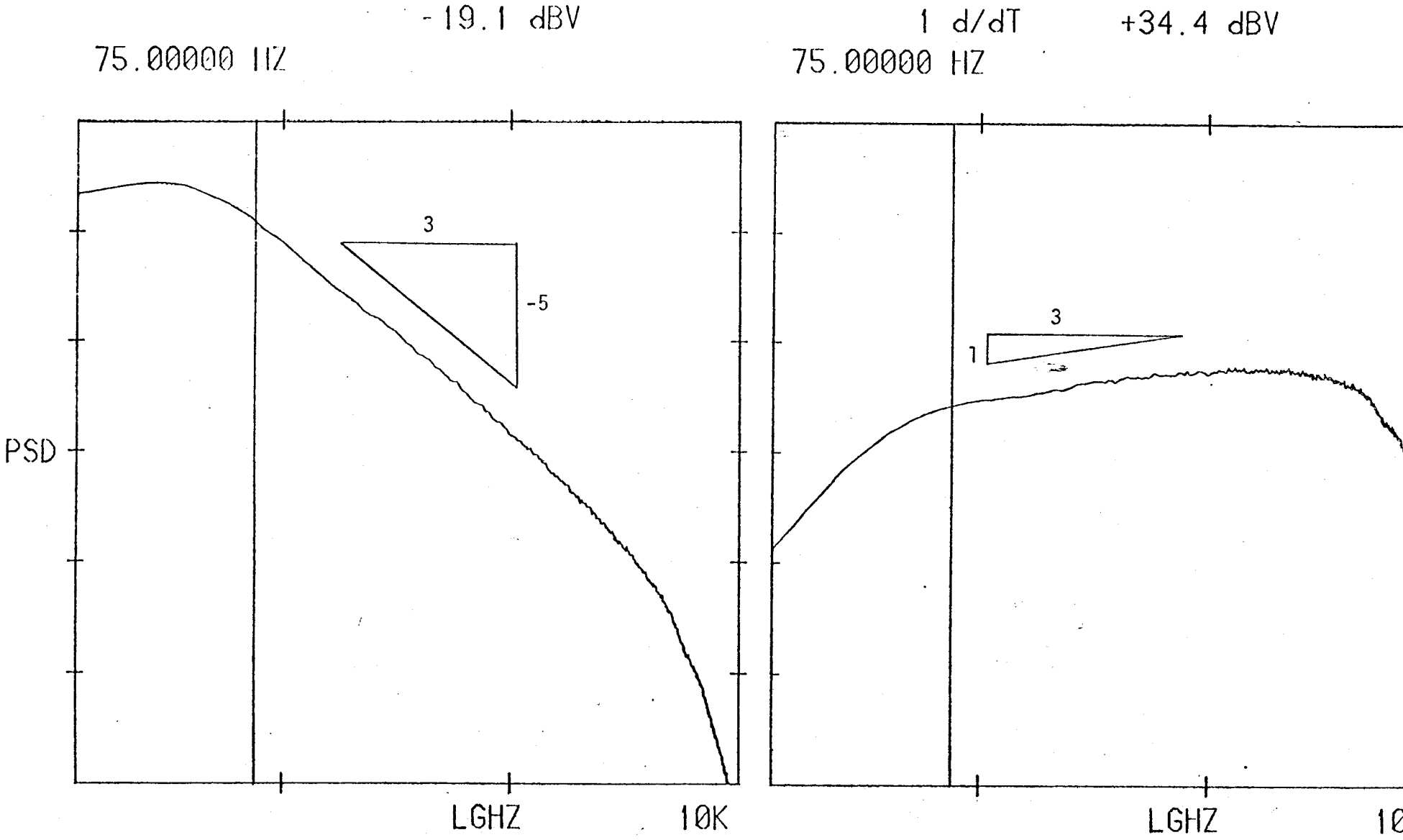

FIG. 7 - CENTER OF MIXING LAYER POWER SPECTRUM AND DIFFERENTIATED SPECTRUM

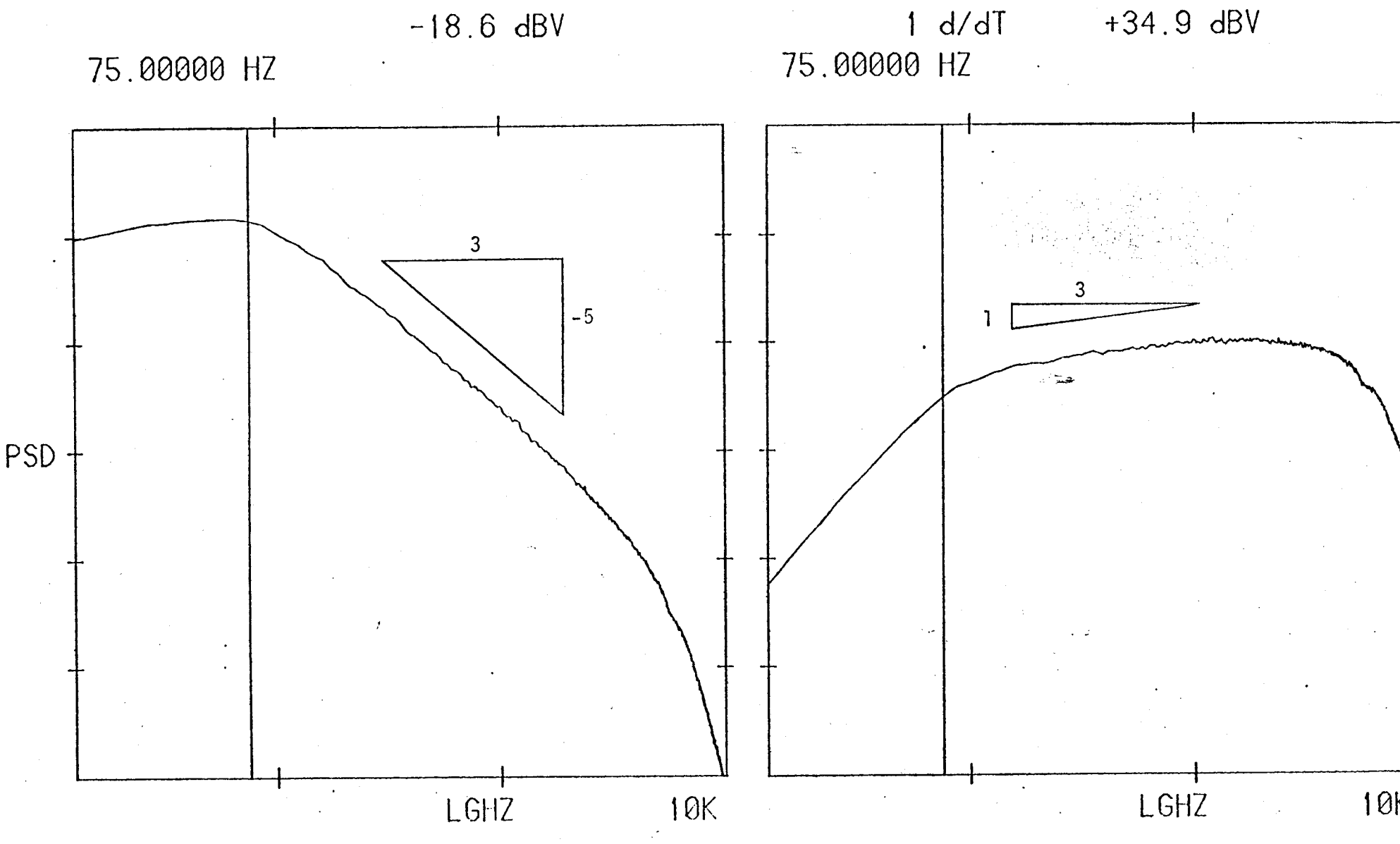

FIG. 5.4 CENTER OF MIXING LAYER POWER SPECTRUM AND DIFFERENTIATED SPECTRUM.

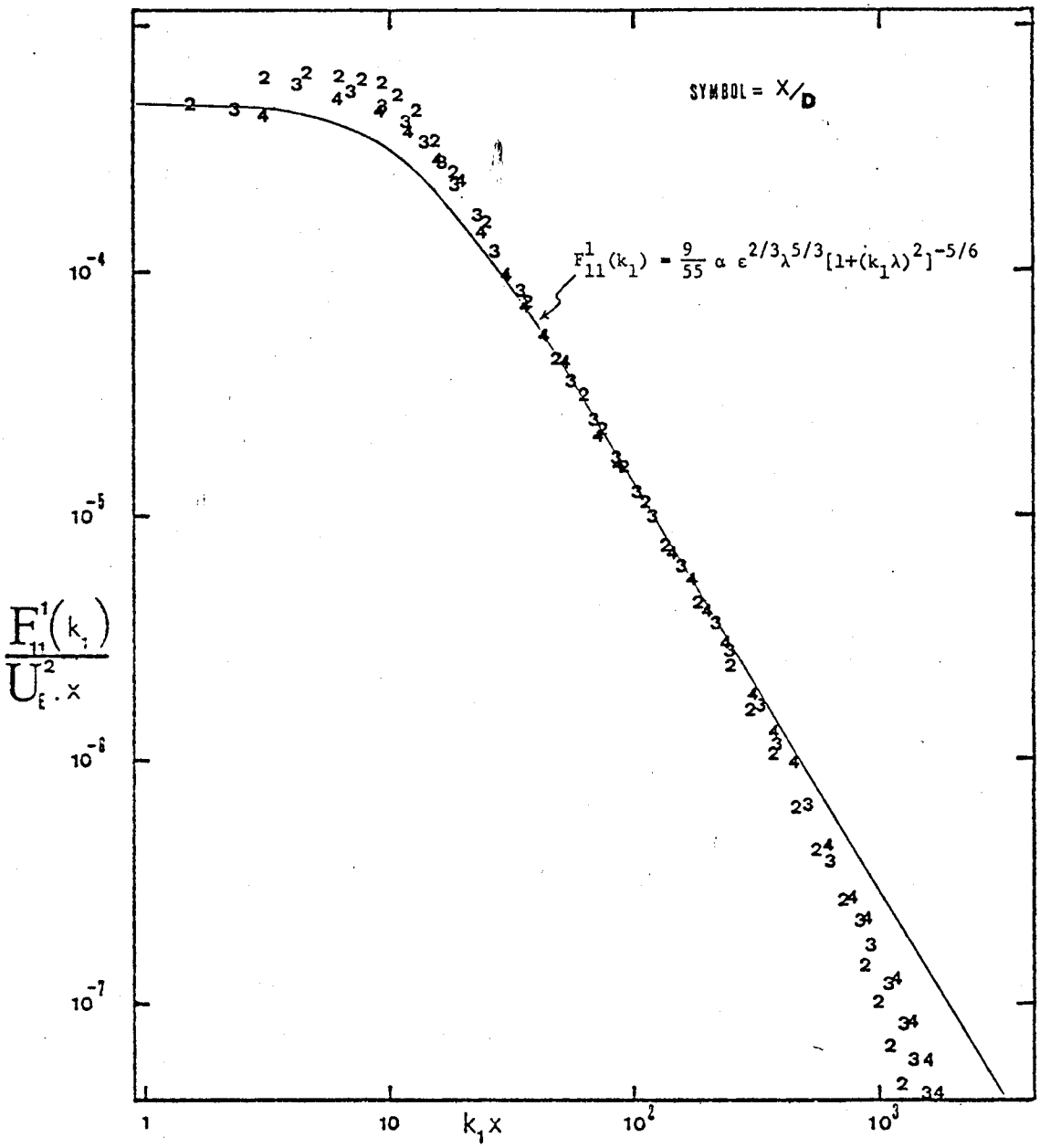
SYMBOL = X/D
$F_{11}^1(k_1) = \frac{9}{55} \alpha \varepsilon^{2/3} \lambda^{5/3} [1+(k_1\lambda)^2]^{-5/6}$
$\frac{F_{11}^1(k_1)}{U_\xi^2 . x}$
10^{-4}
10^{-5}
10^{-6}
10^{-7}
1
10
$k_1 x$
10^2
10^3

FIG 5.6

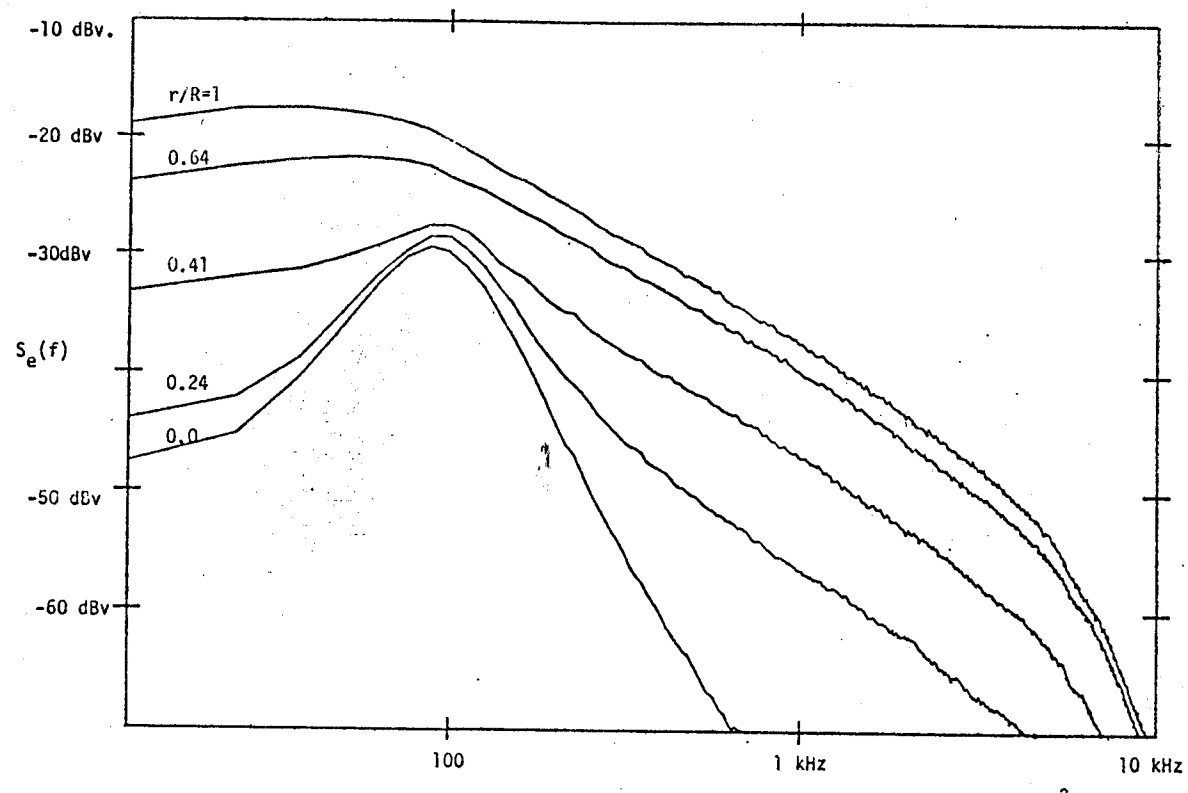

FIG. 7a SPANWISE POWER SPECTRA. x/D=3. (Linearised, Halfline). $S_e(f)$=dBv= 10 $Log_{10}(\frac{V^2}{Hz})$.

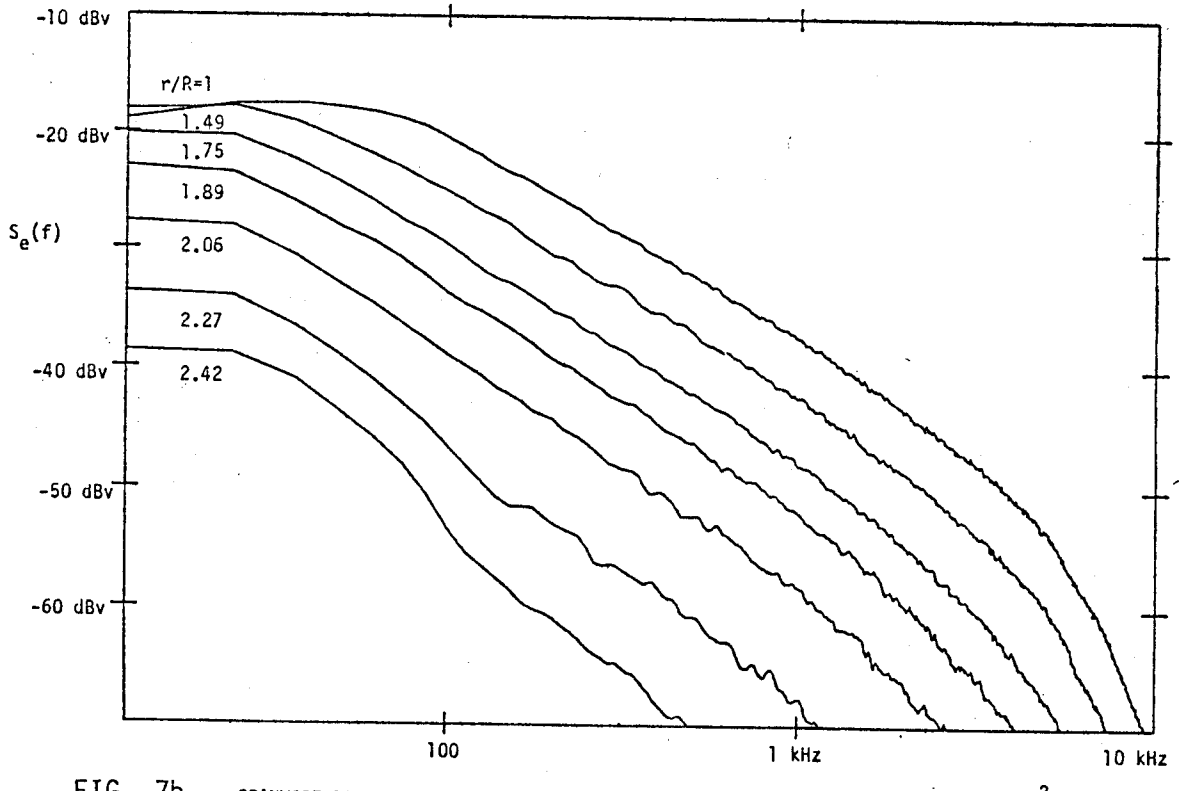

FIG. 7b SPANWISE POWER SPECTRA. x/D=3. (Linearised, Halfline). $S_e(f)$=dBv= 10 $Log_{10}(\frac{V^2}{Hz})$.

is a difference of 3 decades between the spectra at the centerline and in the center of the mixing layer. At the frequency corresponding to the breakpoint in the spectrum for the center of the mixing layer (~ 100 Hz), the difference with the centerline spectra is only one decade. The turbulence intensity at the centerline at x/D = 3 was $u'/\bar{U}_e = 0.03$, almost 10 times that at the exit plane. From the spectra it is clear that this energy is concentrated near the single frequency (wave number) corresponding to the break-point in the spectra measured in the shear layer, that is, the frequency which characterizes the turbulent energy.

The spanwise spectra on the outside of the shear layer are shown in Figure 5.7b. These, unlike those on the inside of the shear layer (Fig. 5.7a), have roughly the same shape as those at the center of the mixing layer but with a magnitude which diminishes with distance from the jet axis. This is consistent with the increasing intermittency with radius and the outward transport of turbulent energy. The shift to the left with increasing radius is primarily the result of the decreasing convection velocity as can be seen from equation (5.10) with the assumption that the shape of $F_{11}^1(k_1)$ is unchanged, while the reduced magnitude is a result of both the reduction in $\overline{u_1^2}$ by the intermittency and the reduced convection velocity.

The power spectrum measured at the exit plane is shown in Figure 5.8. The difference between this and the spectrum at r/R = 0 in Figure 5.7a shows the 4 decades rise in the spectral height at 100 Hz between x/D of 0.18 and x/D of 3. There is evidently a high level of disturbance present (once a small bandwidth) in the so-called potential core of the jet at the latter position. It seems clear from the frequencies that these fluctuations (which could be irrotational) are clearly linked to the energetics of the shear layer.

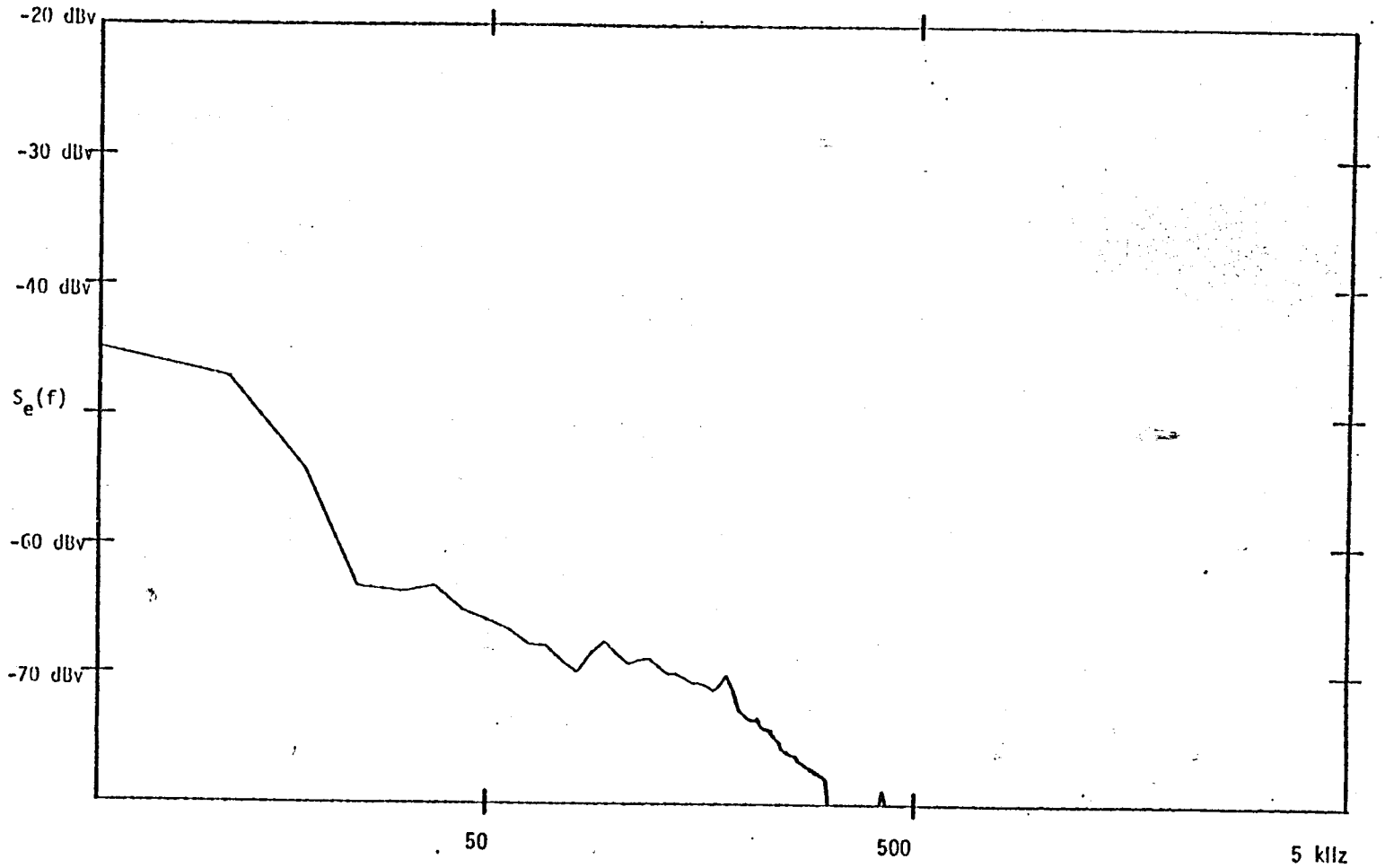

FIG. 5.8 EXIT PLANE POWER SPECTRUM(Center of jet). (Linearised, Halfline, 6.25 Hz B.W.).

$S_e(f)$=dBv= 10 $LOG_{10}(\frac{V^2}{Hz})$. x/D=0.18 . u'/U_e=0.332% . $Signal/_{Noise} > 100$.

CHAPTER 6

6. Correlation Measurements

6.1 Time Autocorrelations

(i) Measurement Techniques

The instrumentation used for measuring time autocorrelation was essentially the same as that discussed in Chapter 5 for spectral analys Linearized hot wire signals were low passed at 250 Hz and high passed a 0.5 Hz before being input to the FFT analyzer. The input trigger was set at half full scale to sample only after a high fluctuation level ha arrived. The analyzer computed the time autocorrelation in a continuou mode over record lengths of 0.08 sec, with the data sampled at 12.8 KHz The autocorrelations computed for each record were displayed continuous as 2048 point plots and averaging was performed over 1000 such records.

(ii) Analysis of Results

Measurements were taken in the center of the mixing layer at x/D of 2, 3 and 4. The results are shown in Figures 6.1, 6.2 and 6.3 . Quantitative computations derived from these plots are summarized in Table 6.1. The time integral scale (of the low passed signal) is computed by integrating the autocorrelation curve on the positive side only. Table 6.2 shows the spacial scales computed from the time scales by multiplying by the average convection velocity ($U_c = 0.6\ U_e$).

Table 6.1

x/D	$\mathcal{I}$ sec.	T_1 sec (1st Zero crossing)	T_2 sec (-ve peak)	T_3 sec (2nd Zero crossing)
2	0.00163	0.00465	0.00703	0.02273
3	0.0025	0.007	0.01047	0.02461
4	0.0032	0.0095	0.015	0.03945

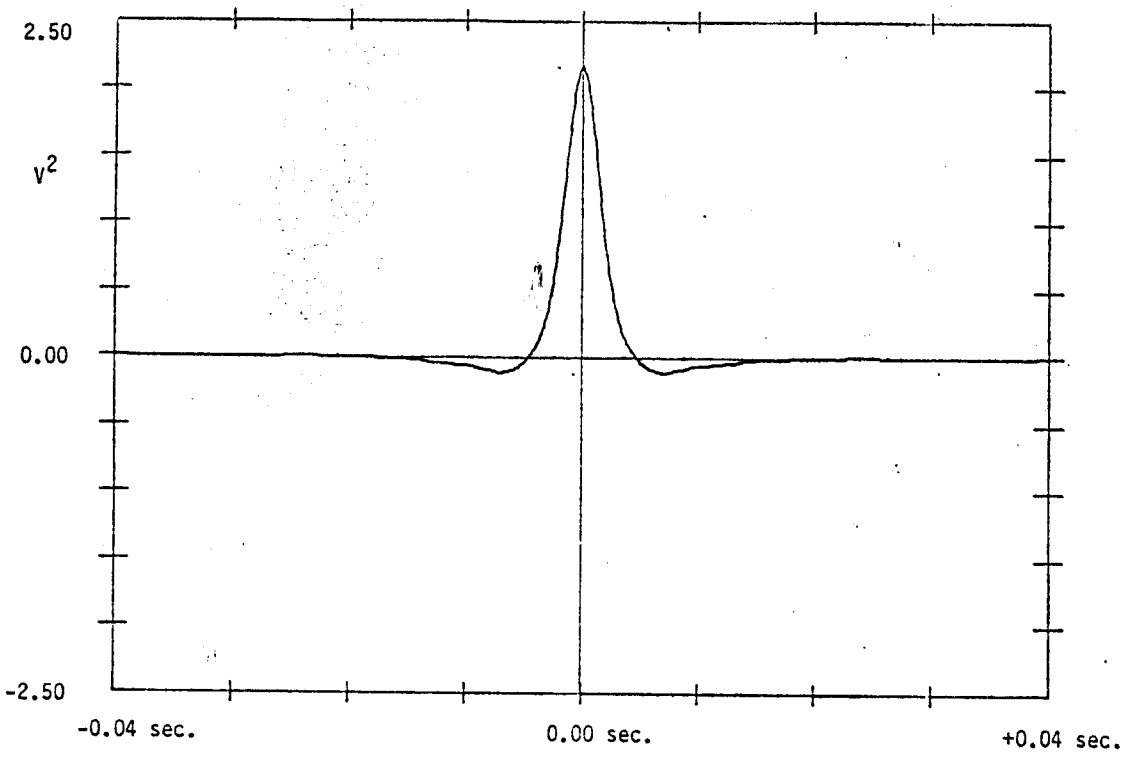

AUTO-CORRELATION FUNCTION . CENTER OF MIXING LAYER. X/D = 2.
LINEARISED SIGNAL, 250 Hz L.P., 1 Hz H.P., u/v =3.7 .

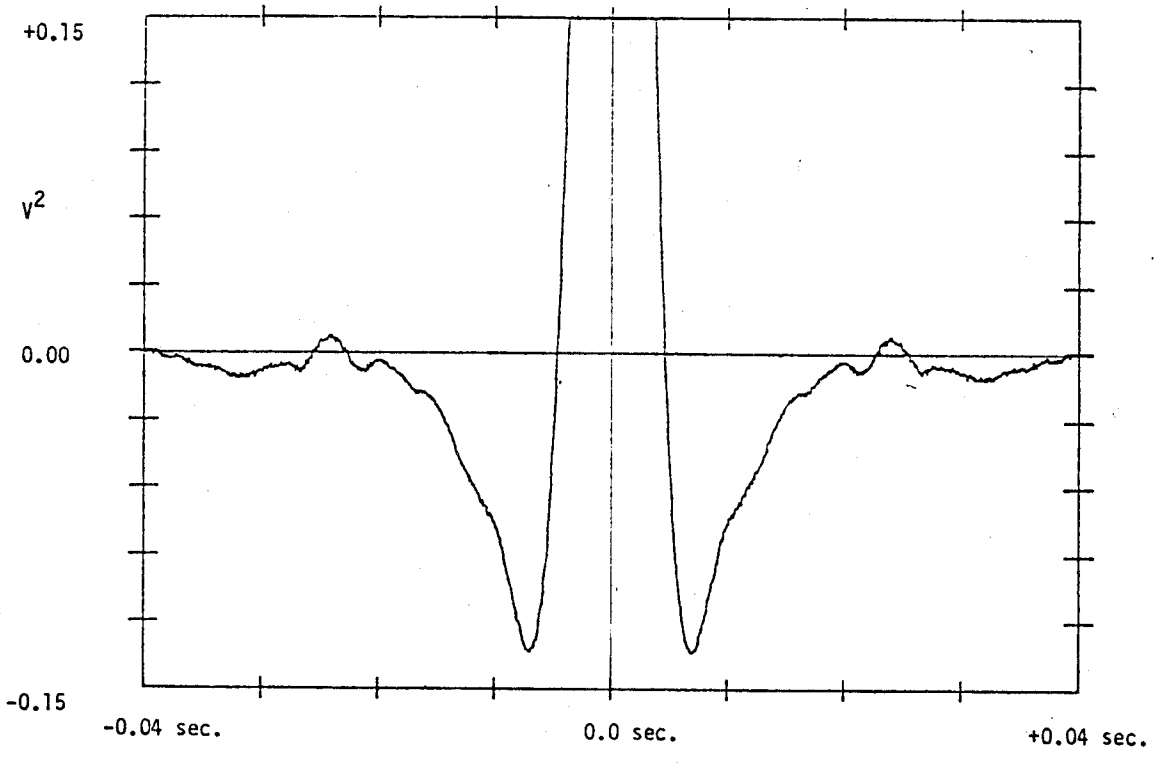

FIG. 6.1 ENLARGED VIEW OF ABOVE. CO-ORDINATES: (0.0 sec, 2.17 V^2), (0.00465 sec, 0.00 V^2), (0.00703 sec.,-0.111 V^2,-ve peak), (0.02273 sec, 0.00 V^2). U_e= 39.5 m/s .

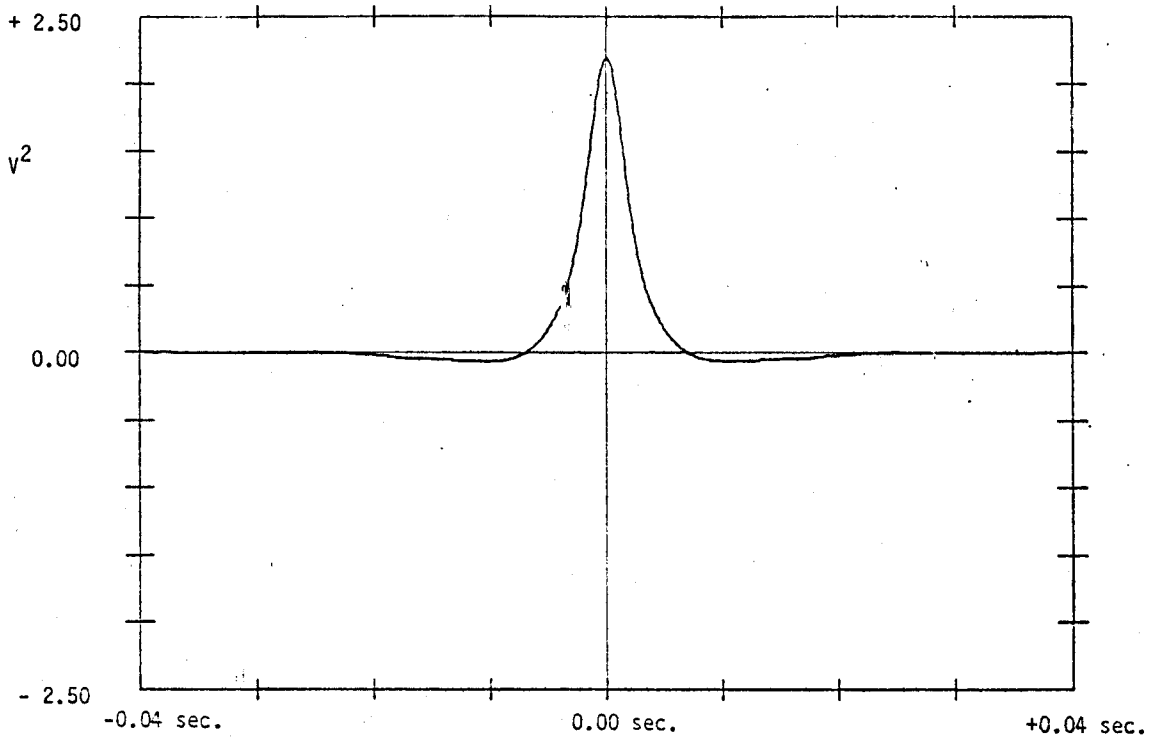

AUTO-CORRELATION FUNCTION. CENTER OF MIXING LAYER. X/D= 3 .
LINEARISED SIGNAL, u/v = 3.6 , 250 Hz. L.P., 1 Hz H.P.

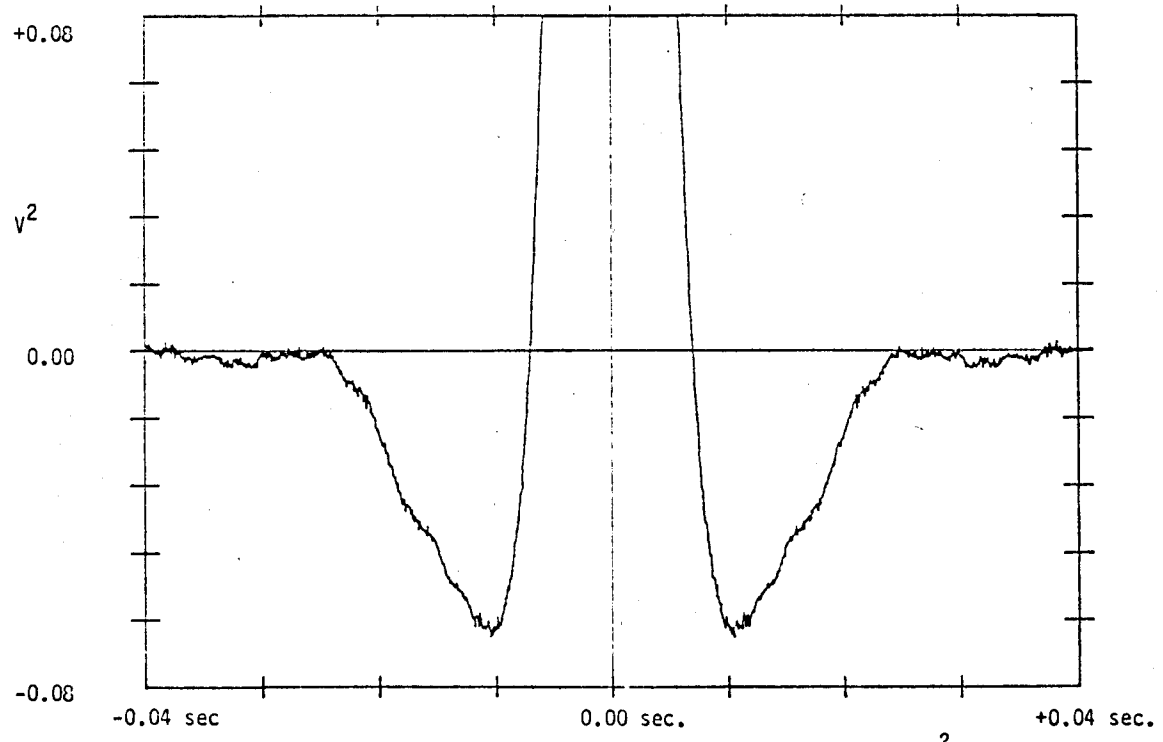

ENLARGED VIEW OF ABOVE. CO-ORDINATES: (0.00 sec.,2.20 V^2),
($\pm$0.007 sec.,0.00 V^2), ($\pm$0.01047 sec., -0.068 V^2, -ve peak),
($\pm$0.02461 sec., 0.00 V^2). U_e= 39.5 m/s .

FIG. 6.2

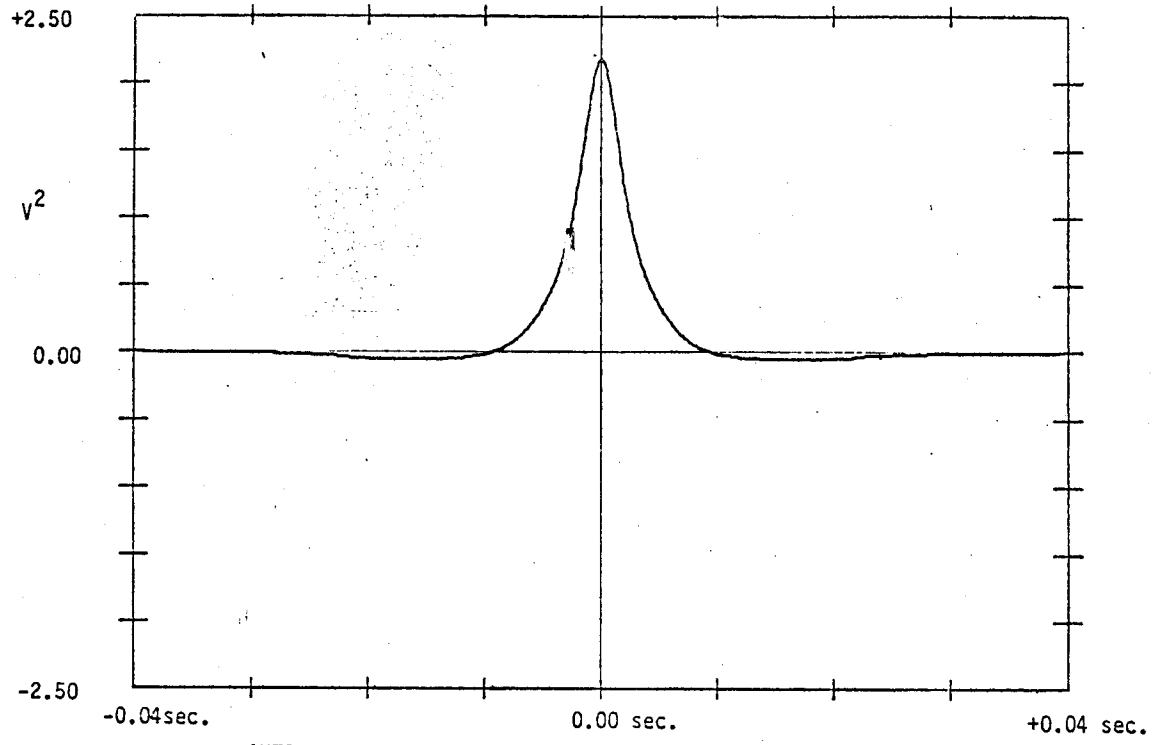

AUTO-CORRELATION FUNCTION. CENTER OF MIXING LAYER. X/D= 4 .
LINEARISED SIGNAL, u/v = 3.6 , 250 Hz. L.P., 1 Hz. H.P.

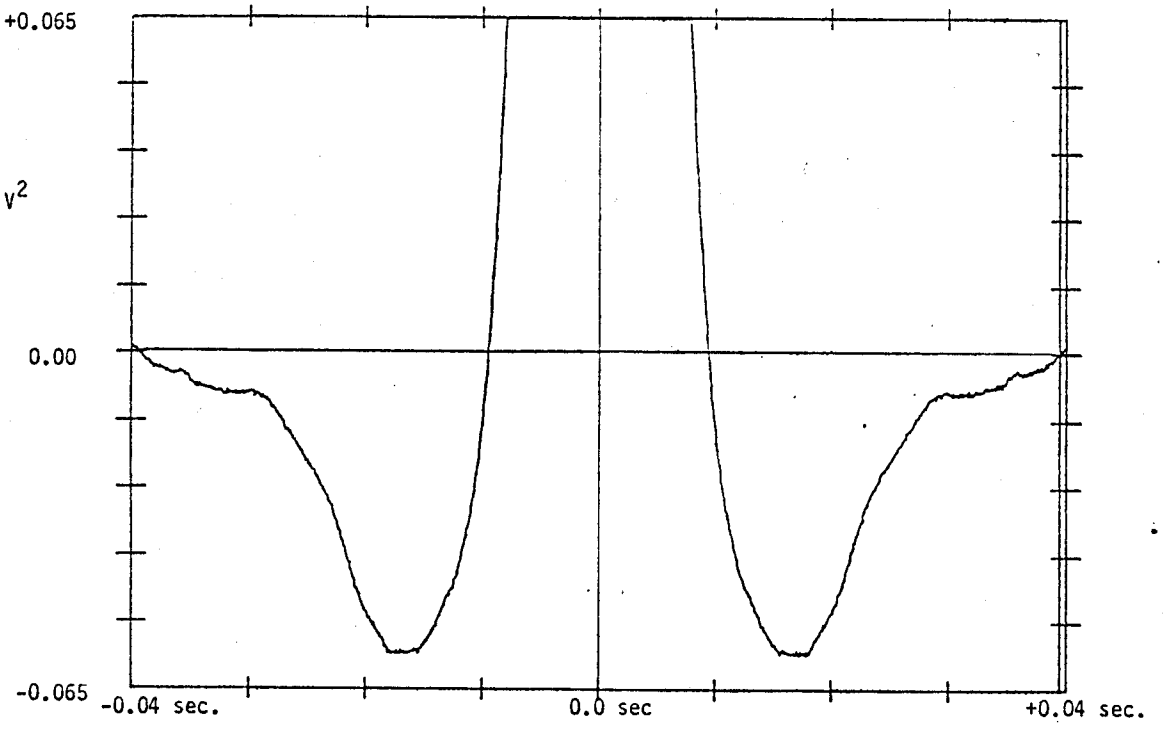

FIG. 6.3 ENLARGED VIEW OF ABOVE. CO-ORDINATES: (0.0 sec., 2.18 V^2), (±0.0095 sec., 0.00 V^2), (± 0.0167 sec., -0.054 V^2, -ve peaks), (±0.03945 sec., 0.00 V^2). U_e= 39.5 m/s .

Table 6.2

x/D	$\mathcal{L}$ cm	$\mathcal{L}$ /X	L_1^*/X	L_2/X	L_3/X
2	3.867	0.094	0.2678	0.405	1.309
3	5.925	0.096	0.2688	0.402	0.945
4	7.65	0.093	0.2736	0.432	1.136

*where $L = T.U_c$.

From George (1979) the variance of the autocorrelation at large lags can be estimated as follows:

$$e^2 = \frac{\text{var}\,[B(\tau)]}{[B(\tau)]^2} = \frac{2\mathcal{T}}{T}\left[\frac{1}{\rho(\tau)}\right]^2 \qquad (6.1)$$

where $B(\tau)$ = correlation function

$\mathcal{T}$ = time integral scale

T = averaging time (record length x no. of records)

$\rho(\tau)$ = autocorrelation coefficient at time lag of interest

For $\mathcal{T} \sim 0.0025$ sec, $\rho \sim 0.068$ and $T = 80$ sec at $x/D = 3$ we estimate e as $e \simeq 0.116$ (or 12% error at -ve peaks). At large time lags (2nd zero crossings) the error in the computed autocorrelation is greater than 20%. Thus, considering the degree of accuracy that can be expected from the signal and data processing parameters, the quantitative results of Table 6.2 show that the autocorrelation functions measured at the three locations scale with x. This conclusion is consistent with that of Chapter 5 where the power spectra were also shown to scale with x.

In chapter 5 it was shown that:

$$\frac{\varepsilon x}{U_e^3} \simeq \text{constant}$$

From Tennekes and Lumley (25), $\varepsilon \equiv u^3/\ell$. Along the center of the mixing layer u/U_e = constant; thus the observation that $\ell \sim x$ is consistent with the earlier conclusions. From Table 6.2 $\mathcal{L} \approx 0.095x$. All previous results from other investigators for the integral scale lie in the range $\mathcal{L} \approx 0.08 - 0.1x$, c.f. refs. (8), (17), (26).

An interesting feature of the autocorrelation measurements is the strong negative peaks at large time lags. Multiplied by an average convection velocity of 0.6 U_e these time lags correspond to wave-length in the range

$$\lambda = 2\ U_c\tau \approx 0.3 - 0.7\ m \qquad (6.2)$$

These large lags indicate that energy is present in the mixing layer at scales more than 10 times the size of the local integral scales. This observation will be confirmed by in the spacial cross-correlation measurements of the next section.

6.2 Cross Correlations (Spacial)

(i) Measurement Techniques:

Cross-correlations were measured in the axisymmetric mixing layer with the instrumentation schematic of Figure 6.4. One probe was placed in the center of the mixing layer, $\overline{U} = 0.59\ \overline{U}_e$ at three different positions: x/D of 2, 3 and 4. The second probe was traversed along a $\overline{U} = 0.4\ \overline{U}_e$ isocontour in one case and along a $\overline{U} = 0.8\ \overline{U}_e$ isocontour in the other case. See section 4.4 for intrinsic coordinate system. Both probes were always in the same diametrical plane, i.e. with the same z-ordinate in the (x, y, z) coordinate system.

The ordinate x for the fixed probe was measured perpendicular to the exit plane, while the ordinate x' for the moving probe was measured as x/cos θ where x was the perpendicular distance from the exit plane

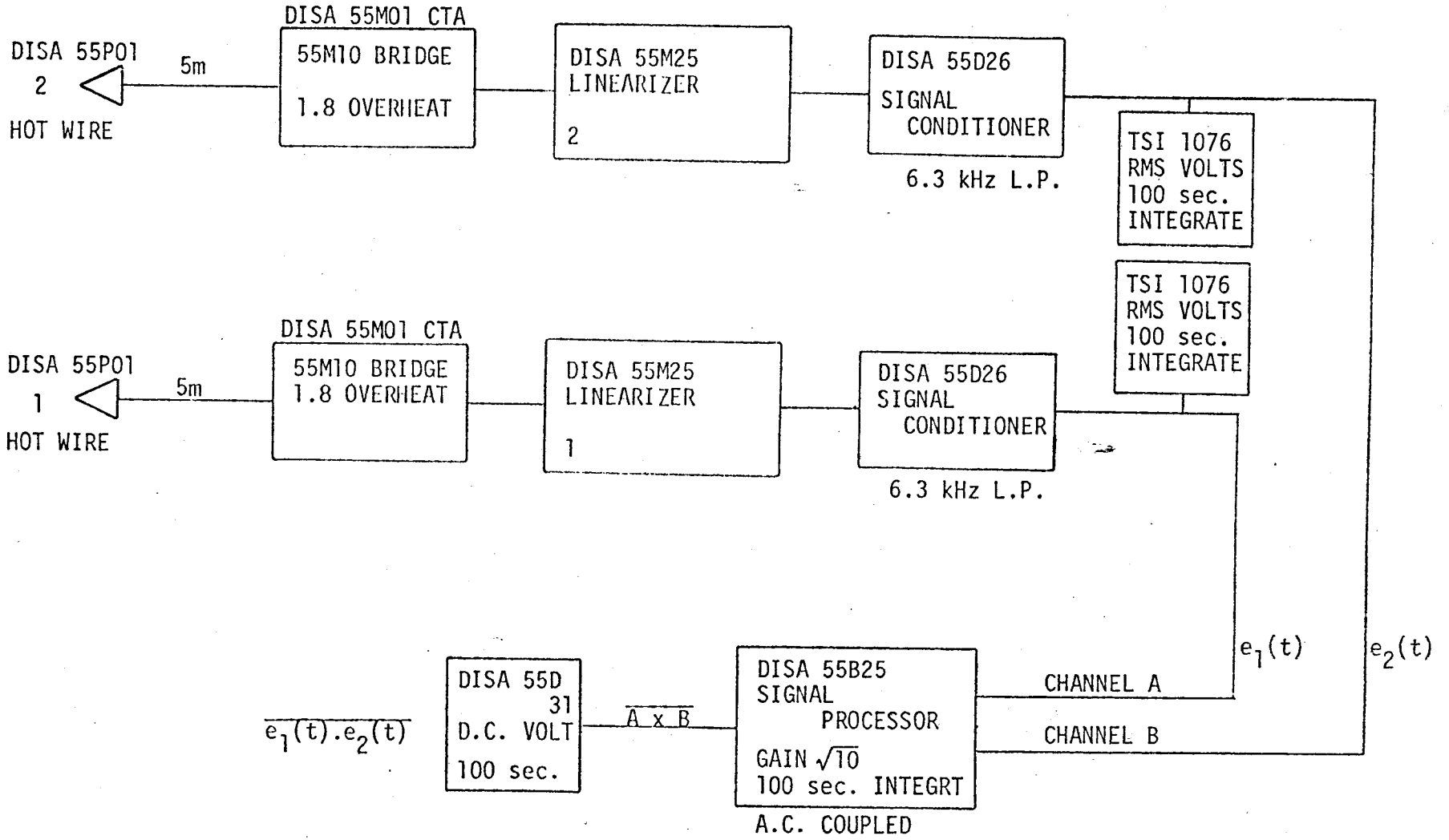

FIG 6.4 INSTRUMENTATION SCHEMATIC FOR CROSS-CORRELATION MEASUREMENTS.

and θ was the angle between the 0.4 $\overline{U}_e$ (or 0.8 $\overline{U}_e$) isocontour and a perpendicular to the exit plane.

The traverse along the x' ordinate was done with randomly spaced intervals to avoid the possibility of a coincidence of phase with any periodicity in the cross correlations being measured.

As single wires were used for each probe there was a possibility that any correlation between the contaminating velocity vectors would be superimposed on the correlations between the x component velocity vectors. In an effort to minimize the effect of such contamination the sensors were always kept perpendicular to each other. Thus the effective velocity being measured by each hot wire was contaminated by cross stream components perpendicular to each other. Thus the contaminating velocity would be v' on one sensor and w' on the one perpendicular to it. This is easily seen from equation (3.2) which yields the effective cooling velocities for each probe as:

$$\overline{u}_{eff_1} = \overline{U}\left(1 + \frac{\overline{v'^2}}{\overline{U}^2} + 0\left(\frac{u'}{\overline{U}}\right)^3\right)$$

and

$$\overline{u}_{eff_2} = \overline{U}\left(1 + \frac{\overline{w'^2}}{2\overline{U}^2} + 0\left(\frac{w'}{\overline{U}}\right)^3\right)$$

In the range over which cross-correlation measurements were made, the effect of contamination is less than a few percent (as mentioned in Chapter 4); therefore any cross-correlation between v' and w' would have an insignificant effect on the cross-correlations between the x components of velocity.

Each point on the cross-correlation curves represents and integration time constant of ~150 sec, the combined effect of integrating for

100 sec on the output of the turbulence processor and 100 sec on the digital voltmeters. The output had to be integrated for 600 sec before a steady state error envelope of ± 2% was reached; in the value of $e(x)\ e(x')$. The r.m.s. values of the fluctuating velocities varie less than 5% when traversing along the x and x' coordinate system.

The cross-correlations were normalized with the r.m.s. values of each signal thus making the correlation coefficient vary between ± 1. This normalization also made the correlation coefficient independent of the calibration constants.

$$\rho = \frac{\overline{u(x)\ u(x')}}{\sqrt{\overline{u(x)^2}}\ \sqrt{\overline{u(x')^2}}} = \frac{\left(\frac{dU}{dE_1}\right)\overline{e(x)\ e(x')}\left(\frac{dU}{dE_2}\right)}{\left(\frac{dU}{dE_1}\right)\sqrt{\overline{e(x)^2}}\ \sqrt{\overline{e(x')^2}}\left(\frac{dU}{dE_2}\right)}$$

$$= \frac{\overline{e(x)\ e(x')}}{\sqrt{\overline{e(x)^2}}\ \sqrt{\overline{e(x')^2}}} \qquad (6.3)$$

The signals were low passed at 6.3 KHz (corresponding to the pr attenuation frequency) and high passed at 1 Hz (both 18 dB/oct). Bas on the convection velocity the spacial scales corresponding to these frequencies are:

$$\lambda_L \simeq \frac{2U_c}{f_{L.P.}} = 0.75 \text{ cm} \qquad (6.4a)$$

$$\lambda_H \simeq \frac{2U_c}{f_{H.P.}} = 23 \text{ m} \qquad (6.4b)$$

which is much wider than all the scales of interest.

(ii) Analysis of Results:

The results of the cross-correlation measurements are plotted ir

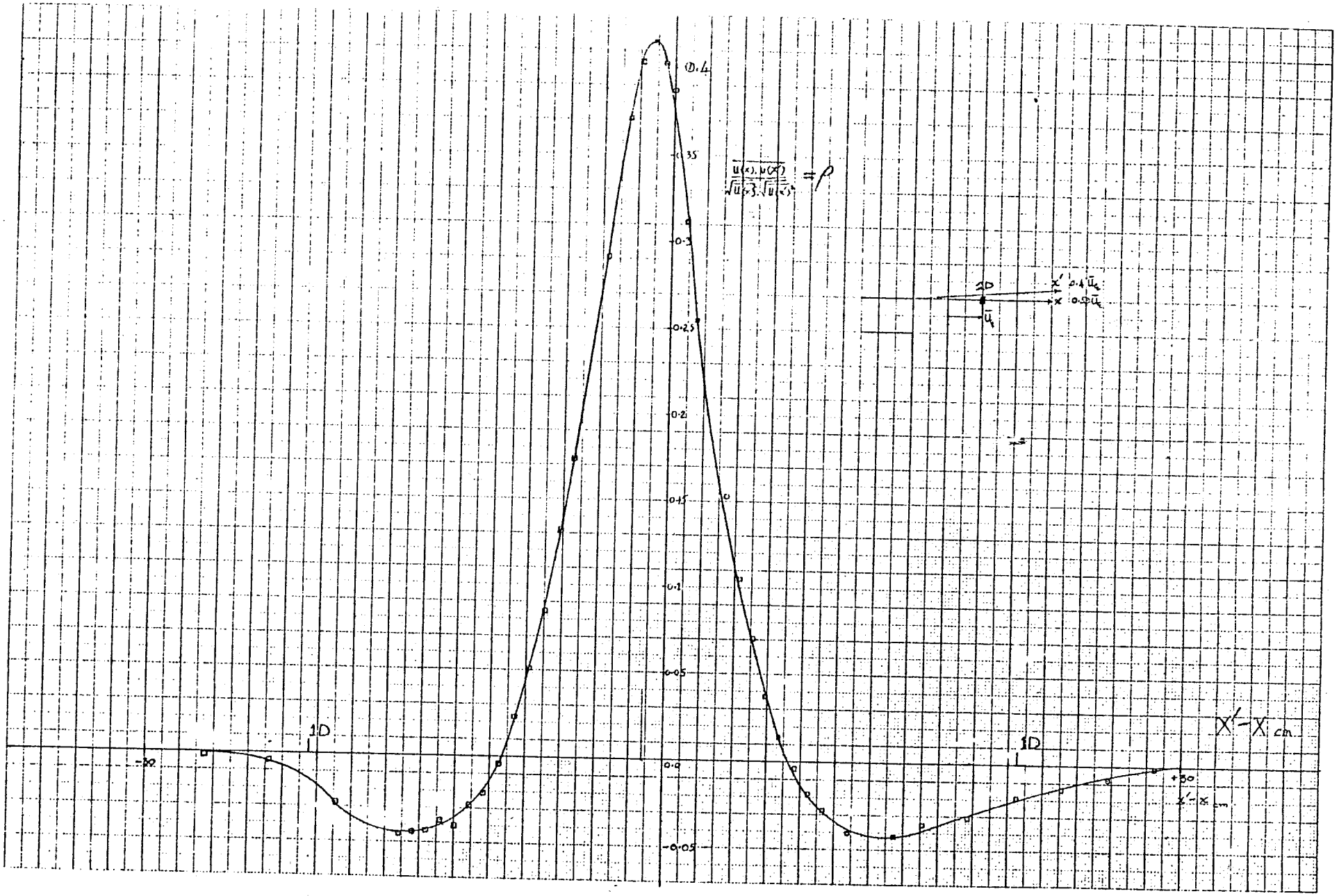

FIG 6.5

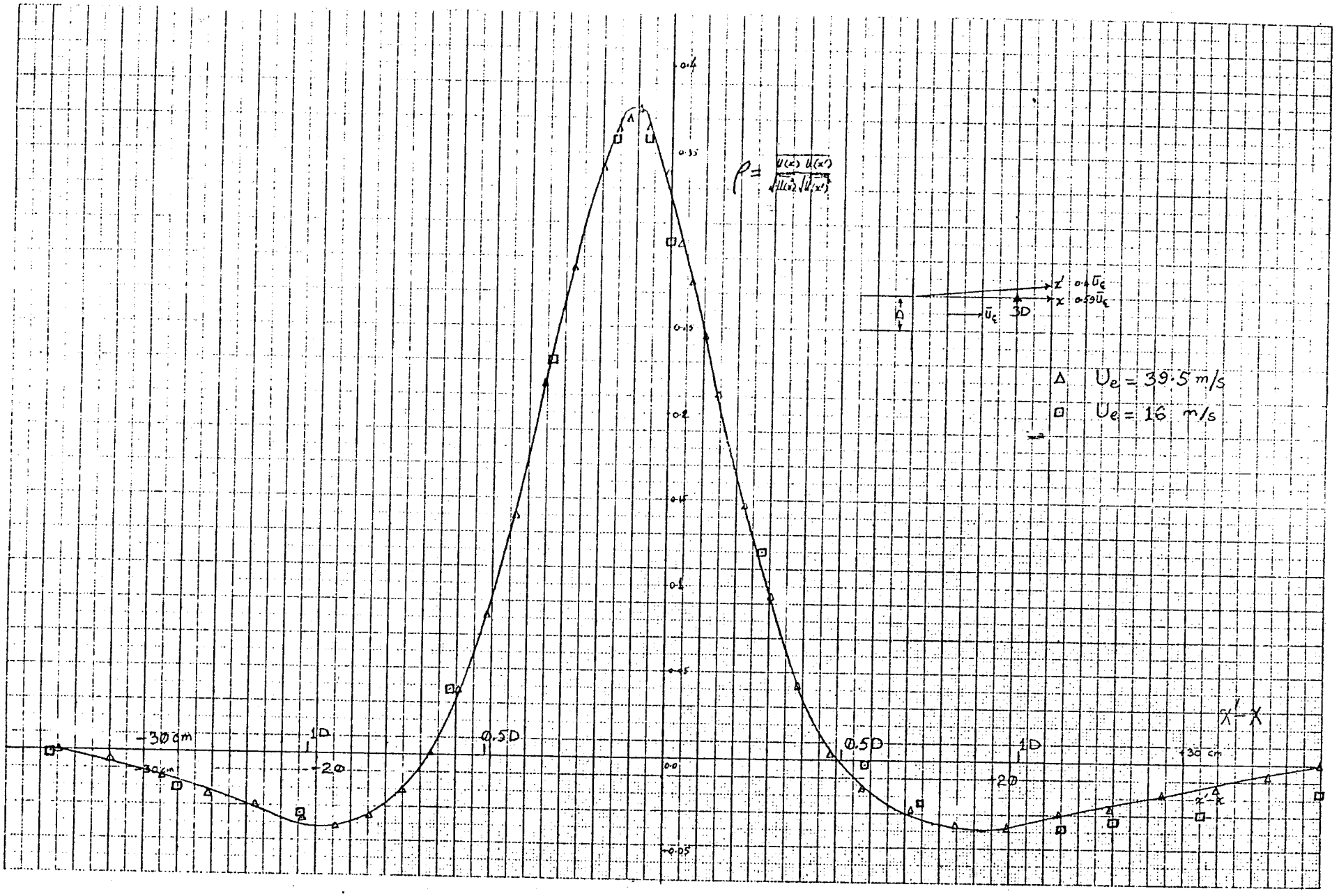
$\rho = \frac{\overline{u(x)\,u(x')}}{\sqrt{\overline{u(x)^2}}\sqrt{\overline{u(x')^2}}}$
x' 0.4 $\bar{u}_e$
x 0.59 $\bar{u}_e$
$\bar{u}_e$
3D
Δ U_e = 39.5 m/s
□ U_e = 16 m/s
0.4
0.35
0.3
0.2
0.1
0.0
-0.05
-30 cm
1D
0.5D
-2D
0.5D
1D
2D
30 cm
x'-x
x-x

FIG. 6.6

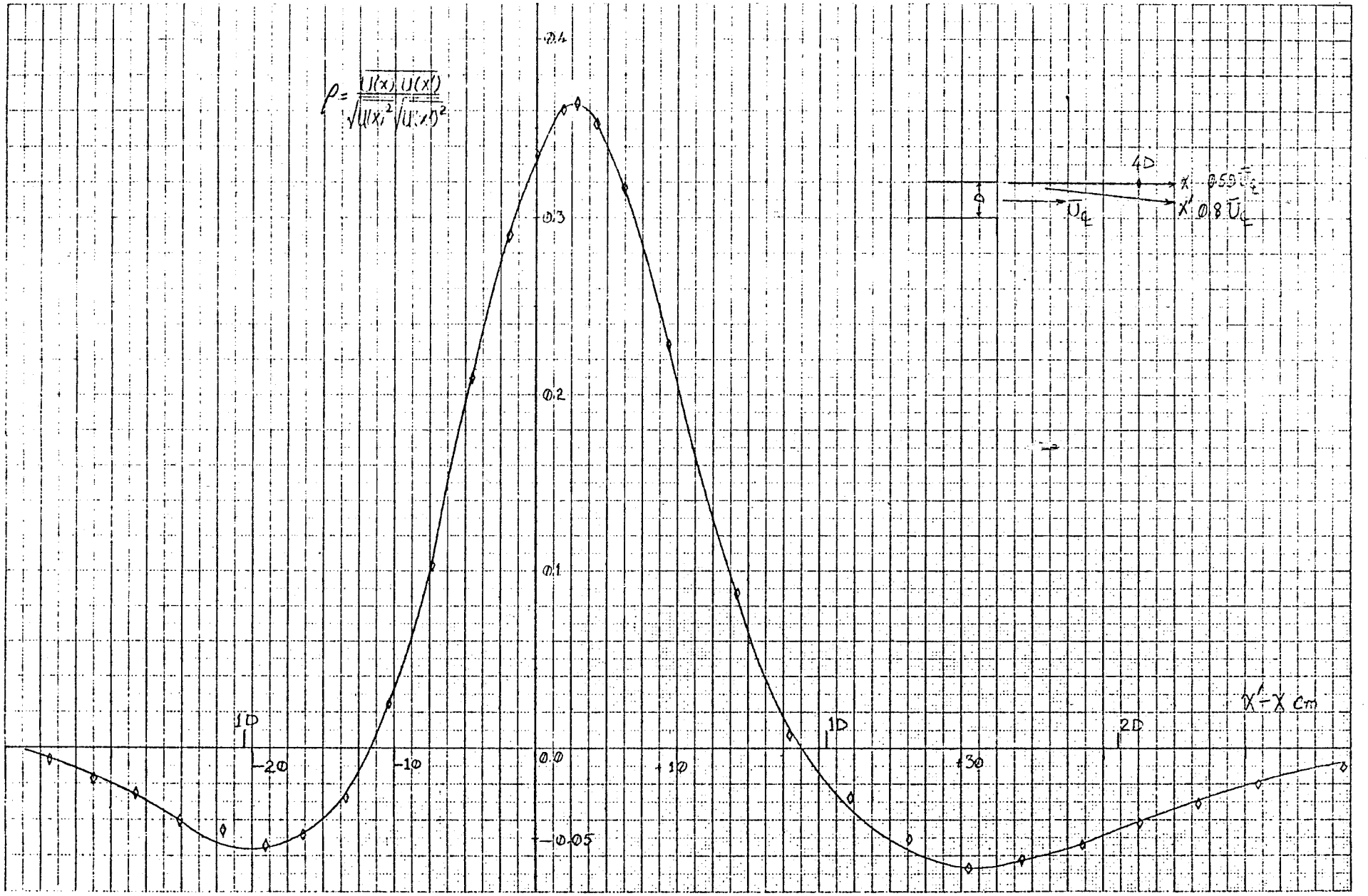
$\rho = \frac{\overline{U(x)\,U(x')}}{\sqrt{\overline{U(x)^2}\,\overline{U(x')^2}}}$
0.4
0.3
0.2
0.1
0.0
−0.05
4D
x 0.9 $\bar{U}_c$
x' 0.8 $\bar{U}_c$
$\bar{U}_c$
d
1D
−2D
−1D
0.0
+1D
1D
+3D
2D
$x'-x$ cm

FIG. 6.7

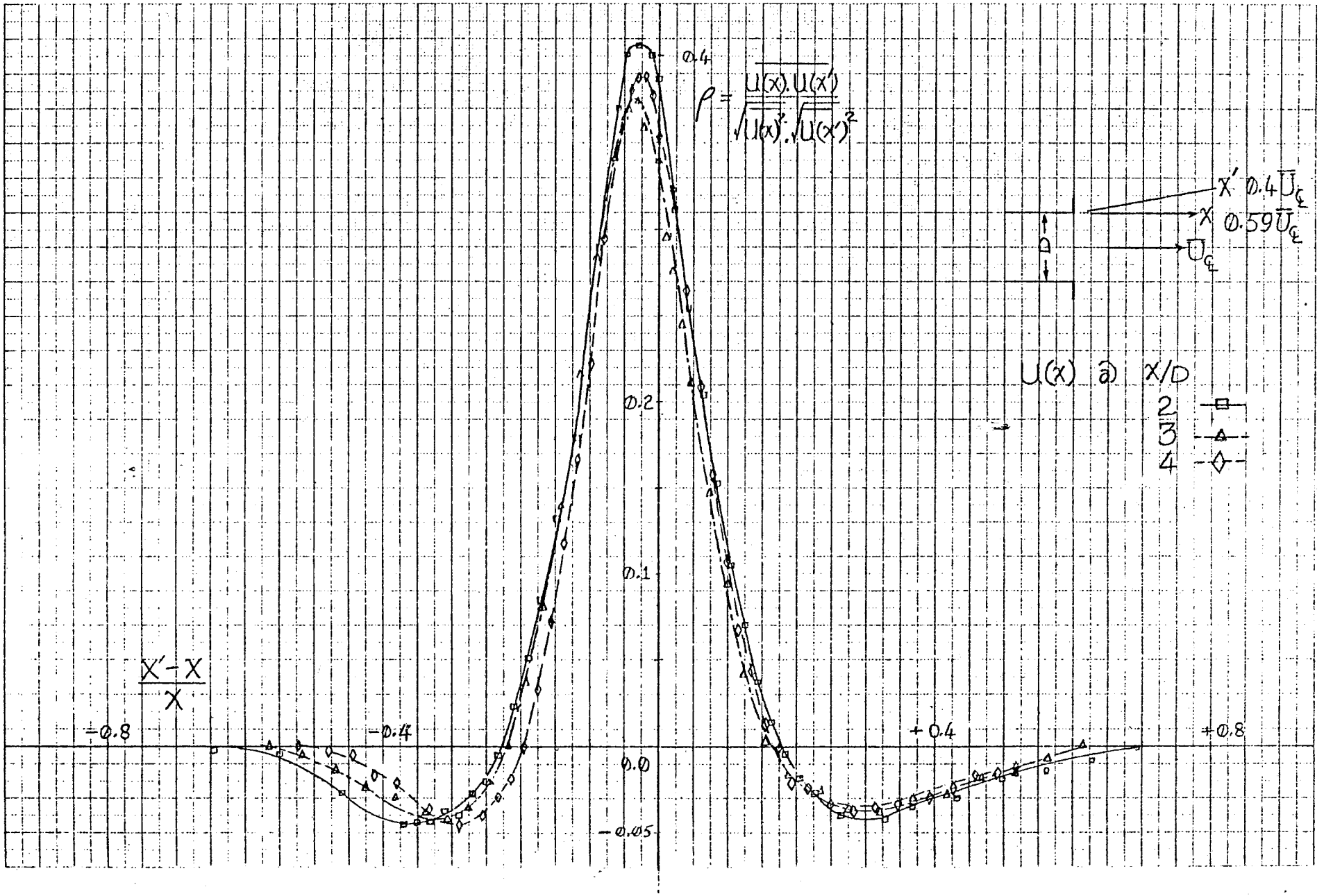
0.4
0.2
0.1
0.0
-0.05
$\rho = \frac{\overline{U(x).U(x')}}{\sqrt{\overline{U(x)^2}}.\sqrt{\overline{U(x')^2}}}$
x' 0.4 $\bar{U}_{\ell}$
x 0.59 $\bar{U}_{\ell}$
U_{ℓ}
D
U(x) a x/D
2
3
4
$\frac{X'-X}{X}$
-0.8
-0.4
+0.4
+0.8

FIG. 6.8

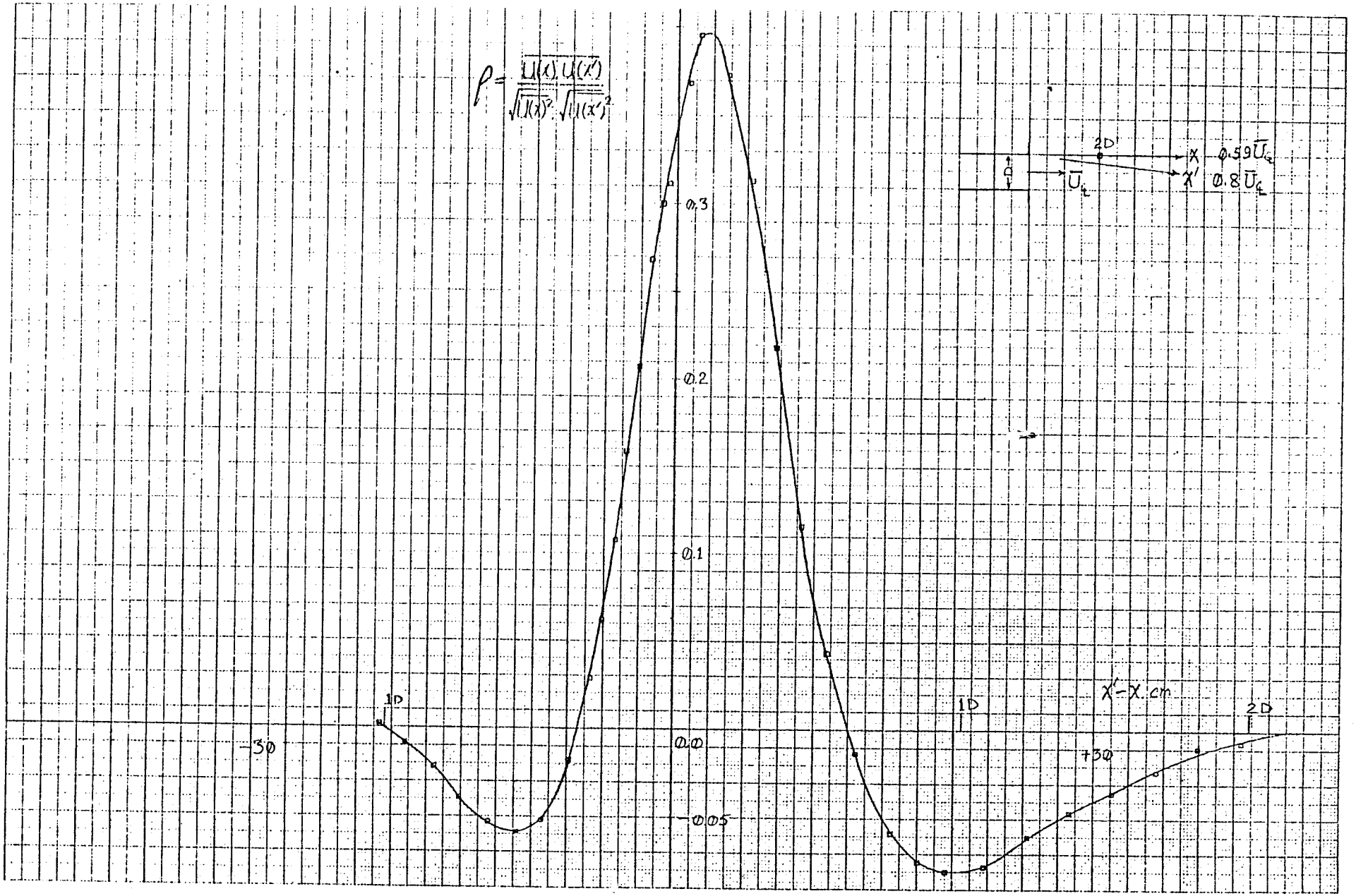
$\rho = \frac{\overline{U(x).U(x')}}{\sqrt{\overline{U(x)^2}}.\sqrt{\overline{U(x')^2}}}$
2D
X 0.99 $\bar{U}_c$
X' 0.8 $\bar{U}_c$
$\bar{U}_c$
0.3
0.2
0.1
0.0
-0.05
1D
-30
1D
X'-X, cm
2D
+30

FIG. 6.9

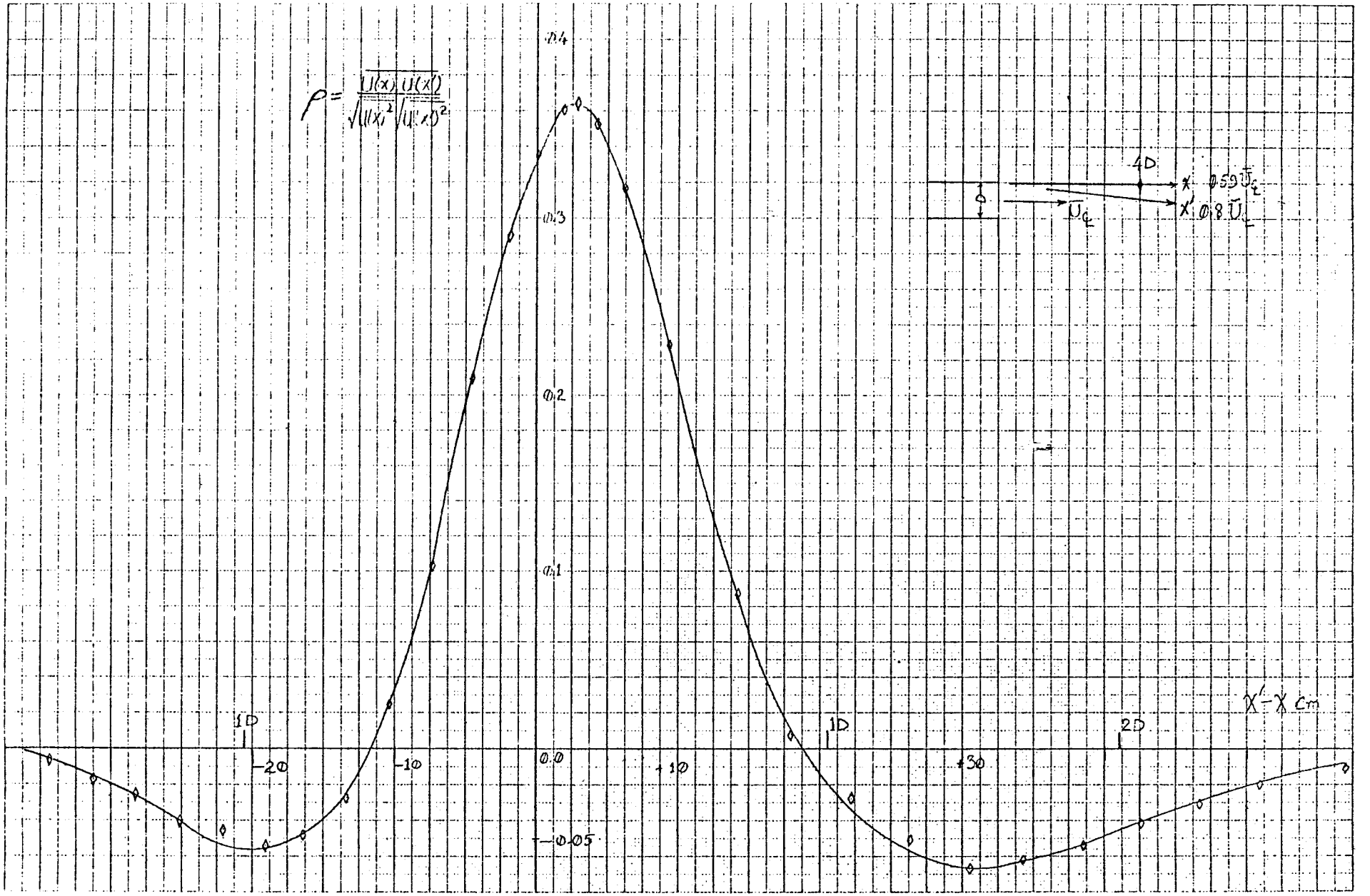
$\rho = \frac{\overline{U(x)\,U(x')}}{\sqrt{\overline{U(x)^2}}\sqrt{\overline{U(x')^2}}}$
0.4
0.3
0.2
0.1
0.0
−0.05
4D
$\bar{U}_\ell$
X 0.59 $\bar{U}_\ell$
X' 0.8 $\bar{U}_\ell$
1D
−2D
−1D
1D
+1D
+3D
2D
$X'-X$ cm

FIG. 6.10

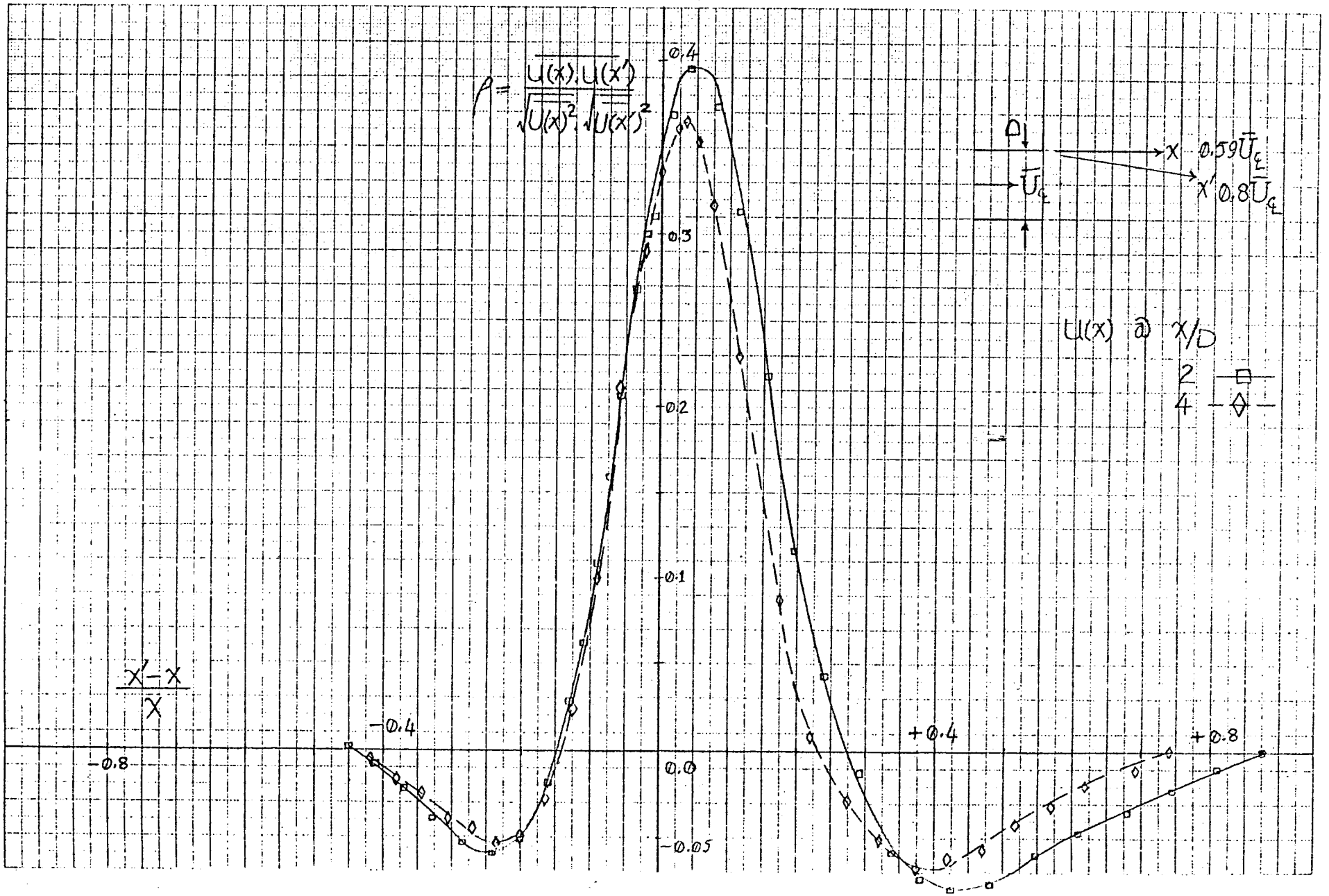
$\rho = \frac{\overline{u(x)\,u(x')}}{\sqrt{\overline{u(x)^2}}\,\sqrt{\overline{u(x')^2}}}$
0.4
0.3
0.2
0.1
0.0
-0.05
-0.4
-0.8
+0.4
+0.8
$\frac{x'-x}{x}$
D
x 0.59$\bar{U}_\ell$
x' 0.8$\bar{U}_\ell$
$\bar{U}_\ell$
u(x) @ x/D
2
4

FIG. 6.11

Figures 6.5 through 6.11. All the plotted data are for U_e = 39.5 m/s except Figure 6.6 has a superimposed plot for U_e = 16 m/s.

The maximum positive peak in the correlations drop with axial distance because when traversing in the (x, x') corrdinate system the least distance between the probes during a traverse for x/D of 2, 3 and 4 increases as the fixed probe is moved downstream. This increase minimum separation of the probes causes the small scales (order of pro separation) to become progressively uncorrelated.

The superimposed plot of Figure 6.6 shows that except for the ve large separations (2nd zero crossings) the profiles are coincident (within the range of experimental error). This indicates that the cro correlations are independent of Reynolds number in the mixing layer (that the turbulent Reynolds number should be high enough in all cases for fully developed turbulence to exist is a limiting condition that goes without saying).

The negative peaks in the cross-correlations relate to spacial scales in the range:

$$\lambda_p \simeq 25\text{-}50 \text{ cm} \qquad (6.5)$$

which is ten times as large as the range of local integral scales. Th the correlations have negative lobes of such magnitude (and at such la scales) is evidence of the amount of turbulent energy present in scale over ten times as large as the integral scales. An examination of the correlation coefficient on each plot reveals that the maximum peaks ar around ρ = 0.4. This means that close to 40% of the turbulent energy present in scales that are larger than the probe separation. The magn tude of the negative lobes indicates that the largest scales ($\lambda \geq 0.8x$ contain between 5-10% of the turbulent energy of the x-component of ve city in the mixing layer. That this observation about the large scale

is a mixing layer phenomenon and not a result of facility dependent conditions is discussed in a later section.

Figures 6.8 and 6.11 show the plots with the spacial separations normalized with x. Except for the very large scales the curves show a reasonable scaling with x, but since the scatter in the convergence is asymmetric, x does not seem to be a universal scaling parameter. The scatter and the asymmetry can be attributed to the moving probe (along x') coming too close to the jet exit and, while traversing down stream, moving into the far jet for the large separations. The two figures (6.8 and 6.11) are skewed in opposite directions. Since they are profiles measured on the opposite sides of the mixing layer this result is consistent with the mechanics of the mixing layer. A spacia autocorrelation measured along the center of the mixing layer should look symmetric about the origin. Wake effects necessitate Laser Doppl Anemometer techniques for such measurements, which are being pursued a a continuation of the present experiments.

Figures 6.12 and 6.13 are plots of various features of each cross-correlation profile. Except for the second zero crossings the other features can be closely approximated to be originating from the virtual origin based on the momentum thickness being zero (from Chapter 4). This is a very qualified statement and a significant amour of additional data are required before this speculation can be establis as a characteristic of the cross-correlation profiles.

6.3 Diagnostic Measurements on the Jet

Different diagnostic tests were conducted on the jet to verify the phenomenon evidenced in the cross-correlation and autocorrelation measurements discussed in the previous section.

Figure 6.14 is a plot of the cross-correlation function between the probes, one placed on the jet centerline at the exit plane and the second

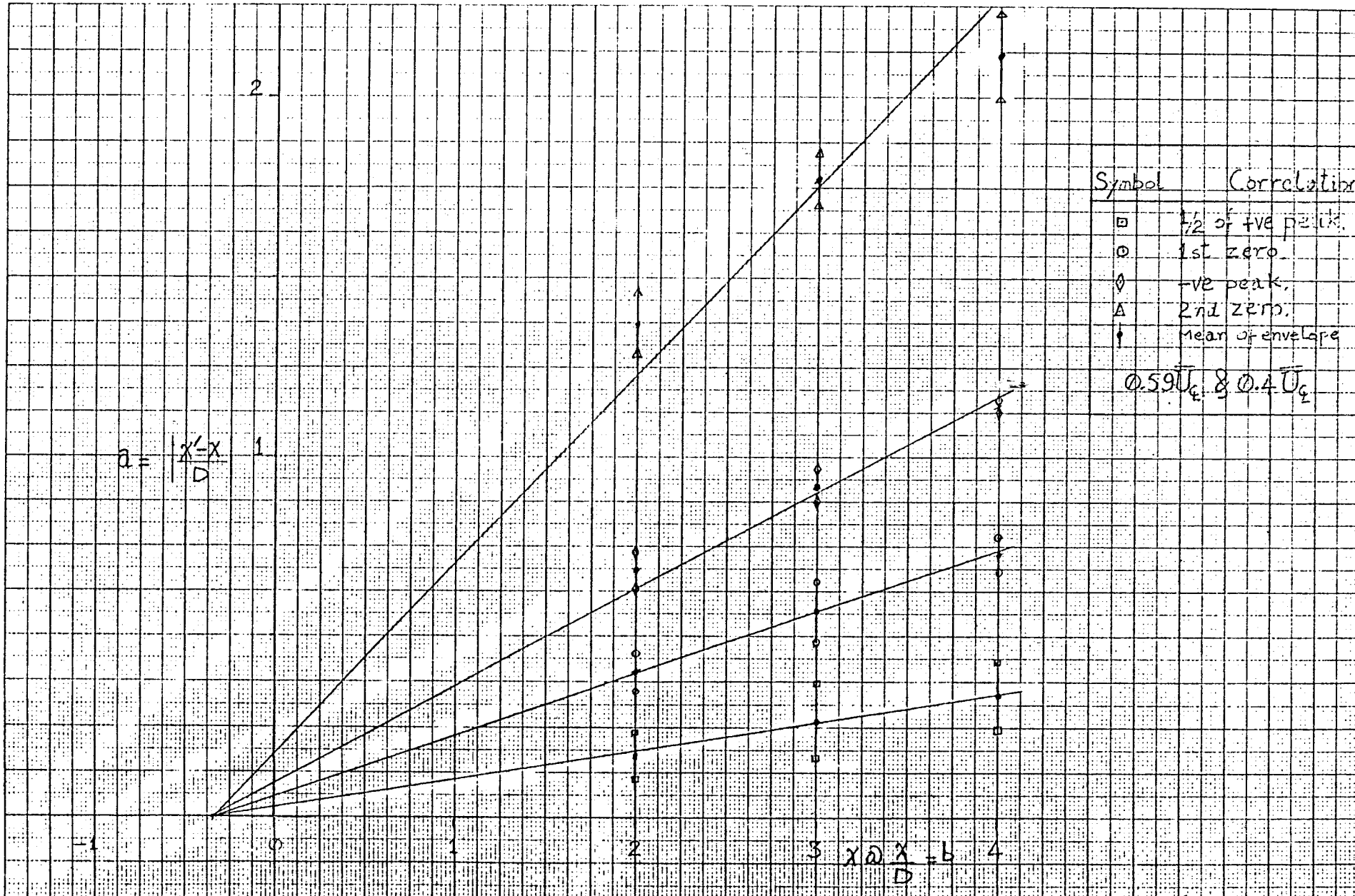
Symbol
Correlation
1/2 of +ve peak.
1st zero.
-ve peak.
2nd zero.
Mean of envelope
0.59 $\bar{U}_t$ & 0.4 $\bar{U}_t$
$a = \left|\frac{x'-x}{D}\right|$
2
1
0
-1
1
2
3
4
$x @ \frac{x}{D} = b$

$$a = \frac{x - x'}{D}$$

Symbol	Correlation
▫	1/2 of +ve peak
⊙	1st zero
◇	−ve peak
△	2nd zero
┃	Mean of envelope

$0.59\,\bar{U}_c \lesssim 0.8\,\bar{U}_c$

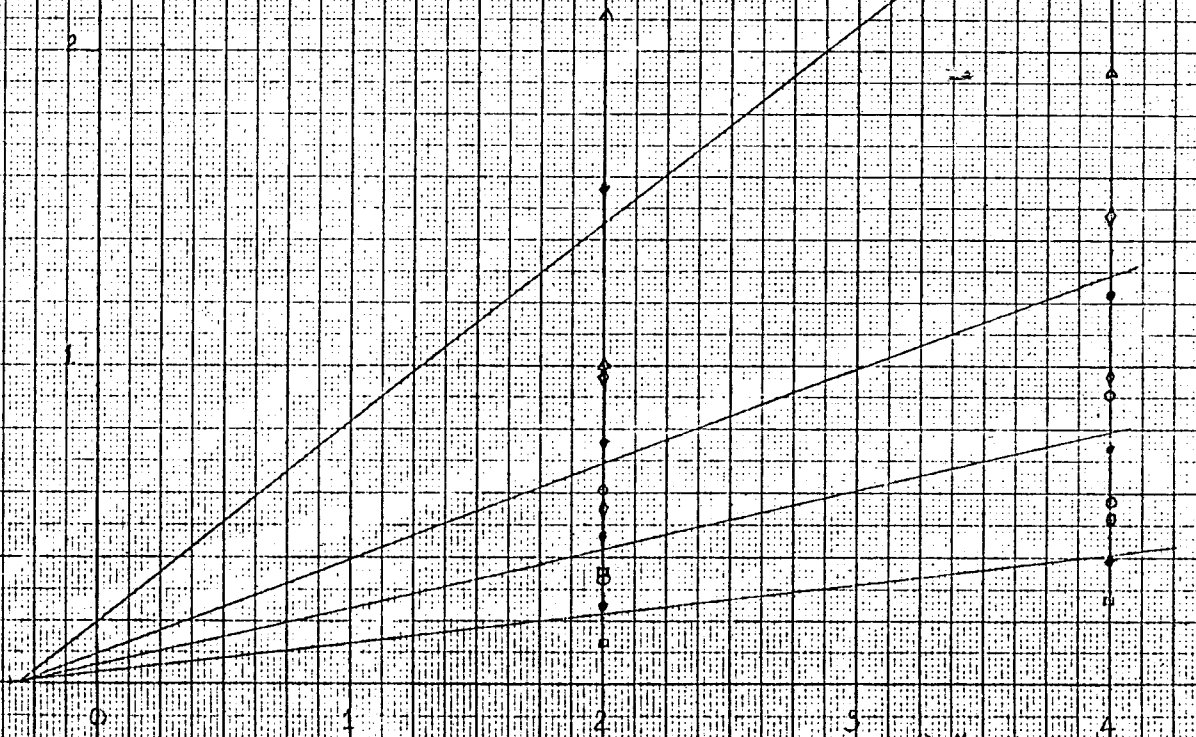

one in the center of the mixing layer at x/D of 4. Both signals were linearized and low passed at 500 Hz and AC coupled in the analyzer. Data were sampled at 1.28 KHz with a record length of 0.8 sec and processed at a bandwidth of 1.25 Hz.

$$CCF = \frac{1}{T}\int_{o}^{T} e_1(t)\ e_2(t+\tau)\ dt$$

e_1 being the signal from the upstream probe.

The highest positive peak corresponds to:

$$\frac{x_2-x_1}{\Delta t} = \overline{U}_e$$

where x_2 & x_1 are the probe positions and Δt is the time delay from zero. The large negative peak at the negative time delay seems to suggest that information goes from mixing layer towards jet exit; the scale corresponding to the peak: $\lambda = (x_2-x_1).2 = 1.6$ m. This phenomenon deserves more investigation and is beyond the scope of the present study.

Figure 6.15 is a cross correlation plot between two probes in the mixin layer, x_1 along a 0.9 $\overline{U}_e$ isocontour at x/D of 3 and x_2, separated downstrean by 10 cm, along a 0.6 $\overline{U}_e$ isocontour. Both signals were low passed at 1 KHz, AC coupled, sampled at 5.12 KHz with a record length of 0.2 sec and processe at a B.W. of 5 Hz.

The first zero crossings correspond to $x_2-x_1 = \overline{U}_c.\Delta t$. The third zero crossings are at $\pm$0.02 sec. The slightly negative time (-0.001 sec) at whic the high positive peak exists points to a similar result in section 6.2 viz. the probe at a radially outwards position sees the turbulence first. The second positive peaks on 6.14 correspond to $\overline{U}_c.\Delta t = 0.44$ m. This is the same scale size seen in spacial cross-correlation measurements of section 6. The correlation at this point is a little less than 1/3 of the correlation at zero time delay. Due to the probe separation and an average convection

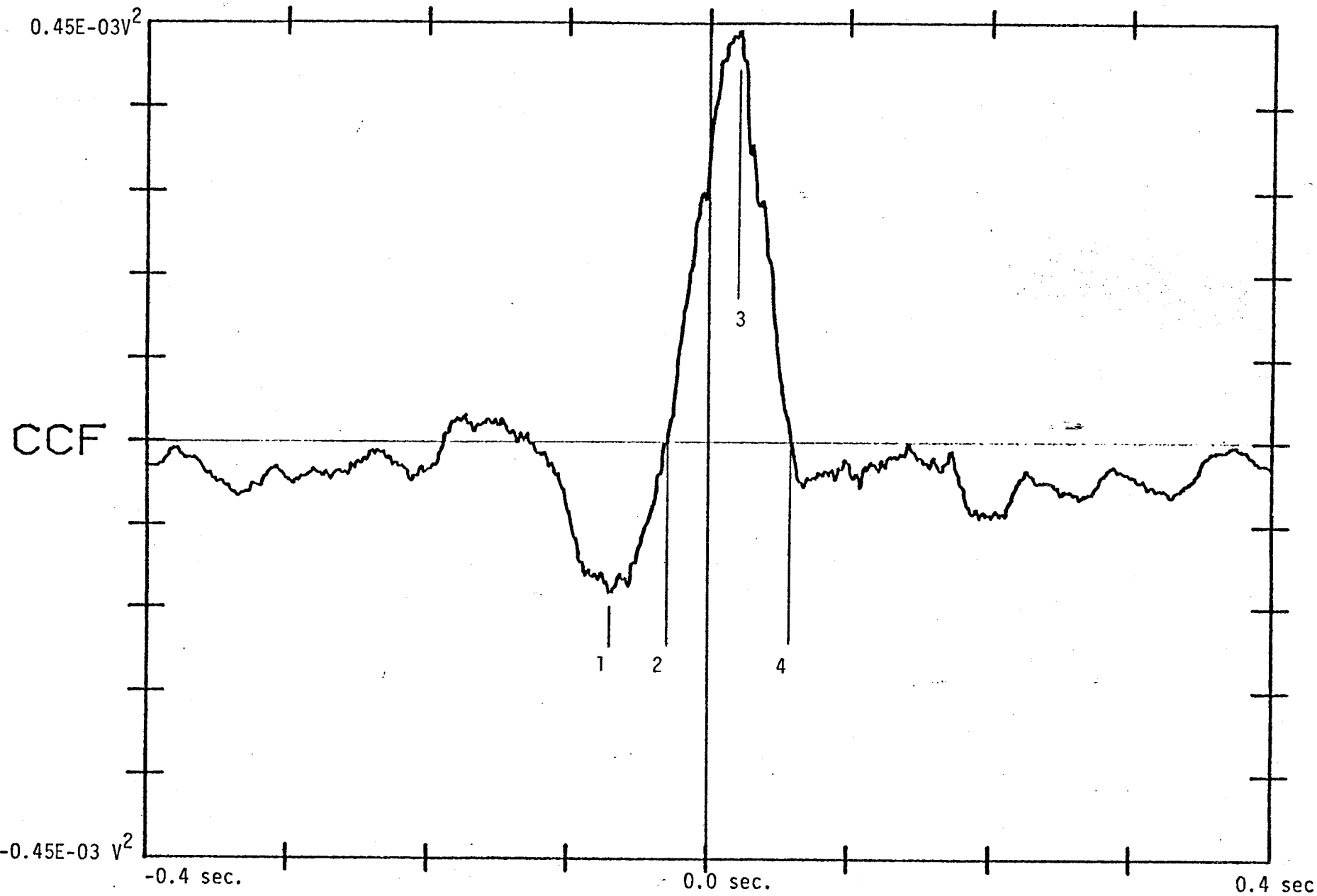

FIG 6.14 CROSS CORRELATION BETWEEN CENTER OF EXIT PLANE AND CENTER OF MIXING LAYER (X/D=4).

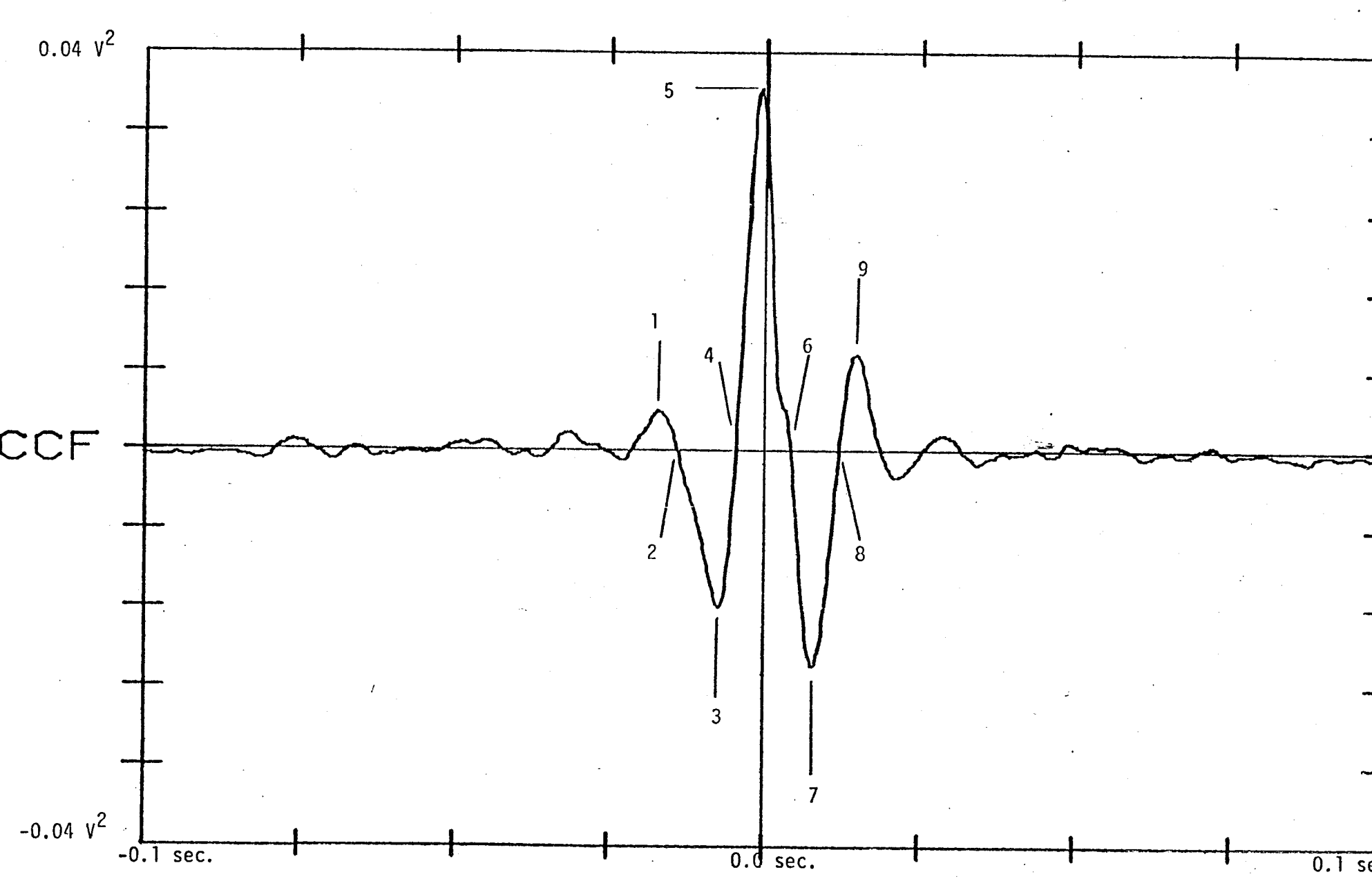

FIG 6.15.CROSS CORRELATION BETWEEN TWO POINTS IN MIXING LAYER, 0.1m APART, X/D=3, ALONG $0.6U_e$ and $0.9U_e$ STREAMLINES.
CO-ORDINATES: 1. -0.017sec.,3.9E-3 V^2., 2. -0.014sec., $0.0V^2$., 3. -0.007sec.,-17E-3V^2.

velocity of 0.75 $\bar{U}_e$ between the two probes, disturbances sweeping by at over 300 Hz would be uncorrelated between the two probes. Hence the 1 KH_z low pass filtering does not attenuate the correlation at zero time delay. This suggests that, among the scales of turbulence more than twice as large as the integral scale, about 25% of the energy is present in scales of the order of 0.4 m and larger.

Figure 6.15 was meant as a reference for 6.14. These plots were generated in an effort to investigate the possible existence of large scale oscillations and pulsing in the jet.

Comparing 6.14 and 6.15 it is evident that the magnitude of the cross-correlation between the exit plane and the mixing layer is very small. As a reference, the highest positive peak in Figure 6.14 is a decade lower than even the second negative peak of Figure 6.15. The highest positive peak is two decades lower than the corresponding peak in Figure 6.15. Looking at the time lags we see that they are many times larger than those in the mixing layer (Figure 6.15). This indicates that very large scales (order of 2 m) are being convected out from the jet but are of extremely low magnitudes.

Figure 6.16 is an autocorrelation measured at the exit plane centerline. The signal was low passed at 500 Hz, AC coupled, sampled at 1.28 KHz and data were processed at a bandwidth of 0.63 Hz. The maximum autocorrelation is 3.5 decades lower than a similar (Figure 6.1) autocorrelation in the mixing layer, the negative peak is 2.5 decades lower than a corresponding peak in the mixing layer. The second positive peak corresponds to a length scale of 6 m.

Plots 6.17 and 6.18 are cross spectra between points in the center of the jet exit and center of the mixing layer at x/D of 4. Noise dominates the spectra and the peaks are 20 dB lower than that on the exit plane power

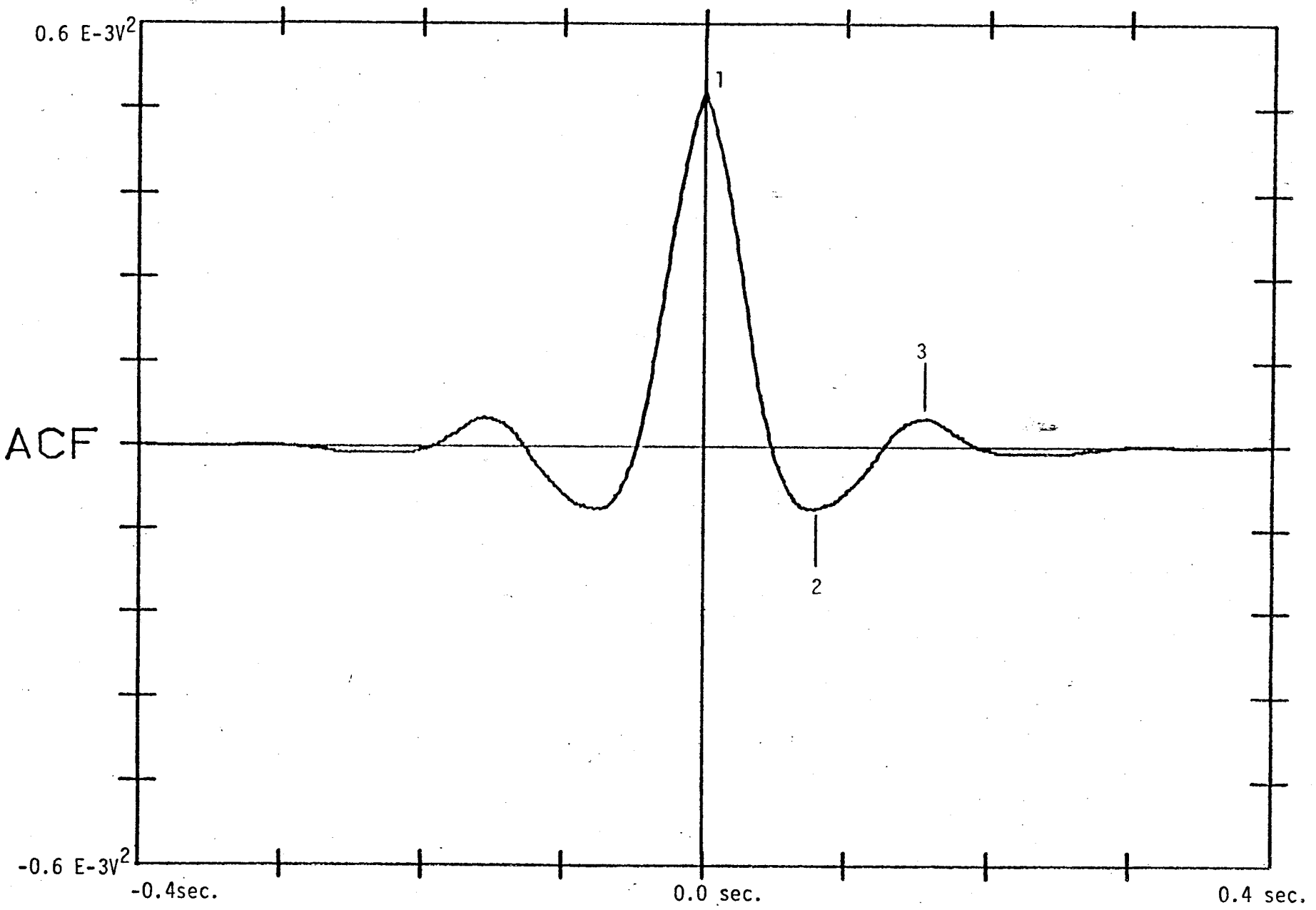

FIG.6.16 AUTO-CORRELATION AT THE CENTER OF EXIT PLANE

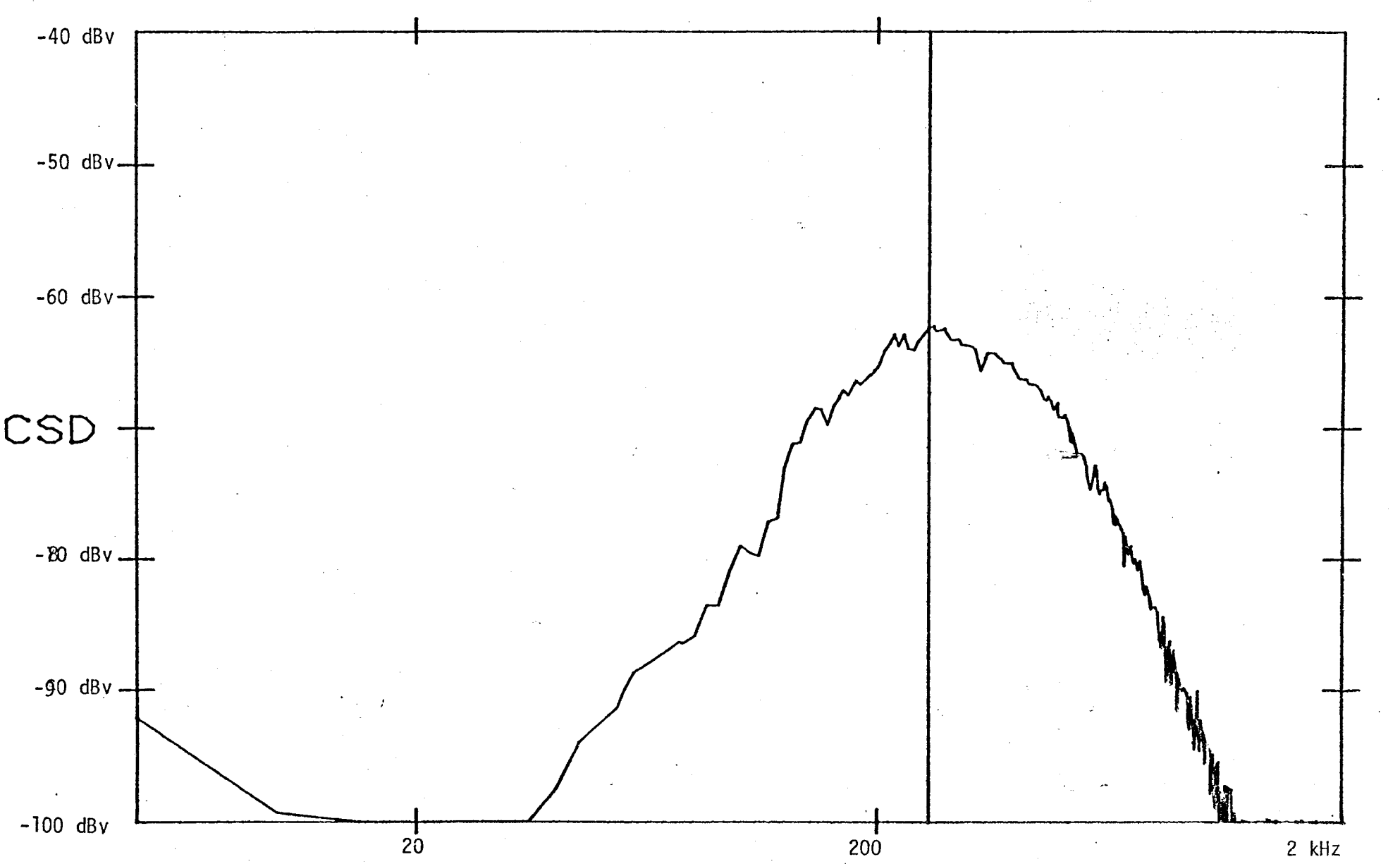

FIG 6.17 CROSS SPECTRUM BETWEEN CENTER OF EXIT PLANE AND CENTER OF MIXING LAYER (X/D=4).
PEAK : -63 dBv, 255 Hz. CSD= 10 $\text{Log}_{10}\left(\frac{V^2}{Hz}\right)$. U_e=39.5 m/s.
BOTH CHANNELS 200Hz H.P. 500Hz L.P. 0.2sec RECORD LENGTH 5 Hz B.W. 5.12 kHz SAMPLE RATE

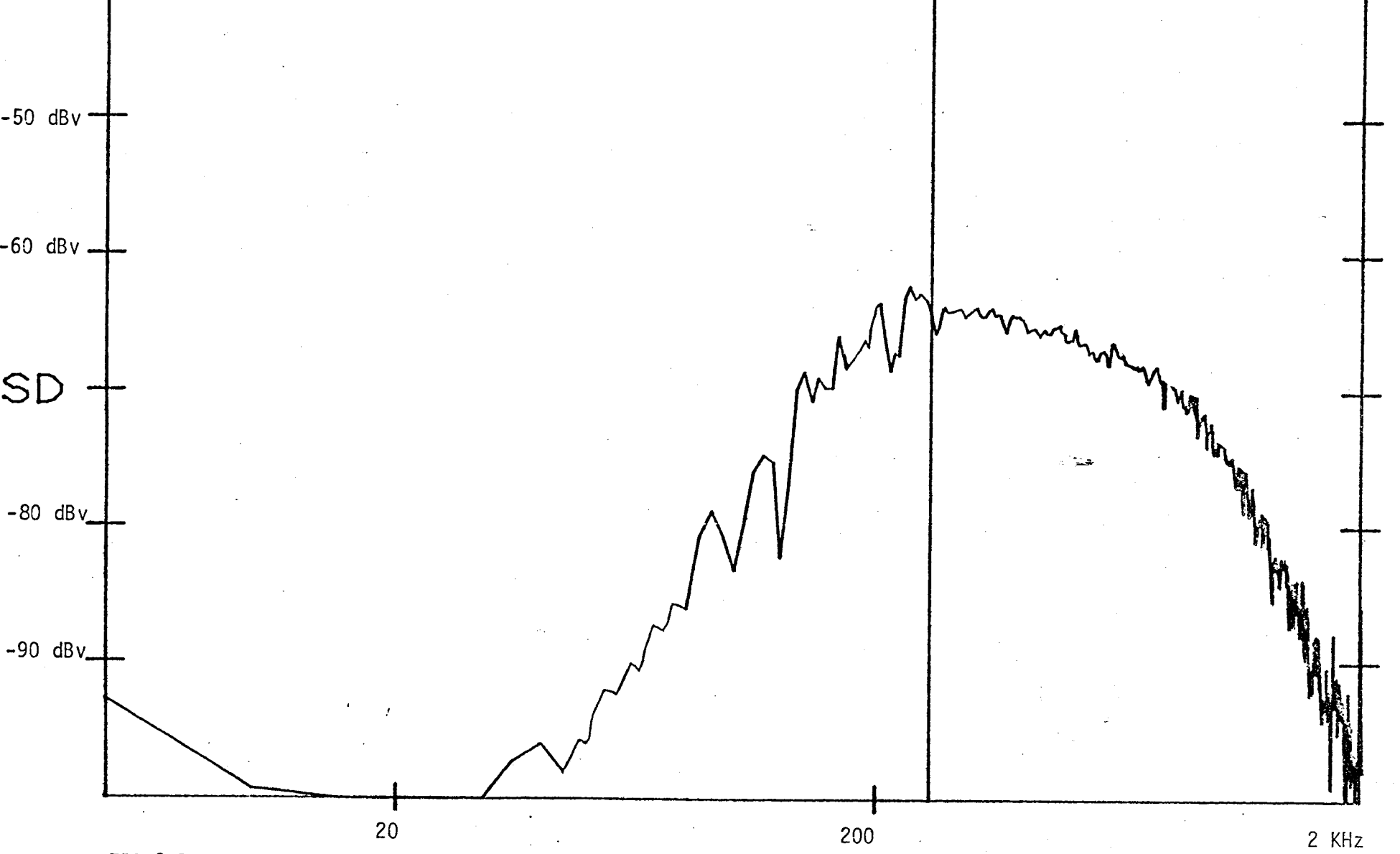

FIG 6.18 CROSS SPECTRUM BETWEEN CENTER OF EXIT PLANE AND CENTER OF MIXING LAYER (X/D=4).
PEAK : -64 dBv, 255 Hz. CONDITIONS SAME AS IN FIG. A.4 EXCEPT 1 kHz L.P.

spectrum in Figure 5.8. This indicates the extremely low level of the cross spectrum and absence of any significant cross-correlation between the two measuring locations. The plots also indicate that no significant acoustic radiation is present in the jet.

Figure 6.19 is a cross spectrum between diametrically opposite sides of the mixing layer. Probes were placed at x/D of 2 and 4. The level of the cross spectrum indicates that a significant level of coupling is preser between diametrically opposite sides of the mixing layer. Though significa the level is barely higher than background noise (about 10 dB or one decade levels. This calls for very sensitive measurements of the cross-correlatio and spectra, something that will be left to later studies.

The approximately 5 dB of scatter in the cross-spectrum of Figure 6.19 above 100 Hz may be attributed to an improper choice of the window function in the FFT analyzer and a resulting spectral leakage to higher frequencies.

Other than what is seen on the plots, cross-correlations were also mea ured between the centerline of the jet and a fixed probe in the center of the mixing layer using the instrumentation discussed in section 6.2. With a probe traversing the centerline, barely discernible peaks were observed i the cross-correlation. The correlations measured here were at least a fact of 3 lower than the corresponding correlation measured in the mixing layer in section 6.2.

Inferring from all the diagnostic measurements, the evidence suggests that there are some residual effects of jet exit fluctuations at downstream measuring points, but they do not seem to be significant. The diagnostics consistently imply that measurements in the mixing layer are unrelated to either exit conditions or noise.

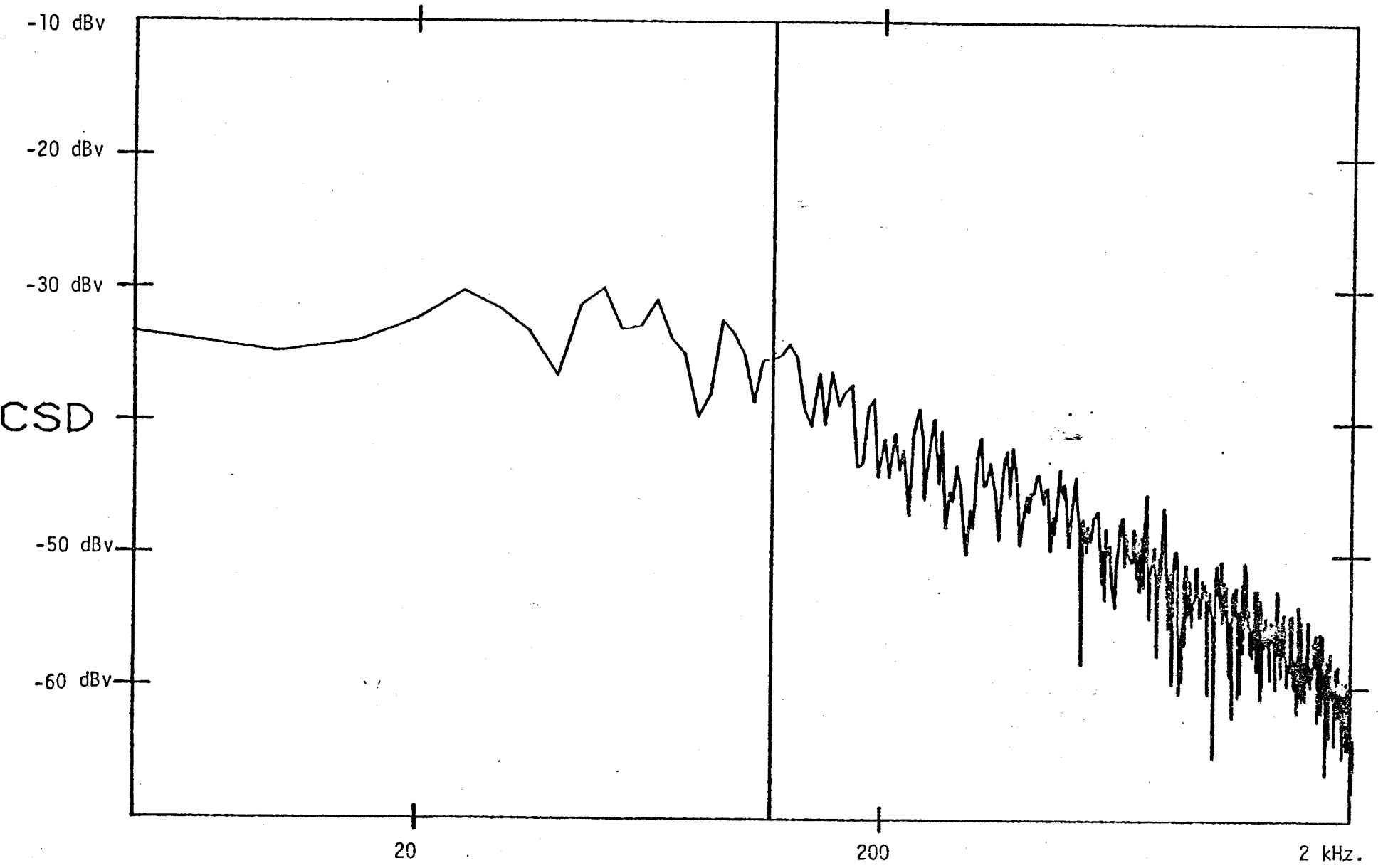

FIG 6.19 CROSS SPECTRUM BETWEEN DIAMETRICALLY OPPOSITE SIDES OF MIXING LAYER. PROBES IN CENTER OF MIXING LAYER AT X/D=2 AND X/D=4. CURSOR : 115 Hz, -35 dBv.

6.4 Discussion

The flow field in the mixing layer is highly inhomogeneous. The effect of inhomogeneity is seen in Figures 6.8 and 6.11 where the downstream ($x'>x$) and upstream ($x'<x$) correlation legs respond differently to a normalization with x. A normalization with $x'+x$ was attempted with virtually identical results. The search for scaling parameters that would make all the cross-correlation curves (from one side of the mixing layer) converge to a universal curve is continuing. It seems obvious that a constant or linear scaling is ineffective.

CHAPTER 7

7. Summary and Conclusions

During the course of this experiment work has progressed from the stage of generating an axisymmetric jet with low turbulence intensity at the exit and taking some basic measurements to developing signal processing techniques for sophisticated measurements.

The jet was thoroughly examined for axisymmetry and skewness of the mean flow. Mean and turbulent intensity profiles were measured in the free shear layer and their similarity was established with the axial coordinate as the scaling parameter.

Power spectra were measured in the mixing layer and found to scale with the axial coordinate, as well as possess a well defined $k^{-5/3}$ inertial subrange. From the one dimensional power spectra, estimates of the dissipation of turbulent energy were found to be consistent with those of other investigators. The inertial subrange was found to conform to the local isotropy hypothesis. Spanwise power spectra evidenced the concentration of energy in the mixing layer (and even to a small degree in the potential core) around the local integral scale.

Autocorrelation measurements were found to scale with the axial coordinate; the same scaling as the mean velocity and turbulence intensity profiles and the one dimensional power spectra. Both the time autocorrelation and spacial cross-correlation measurements evidenced the existence of significant energy (over 5%) in turbulence scales more thanten times as large as the integral scales. The shapes of the cross-correlation profiles indicated the inhomogeneity of the mixing layer and pointed to the need for more complex scaling parameters. In cylindrical coordinates, the ϕ dependence of the cross-correlations still needs to be investigated.

Space-time cross-spectral measurements were attempted but the results were not credible due to peculiar digital signal processing problems resulting from spectral leakage in the FFT Analyzer.

APPENDIX

Specifications, definition of functions and averaging operations of the FFT Analyzer.

A.1

NICOLET 660 A DUAL CHANNEL FFT ANALYSER. OVERALL SPECIFICATIONS

FUNCTIONS CALCULATED AND DISPLAYED	FIVE MEASUREMENT MODES (Traces x no. of data points displayed in each)			
	# 1 SIG. ENH.	# 2 CH A 2K	# 3 DUAL 1K or # 4 CORR(3)	# 5 PROB
Input Time History (IT) Averaged Time History (AT)	2x1024(1) 2x1024(1)	1x2048	2x1024(1)	2x1024(1)
Avg. Linear Spectrum (IS)	2x400			
Inst. Spec. of Input (IS) RMS Spectrum (RS) Power Spectrum (PS)		1x800 1x800 1x800	2x400 2x400 2x400	
Cross Spectrum (CS)			1x400(2)	
Transfer Function (TF) Equalized Trans. Function(ETF)			1x400(2) 1x400(2)	
Transmissibility Function (TM) Equal. Transmiss.Function(ETM)			1x400 1x400	
Coherence Function (COH) Coherent Output Power (CP)			1x400 1x400	
Impulse Response (IR) Equalized Impulse Resp.(EIR)			1x1024 1x1024	
Auto Correl. Function (ACF) Cross Correl. Function (CCF)			2x1024 1x1024	
Prob. Density Function (PDF) Cumulative Dist. Function(CDF)				2x127 2x127
NUMBER OF FUNCTIONS AVAILABLE WITHOUT CHANGING MODES OR RERUNNING DATA	6	4	20	6

FOOTNOTES:
(1) 1024 data points A vs. B in "NYQ"
(2) Complex data points; 400 real and 400 imaginary, or 400 magnitude and 400 phase, or 400 Nyquist (R vs. I)
(3) Weighting removed and pad-zeros applied in correlation

INPUT CHARACTERISTICS (Each Input Channel)

MAXIMUM AMPLITUDE - 0.1, 0.2, 0.5, 1, 2, 5, 10, 20 V (0 - peak)

COUPLING - AC (-3 dB at 0.5 Hz) or DC, normal or digitally inverted, digital ZERO is effective input ground.

IMPEDANCE - 100K ohms

TEST SIGNALS - (a) Single peak, approximately full scale amplitude, appears in each channel at 64% of analysis range (normal input is disconnected when test signal is on). (b) (Rear panel) Digitally generated random and digitally filtered random noise outputs provide standard complex functions regardless of frequency range; random sequence over 1,000,000 samples, clocked in sync with input ADC, amplitude 0-1V; trigger restarts sequence after pre-sequence of 2048 samples to create pseudo-random noise.

INPUT SAMPLING: 12-bit A/D conversion at 2.56 times maximum frequency in the range selected; 256,000 per second maximum external control.

INPUT FILTERS: Range switch automatically selects a pair of matched, low-pass anti-aliasing filters, which provide at least 70 dB attenuation of those input frequencies which can cause aliasing (10 Hz filter used on 1, 2 and 5 Hz ranges); frequency response ±0.5 dB (except ±1.0 dB on 100 kHz range).

TRANSIENT CAPTURE CONTROL: Digital data in input buffer memories held manually by placing the HOLD/REL button in HOLD (light on), or automatically by triggering on the transient waveform in either A or B input channels at a preset trigger level (±1/2, ±1/4, ±1/8, or ±1/16 FS) after ARM is pushed (light on); anticipation or delay of the trigger set using the keyboard (T →A) from -1 to 63 time windows.

INPUT AMPLITUDE MONITORS: Lights indicate peak signal levels - OVERLOAD, -6 dB (greater than 1/2 full scale), -12 dB (between 1/2 and 1/4 FS), -18 dB (between 1/4 and 1/8 FS), -24 dB (between 1/8 and 1/16 FS); electronic graticule top and bottom in time display indicates amplitude limits.

FREQUENCY RANGES: (any other coverage up to 100 kHz can be set using external sampling at 2.56 x Fmax and calibrated to read correctly using ORDERS; the anti-aliasing low-pass input filters associated with the range switch appear in the signal paths).

RANGE (Hz)	DUAL 1K MODE* NOMINAL BW (Hz)	TIME WINDOW* (SEC)
100K	250	.004
50K	125	.008
20K	50	.02
10K	25	.04
5K	12.5	.08
2K	5.0	.2
1K	2.5	.4
500	1.25	.8
200	0.5	2
100	0.25	4
50	0.125	8
20	0.05	20
10	0.025	40
5	0.0125	80
2	0.005	200
1	0.0025	400

* For CH A 2K mode, nominal BW is X 1/2, time window is X2; BW is also lowest frequency that can be read.

STORED FUNCTIONS (Internal Memory):

STORE - retains one 800-line spectrum, one 1024-time waveform, or two 400-line spectra on display cross-spectrum or TF, stores R and I regardless of

RECALL - displays stored data; reverts back to cu data display upon second actuation of pushbutton

COMPare - displays one stored trace and correspon current traces if both processed in a similar manne

EQL TF/TM - Equalizes current transfer function TF (if both processed in a similar manner) by divi tude of current by stored and subtracting phase of from current; also equalizes IR and TM.

BUILT-IN ANNOTATED DISPLAY:

VERTICAL DISPLAY - linear full scale can be set 1,5, 2, 2.5, 3, 4, 5, 6 or 8 x 10^{N}, or to cursor ampl to other number entered with keyboard; log offset + 300 dB to -300 dB in 10 dB steps, display range to 160 dB in 20 dB steps via keyboard (DSPL dB).

TIME DISPLAYS - self-aligning electronic graticul maximum amplitude written on CRT in volts 0 - p

FREQUENCY DISPLAYS - self-aligning electronic annotation includes display and scaling as well as i settings and running N of average if recalled.

DISPLAY FORMATS: Time A vs. time B; single channel where applicable; cross-spectra magnitude phase, real and/or imaginary, or real vs. imaginary for frequency, lin/log vertical and horizontal.

CALIBRATION AT CURSOR:

MARKER - single line cursor intensifies each wave intersection to indicate location of measurement; HARMONIC multiples of cursor frequency are illu with multiple dots.

AMPLITUDE - E, E^2 or dBE (engineering units) u board to establish E at cursor or sensitivity as V/E (R) set for relative measurements; V, V^2 (power) readings normalized per Hz (such as PSD) using th button.

FREQUENCY - Hz (cycles/sec), CPM (cycles/minu number, fraction of FS or orders; reads absolute o difference from reference frequency.

TIME - sec, msec, fraction of FS, cell number or (1/orders).

KEYBOARD SETTINGS: (Set and recalled)

AVG N - number of functions averaged (1 - 9999); running N can be displayed.

DLY T →A - delay (or anticipation) between trigg and start of Channel A data window set in time wi from -1.000 to +63.000.

DLY A→B - delay introduced between Channels A time windows 0 to 64.000.

PNL - stores 9 sets of complete panel settings with numbers for recall (see below).

CUR LOC - 9 cursor locations stored with ID num for recall.

RMS 1- 2 - calculates total RMS power between ar stored cursor locations; cursor alternates between locations in display.

$\int dt$, d/dt - effective time-domain integration or di tion, single or double affects all functions until cle (e.g. converts acceleration to velocity to displacem

COH BLANK - sets level of display blanking based of coherence (0 - 1.00).

PLOT RATE - five X-Y plot speeds from very slow to very fast (=5).

DSPL dB - 20 dB to 160 dB in 20 dB steps.

LIN - amplitude at cursor on CH A or CH B set to reference (recall is in V/EU).

dB - amplitude at cursor on CH A or CH B set to reference (recall is in V/EU).

V/EU - calibration sensitivity of CH A or CH B set engineering units.

to which all future cursor locations are referenced.

ORDER REF - cursor location set (in ORD), scaling future cursor locations proportionally (for example, if cursor at .1 FS is assigned "30", then FS will be "300").

DEFINE AUX - auxiliary codes used for secondary operations.

PANEL STORAGE (PNL) - stores and recalls nine sets of setup, processing and display settings.

CURSOR TYPE	COHERENCE BLANK
FREQ READ	PLOT RATE
DISPLAY GAIN (offset)	DISPLAY dB
AVERAGE MODE	INPUT AMPLITUDE
AVERAGE N	for d/dt
DELAY T→A	AUX CODE
DELAY A→B	CAL VIEU (CH A and CH B)
MODE	CAPTURE CONTROL
FUNCTION	FREQ REF
DISPLAY CH	ORDER REF
DISPLAY FORMAT	XPND WIDTH*
DISPLAY MEMORY	XPND (location)*

* with 2D Digital Expansion

NUMERIC CALCULATION: Numbers in entry field, manually entered or transferred from another field can be added, subtracted, multiplied or divided, or the square root or reciprocal taken.

AVERAGING (9 types):

SUM adds N power spectra (N = 1 - 9999 set with keyboard); redundancy selectable 0% or 50%.

DIFF subtracts N power spectra from previous average.

EX follows the changing statistics of a signal exponentially with a time constant of (N) x (time window).

PEAK produces the profile of the maximum amplitudes at each frequency element during N spectra.

SWEEP averages with maximum redundancy.

TRANS averages power spectra of N transients automatically in SUM, DIFF, EX or PK modes, except *those which overload input*; after each capture, the transient trigger is automatically re-armed; used for time averaging.

AVERAGING CONTROL:

START erases memory and starts averaging.

STOP halts averaging.

CONT resumes averaging until N is reached; if averaging completed, restarts averaging without erasing memory.

ANALOG OUTPUTS: X, Y and Z outputs for s
display; X, Y and pen lift for X-Y plotters; timin
for 3-D display (see Model 66-2A); PLOT CAL p
lower-left and upper-right of grid for setup; outp
tude at cursor

DIGITAL INTERFACES (Standard Built-In):

a. Full duplex RS232 serial interface with select
baud rates of 110, 150, 300, 600, 1200, 2400
9600; internal programming communicates w
digital plotters through the RS232 interface,
to communicate with external devices, the ou
the RS232 interface are printable in ASCII ch

b. IEEE488-1975 interface (full listener/talker).

c. High-speed 12-bit A/D converter output inter
16-bit parallel words (two channels simultane
16-bit digital input to time buffer.

POWER: 425 watts, 600 VA

WEIGHT: 36.4 kgm (80 pounds) nominal

SIZE: 35.56 cm (14 in.) high, 43.18 cm (17 in.)
52.79 cm (20-7/8 in.) deep.

A.1 (continued)

DISPLAY SELECT	FUNCTION COMPUTED	DESCRIPTION
Time (Δ) (Inpt. Time - IT)	$A(t)$	Digital time history of input signal. (Display shows actual data processed)
Instant FFT (Δ) (Inst. Spec. - IS)	$S_A = \mathcal{F}\{A(t)\}$ $= \lvert S_A\rvert\cos(\phi_A) + j\lvert S_A\rvert\sin(\phi_A)$	Complex spectrum of time history, A(t). Magnitude $\lvert S_A\rvert$ defines instantaneous spectral content. Phase angle, ϕ_A, describes *relative phasing* of periodic harmonic components. Absolute angles are only meaningful if analysis window is synchronized to periodic data.
LIN	$\lvert S_A\rvert$	
LOG	$20\ LOG_{10}\ \lvert S_A\rvert$	
PHASE	ϕ_A	
REAL	$\lvert S_A\rvert\cos\phi_A$	
IMAG	$\lvert S_A\rvert\sin\phi_A$	
Aver. Spec. (Δ) (Pwr. Spec. - PS)	$G_{AA} = \overline{S_A \cdot S_A^*}$ $= \overline{S_A^2}$	Ensemble average of squared spectrum magnitude (formed by multiplying complex spectrum by its conjugate). A real (rather than complex) spectrum defining *average power* at each frequency.
LIN	G_{AA}	
LOG	$10\ LOG_{10}\ G_{AA}$	
(RMS Spec. - RS)	$\sqrt{G_{AA}}$	
Aver Cross Spec (X Spec. - CS)	$G_{AB} = \overline{S_B \cdot S_A^*}$ $= \overline{\lvert S_A\rvert\lvert S_B\rvert\cos(\phi_B - \phi_A)} + j\overline{\lvert S_A\rvert\lvert S_B\rvert\sin(\phi_B - \phi_A)}$	Ensemble averaged complex product of spectrum with conjugated spectrum, S_A^*. Indicates those frequencies where *both* A(t) and B(t) have content. Phase angles indicate average phase *difference* between signals at each frequency.
LIN MAG	$\lvert G_{AB}\rvert$	
LOG MAG	$10\ LOG_{10}\ \lvert G_{AB}\rvert$	
PHASE	$\overline{\phi_B - \phi_A}$	
REAL	$\overline{\lvert G_{AB}\rvert\cos(\phi_B - \phi_A)}$	
IMAG	$\overline{\lvert G_{AB}\rvert\sin(\phi_B - \phi_A)}$	
Auto-Correlation Function (Δ) (Auto Corr. - ACF)	$R_{AA}(\tau) = \mathcal{F}^{-1}\{G_{AA}\}$ $= \frac{1}{P}\int_0^P A(t)\cdot A(t+\tau)dt$	Time domain statistic comparing *similarity* of A(t) to replicates of *itself*, delayed by time, τ. At $\tau = 0$, R_{AA} = mean square of A(t). As $\tau \to \infty$, R_{AA} approaches square of mean value. Oscillations in R_{AA} indicate *bandwidth* and *periodicity* of A
Cross-Correlation Function (X Corr. - CCF)	$R_{AB}(\tau) = \mathcal{F}^{-1}\{G_{AB}\}$ $= \frac{1}{P}\int_0^P A(t)B(t+\tau)dt$	Time statistic comparing *similarity* of A(t) a Value of τ that maximizes R_{AB} indicates *tim* between signals. Maximum value of R_{AB} di square root of $[R_{AA}(0)][R_{BB}(0)]$ yields co coefficient (equal to 1 for identical signals, 0 unrelated signals).

Definition of Symbols

- $A(t)$ = Input time function on Channel A
- $B(t)$ = Input time function on Channel B
- $\lvert S\rvert$ = Magnitude of instant FFT = $\sqrt{S_{REAL}^2 + S_{IMAG}^2}$
- ϕ = Phase angle of instant FFT = $\tan^{-1}\frac{S_{IMAG}}{S_{REAL}}$
- j = $\sqrt{-1}$
- S^* = Complex conjugate of $S = S_{REAL} - j\,S_{IMAG}$
- (overbar) = Ensemble average
- t = Time
- τ = Artificially introduced time delay
- $\mathcal{F}\{\ \}$ Direct Fourier Transformation
- $\mathcal{F}^{-1}\{\ \}$ Inverse Fourier Transform

(Δ) Similar for Channel B

A.3 AVERAGING OPERATIONS

Type of Averaging	Operation Performed
Summation (SU, TSU, SWEEP)	$G_{k+1} = G_k + S_{k+1} \quad 0 \le k \le N$ $0 \le k \le \infty$ for swee $P_{i(k+1)} = P_{i(k)}$ for $A_{i(k+1)}(t) \neq v_i$ $= P_{i(k)+1}$ for $A_{i(k+1)}(t) = v_i$
Difference (DF, TDF)	$G_{k+1} = G_k - S_{k+1} \quad 0 \le k \le N$
Exponential (EX, TEX)	$G_{k+1} = \frac{S_{k+1} - G_k}{2\exp(N^*)} + G_k \quad 0 \le k$ $N^* =$ Integer $(\log_2 N)$
Peak (PK, TPK)	$G_{k+1} = \max \left(S_{i(k+1)}, G_{ik} \right)$ for all i $0 \le k \le N$

Notation:

P	=	Probability value
A(t)	=	Input time waveform
G	=	Current averaged spectrum or spectra
S	=	Instanteous spectrum
k	=	Number of averages completed
N	=	Number of averages set via Calculatic Control Keyboard. Wake up value = 1
i	=	Particular cell in spectrum mode or bin in probability mode
v_i	=	Voltage range associated with bin i

REFERENCES

1. Abramovich, G.N. (1963) *The Theory of Turbulent Jets*, (M.I.T. press).

2. Arndt, R.E.A., Tran, N.C., Barefoot, G.L. (1974) *Turbulence and acoustic characteristics of screen perturbed jets*, AIAA Journal, 12, 3, 261-262.

3. Batchelor, G.K. (1953) *Theory of Homogeneous Turbulence*, Cambridge University Press, Cambridge, England.

4. Bradshaw, P., Ferriss, D.H. and Johnson, R.F. (1964) *Turbulence in the noise producing region of a circular jet*, JFM, 19, 591-624.

5. Browand, F.K. and Weidman, P.O. (1975) *Large scales in the developing mixing region*, JFM, 76, 1, 127-144.

6. Champagne, F.H., Pao, Y.H. and Wygnanski, I.J. (1975) *On the two-dimensional mixing region*, JFM, 74, 2, 209-250.

7. Crow, S.C. and Champagne, F.H. (1970) *Orderly Structure in Turbulence*, JFM, 48, 3, 547-591.

8. Davies, P.O.A.L., Fisher, M.J. and Barrat, M.J., *The characteristics of the turbulence in the mixing region of a round jet*, JFM, Vol.15, 1971, pp. 337-367.

9. Davies, P.O.A.L. and Yule, A.J. (1974) *Coherent Structures in Turbulenc* JFM, 69, 3, 573-537.

10. George, W.K., Jr. (1979) *Processing of Random Signals*, Proc. of the Dynamic Flow Conf. 1978, P.O. Box 121, DK-2740, Skovlunde, Denmark, 757-800.

REFERENCES (cont.)

11. George, W.K., Jr., (1980) Presentation at meeting of principals of the cooperative investigation of jet noise (1979), IIT, Chicago, Ill.

12. George, W.K., Jr., Beuther, P.D. and Arndt, R.E.A. *Pressure Spectra in Turbulent Free Shear Flows*, (To be published) AIAA Journal.

13. Hinze, J.O. (1975) Turbulence, McGraw-Hill, Inc.

14. Husain, Z.D. and Hussain, A.K.M.F. (1979) AIAA J. 17, 48.

15. Hussain, A.K.M.F. and Zedan, M.F. (1978) *Effects of the initial condition on the axisymmetric free shear layer*, Phys. Fluids, Vol. 21, Nos. 7 & 9.

16. Jenkins, G.M., Watts, D.G. (1968) *Spectral analysis and its applications*, Holden-Day, San Francisco.

17. Jones, B.G., Planchon, H.P. and Hammersley, R.J. *Turbulent Correlation measurements in a two stream mixing layer*, AIAA Journal, 1973, Vol. 11, pp. 1146-1150.

18. Lau, J.C., Fisher, M.J. and Fuchs, H.V. (1972) *The intrinsic structure of turbulent jets*, Journal Sound & Vibration, 22, 4, 379-406.

19. Monin, A.S. and Yaglom, A.M. (1965) *Statistical Fluid Mechanics; Mechanics of Turbulence*, Vol. 1, MIT Press.

20. Nagib, H.M. (1980) Presentation at the meeting of principals of the cooperative investigation of jet noise,(April, 1979), IIT, Chicago.

21. Nee, N. (1980) *Investigation of an axisymmetric jet using Laser Doppler Anemometer techniques*". M.S. Thesis, State University of New York at Buffalo.

REFERENCES (cont.)

22. Popiel, Cz.O. and Boguslawski, L. (1978) *Flow Structure of the Free Round Turbulent Jet in the Initial Region*, JFM, 90, 3, 531-539.

23. Sasidhar, E. (1980) *Four Axis Microcomputer Control Probe Positioning System for Flow Measurement*, M.S. Thesis, State University of New York at Buffalo.

24. Sokolov, M., Hussain, A.K.M.F. and Kleis, S.J. (1979), JFM, 98, 1, 65-95.

25. Tennekes, H. and Lumley, J.L. (1972) *A First Course in Turbulence*, The MIT Press.

26. Tran, N.C., *Turbulence and Acoustic Characteristics of a Screen Perturbed Jet*, M.S. Thesis, 1973, The Pennsylvania State Univ.

27. Wills, J.A.B. (1964) *On convection velocities in turbulent shear flows*, JFM, 20, 3, 417-432.

28. Wygnanski, I., Fiedler, H. (1969) *Some measurements in the self-preserving jet*, JFM, 38, 3, 577-612.

29. Yule, A.J. (1978) *Large-scale structure in the mixing layer of a round jet*, JFM, 89, 3, 413=432.